NUMERICAL AND EXPERIMENTAL INVESTIGATION OF INORGANIC NANOMATERIALS FOR THERMAL ENERGY STORAGE (TES) AND CONCENTRATED SOLAR POWER (CSP) APPLICATIONS

A Dissertation

by

SEUNGHWAN JUNG

Submitted to the Office of Graduate Studies of
Texas A&M University
in partial fulfillment of the requirements for the degree of

DOCTOR OF PHILOSOPHY

May 2012

Major Subject: Mechanical Engineering

Numerical and Experimental Investigation of Inorganic Nanomaterials for Thermal Energy Storage (TES) and Concentrated Solar Power (CSP) Applications

NUMERICAL AND EXPERIMENTAL INVESTIGATION OF INORGANIC NANOMATERIALS FOR THERMAL ENERGY STORAGE (TES) AND CONCENTRATED SOLAR POWER (CSP) APPLICATIONS

A Dissertation

by

SEUNGHWAN JUNG

Submitted to the Office of Graduate Studies of
Texas A&M University
in partial fulfillment of the requirements for the degree of

DOCTOR OF PHILOSOPHY

Approved by:

Chair of Committee,	Debjyoti Banerjee
Committee Members,	Timothy J. Jacobs
	Devesh Ranjan
	Kamran Entesari
Head of Department,	Jerald A. Caton

May 2012

Major Subject: Mechanical Engineering

ABSTRACT

Numerical and Experimental Investigation of Inorganic Nanomaterials for Thermal Energy Storage (TES) and Concentrated Solar Power (CSP) Applications.
(May 2012)
Seunghwan Jung, B.S., Sungkyunkwan University;
M.S., University of Southern California
Chair of Advisory Committee: Dr. Debjyoti Banerjee

The objective of this study is to synthesize nanomaterials by mixing molten salt with inorganic nanoparticles. The thermo-physical properties of the synthesized nanomaterials were characterized experimentally.

Experimental results allude to the existence of a distinct compressed phase even for the solid phase. The specific heat capacity of the nanocomposites was observed to be enhanced after melting and re-solidification more than those of the nanocomposites that were not subjected to melting and re-solidification. This showed that melting and re-solidification induced molecular reordering even in the solid phase - leading to enhancement in the specific heat capacity.

Numerical models were developed to simulate the fundamental transport mechanisms and the energy storage mechanisms responsible for the observed enhancements in the thermo-physical properties. In this study, a simple analytical model was proposed for predicting the specific heat capacity of nanoparticle suspensions. The model explored the effect of the compressed phase at the interface with individual nanoparticles in the mixture. The results from the numerical simulations indicated that, depending on the properties and morphology of the compressed phase, – it can cause significant enhancement in the specific heat capacity of nanofluids and nanocomposites.

The interfacial thermal resistance between a nanoparticle and the surrounding solvent molecules was estimated using Molecular Dynamics simulations. This exercise is relevant for the design optimization of nanomaterials. The design trade-off is between maximizing the thermal conductivity of the nanomaterial (typically occurs for nanoparticle size between 20-30nm) and maximizing the specific heat capacity (typically occurs for nanoparticle size less than 5nm), while simultaneously minimizing the viscosity of the nanofluid.

The rheological behavior of nanofluids can be non-Newtonian even at very low mass concentrations of nanoparticles, while the pure molten salt may be a Newtonian fluid. Such viscosity enhancements and change in rheological properties of nanofluids can be detrimental to the operational efficiencies for thermal management as well as energy storage applications. Hence, the rheological behavior of the nanofluid samples was measured experimentally and compared to that of the neat solvent.

The results from the analytical and computational investigations, as well as the experimental measurements performed in this proposed study, – were used to formulate the design rules for maximizing the enhancement in the thermo-physical properties of molten salt based inorganic nanomaterials. The results from these studies are summarized and the future directions are identified as a conclusion from this study.

DEDICATION

To my wife, Hyemin, my son, Minjae (Ryan), and my beloved parents

for their endless support

ACKNOWLEDGEMENTS

I would like to thank my committee chair, Dr. Debjyoti Banerjee, and my committee members, Dr. Timothy J. Jacobs, Dr. Devesh Ranjan, and Dr. Kamran Entesari, for their guidance and support throughout the course of this research.

I would like to thank Dr. Frederic Best and Dr. Michael Schuller for their contributions to the collaborative project sponsored by the Department of Energy (DOE) Solar Energy Technology Program (SETP) for Concentrated Solar Power (CSP) that made this work possible.

I also acknowledge the Material Characterization Facility (MCF) and the Microscopy and Image Center (MIC) at Texas A&M University for access to their facilities. The FE-SEM acquisition was supported by the NSF grant DBI-0016835, the VP for Research Office, and the TX Eng. Exp. Station.

Thanks also go to my friends and colleagues and the department faculty and staff for making my time at Texas A&M University a great experience.

Finally, thanks to my mother and father for their encouragement and to my wife for her patience and love.

NOMENCLATURE

A_s	total surface area of the nanoparticle [m^2]
a	radius of primary nanoparticle
a_a	radius of nanoparticle aggregation
C	specific heat capacity [J/g-K]
c_p	specific heat capacity [J/g-K]
D	diameter [m]
d_c	optimum diameter [nm]
E	energy [joule]
G	interfacial conductance [W/m^2-K]
h	heat transfer coefficient [W/m^2-K]
k	thermal conductivity [W/m-K]
k_{eff}	effective thermal conductivity of the nanofluid [W/m-K]
k_b	thermal conductivity of the neat solvent [W/m-K]
k_p	thermal conductivity of the nanoparticle [W/m-K]
L	characteristic length scale of the flow system [m]
m	mass [g]
N_1	first normal stress difference [Pa]
Q	heat [joule]
q_i, q_j	charge [C]
Δq	differential heat flow [mW]

R_b	interfacial thermal resistance [m^2K/W]
r_{ij}	distance between the atoms [Å]
r_0	equilibrium bond distance [Å]
T	temperature [K]
U	characteristic velocity [m/sec]
V	volume [m^3]
V_{np}	volume concentration of the carbon nanotube
W	work [joule]
x	mass concentration
$\dot{\gamma}_{yx}$	shear rate [1/sec]
ε	dissociation energy [kcal/mole]
η	viscosity [Pa-S]
$[\eta]$	intrinsic viscosity [1/volume fraction]
φ	volume concentration of nanoparticle
φ_m	maximum concentration
φ_a	effective volume fraction of aggregations
$\eta_{th,rev}$	thermal efficiency
λ_f	fluid relaxation time [sec]
μ	viscosity [Pa-S]
θ_0	equilibrium value of the angle [radian]
ρ	density [g/cm^3]
σ	collision diameter [Å]

τ	time constant [psec]
τ_{yx}	shear stress [Pa]
ψ_0	equilibrium value of the improper angle [radian]

subscripts

n, np	nanoparticle
s	compressed phase, sample
st	standard material
b	baseline (empty pan)
l	solvent

TABLE OF CONTENTS

CHAPTER Page

LIST OF FIGURES

Page

Page

Page

Page

Page

Page

Page

LIST OF TABLES

Page

Page

Page

CHAPTER I

INTRODUCTION

Molten salt and their eutectics are typically used as materials for Thermal Energy Storage (TES) and as heat transfer fluid (HTF) in various energy conversion processes, such as in Concentrating Solar Power (CSP) stations and nuclear power stations. However, the molten salt has poor thermo-physical properties compared to conventional HTF (such as water and oils). The operational efficiencies for energy conversion can be improved and the operating costs can be reduced - if the thermo-physical properties of HTF and TES materials are enhanced. Typically thermo-physical properties of solvents can be enhanced by mixing with nanoparticles, usually at low mass concentrations (e.g., less than 1%). Solvents mixed with uniformly dispersed nanoparticles to form a stable suspension are called “nanofluids” [1-5]. The solid phase of the solvent mixed with nanoparticles (i.e., the solid phase of the resulting nanomaterial) is termed as “nanocomposite” [6].

The melting points of the molten salt are typically tuned by mixing two or more types of salt – with the cation typically being alkali metals (e.g., Ca, K, Li, Mg, Na, etc.) and a variety of anions (e.g., carbonate, nitrate, chlorides, fluorides, etc.). Molten phase of these salt are termed as “ionic liquids” (i.e., they dissociate into cations and anions). The eutectic compositions of these salt mixtures are typically utilized in TES – in order to minimize the melting point and to obtain homogeneous formulations [7].

This dissertation follows the style of Journal of Heat Transfer.

In CSP systems insolation is collected from a large area and focused onto a receiver (also called “solar power tower”) - using an array of lenses or mirrors (also called “heliostats”). Depending on the operating temperature of the CSP station and the TES, the typical materials used as HTF in the receiver tube to capture the incident thermal energy (i.e., thermal radiation) can be water (or steam), synthetic oils, fatty acids, or molten salt. Typically the HTF transfers the concentrated thermal energy harvested by the receiver to TES. The energy from TES is then utilized to run a heat engine to produce work (i.e., electrical power). The heat engine can typically use Rankine cycle (i.e., use a separate heat exchanging loop to produce steam and drive a turbine). Alternatively, the heat engine can be operated in a Stirling cycle to produce electricity. Several configurations and architectures are used in contemporary CSP stations, which are categorized as “solar power tower”, “parabolic trough” and “dish-Sterling unit” [8].

TES provides several advantages for the economical operation of CSP stations [9]. It provides a cheap and economical way to store the harvested solar thermal energy (as opposed to electrical energy storage using batteries – which can be quite expensive in comparison). In addition, TES enables the CSP plants to be operational even during disruptions in the energy supply from the Sun (e.g., during cloud cover and at night time). TES enables the operation of the CSP stations to be extended to several hours into the night time (i.e., after sunset).

TES also enables bridging of demand and supply for utilities. By matching the peak in energy supply (that typically occurs between 1-3 p.m. on an average day) to the peak in energy demand usually encountered by the utilities (that typically occurs between 4-7 p.m. on an average week-day) - TES enables economically competitive operation of CSP stations. Hence, even by providing energy storage capability for just 4-6 hours the TES enables competitive and attractive pricing options for solar thermal power, considering the levelized cost of electricity (LCOE) for the utilities in the contemporary energy trading markets. This shows that huge volume (or size) of TES that may be assumed to be needed (e.g., TES capability for supporting 12 hours of operation during night-time) - is not really required for delivering power at competitive prices from CSP stations. Hence, a CSP station operating for just 6-8 hours with a TES system capable of supporting 4-6 hours of operation can be an economically competitive option in the contemporary energy trading market. Hybrid systems that utilize coal-based or gas-based thermal power generation units during night-time (in combinations with CSP stations for operation during day-time) are expected to provide even better competitive pricing options for the cost of electricity generated by these hybrid power generation stations [9].

The contemporary commercial CSP stations typically utilize alkali-nitrate molten salt and their eutectics as materials for Thermal Energy Storage (TES) [9]. Alkali-nitrate eutectic materials are also under exploration as heat transfer fluid (HTF) [10].

A solar power tower that utilizes TES devices can sometimes utilize molten salt as HTF. In such system, the HTF is used to transfer the harvested concentrated solar energy to a “hot” storage tank containing a molten salt mixture. The thermal energy from the hot storage tank is used to generate steam (using a separate heat exchanger flow loop) and in the process the molten salt is cooled down. Due to systemic issues associated with the start-up process for a CSP station, care is taken in the design/ operation procedures to prevent the solidification of the molten salt when the thermal energy stored in the hot storage tank is tapped for generating steam. The generated steam is used for driving a turbine for obtaining electric power (i.e., using Rankine cycle). The liquid molten salt that is cooled down in the process is pumped to a “cold” storage tank during the heat-exchanging process that occurs during the operation of the CSP station. The molten salt from the cold storage tank is then pumped to the solar power tower during the day time for heating and then pumped into the hot storage tank.

As mentioned before, if the thermo-physical properties of the materials used for HTF and TES are enhanced, the resulting improvements in the operational efficiencies can enable the reduction in the cost of power generated from CSP stations. One strategy for improvement of the thermo-physical properties is to mix the salt with nanoparticles for synthesizing various nanomaterials. The CSP stations are considered to undergo catastrophic failure in the event the TES materials freeze that can occur during periods of low insolation or excessive energy loss from TES (i.e., complications arising from efforts needed to thaw the frozen materials during periods of low insolation, e.g., during system start-up in the morning). The specific heat capacity is therefore more dominant material property than fusion enthalpy that determines the efficacy of the TES material. Hence materials characterization of the liquid phase of the molten salt nanomaterials (i.e., nanofluids) is important for determining the efficacy for their applications in CSP stations. However, the solid phase properties of these alkali salt nanomaterials (i.e., the nanocomposites) is also important for designing the operational aspects related to system start-up for these CSP stations.

As mentioned before, nanofluids are colloidal suspensions of dispersed nanoparticles in liquids (solvents), and are typically synthesized by mixing nanoparticles with the solvents at very low mass concentrations [1-5, 11-13]. Compared to conventional solvents doped with micron-sized particles, nanoparticles (at minute concentrations) can enable more stable fluid emulsions or suspensions. Hence, the flow components that utilize nanofluids are less susceptible to clogging (such as valves, pumps, seals, etc.). Several literature reports have shown the enhancement of thermo-physical properties of nanofluids compared to those of the neat solvent. Hence nanofluids were traditionally envisioned for applications in various heat transfer applications – such as for enhanced cooling in compact systems [14]. Nanofluids obtained from carbonate eutectics are also being explored for thermal energy storage (TES) – in CSP stations [15-18]. The effects of nanoparticle doped in nitrate thermal storage material were investigated by Betts (2011) [10].

The cost-benefit analyses for mixing Hitec-Solar Salt with nanoparticles was performed by Malik (2010) [19] using the “Excelergy Model” developed at National Renewable Energy laboratory (NREL). The analyses show that if the cost adding nanoparticles into Hitec-Solar Salt increases the materials cost by ~10%, and if this causes specific heat capacity enhancement of 20% the cost of power generated by a CSP plant can be reduced by ~10%. On the other hand, if the cost adding nanoparticles into Hitec-Solar Salt increases the materials cost by ~10%, and if this results in specific heat capacity enhancement of ~50% - 100% - the cost of power generated by a CSP plant can be reduced by ~30%-50%. Hence, significant enhancement of specific heat capacity has a direct cost-benefit even if the incorporation of nanomaterials results in marginal increase in material cost.

The efficacy of thermal transport for convection processes (natural convection as well as forced convection) is determined by the magnitude of the heat transfer coefficient (h). For example, the forced convective heat transfer coefficient (h) for laminar and turbulent flows can be expressed by correlations [20]:

$$Nu = f\,(Re, Pr) \tag{I-1}$$

In these correlations, the Prandtl number ($Pr = c_p\,\mu\,/\,k$) is a function of specific heat capacity (c_p), viscosity (μ) and thermal conductivity (k), while the Nusselt number ($Nu = h\,L\,/\,k$) is a function of the characteristic length scale of the flow system (L), and the Reynolds number ($Re = \rho\,U\,L\,/\,\mu$) is a function of the density (ρ) and the characteristic velocity (U). Therefore specific heat capacity (c_p), thermal conductivity (k), viscosity (μ) and the density (ρ) of the nanofluid - are the basic fluid properties – which are absolutely essential and should be measured with precision accuracy in order to develop correlations for predicting the heat transfer coefficient (h) with sufficient accuracy [21].

Nanofluid literature is replete with experimental measurements of thermal conductivity (that were often contradictory) as well as theoretical models (that were often inadequate). These theoretical models were proposed to explore the origin of the anomalous enhancement of thermal conductivity observed in these experiments [1, 22].

For example, the largest level of enhancement in thermal conductivity has been reported for nanofluid suspensions of carbon nanotubes (CNT) [1-2].

In contrast, the specific heat capacity of nanofluids has not been studied as thoroughly in the literature. Only a limited number of experimental measurements are reported in the literature on the specific heat capacity of nanofluids. These studies were restricted primarily to aqueous nanofluids and the property measurements were performed only at low temperatures (less than 100 °C). In these studies, degradation of the specific heat capacity was observed on addition of the nanoparticles to water or aqueous solutions.

The specific heat capacity of three nanofluids containing aluminum oxide (Al_2O_3), zinc oxide (ZnO), and silicon dioxide (SiO_2) nanoparticles in aqueous solvents were measured by Vajjha and Das (2009) [23]. The aqueous solvents were deionized (DI) water as well as pure ethylene glycol (EG) and DI water mixture (EG:water= 60:40). A new general correlation (i.e., using the simple mixing rule) was developed for the specific heat capacity of the mixture, that was expressed as a function of the particle volumetric concentration, temperature, and the specific heat capacity of both the nanoparticle and the neat solvent. It is interesting to note that the authors did not measure the size of the nanoparticles or perform any materials characterization to verify the level of agglomeration of the nanoparticles both before and after the measurement experiments. It is quite possible that the nanoparticles had agglomerated at higher concentration and had acquired micron-scale sizes. Hence, the stability of the nanofluids in this study was circumspect.

Similar studies were also performed by Zhou and Ni (2008) [24] and Namburu et al. (2007) [25] using aqueous nanofluids of alumina (Al_2O_3) and silica (SiO_2), respectively; where these authors reported similar levels of degradation of the specific heat capacity of the nanofluids with the increase in nanoparticle concentrations. In this study the authors reported that the degradation in specific heat capacity was found to consistent with the simple mixing rule. Again, it is interesting to note that the authors did not measure the size of the nanoparticles or perform any materials characterization to verify the level of agglomeration of the nanoparticles both before and after the measurement experiments. As in the previous study, it is quite possible that the nanoparticles had agglomerated at higher concentrations and had acquired micron-scale sizes. Hence, the stability of the nanofluids in this study was also circumspect. The same erroneous relationship was proposed and assumed to be true for predicting the specific heat capacity of aqueous nanofluids in studies reported by Xuan and Roetzel (2000) [26] as well as by Pak and Cho (1998) [27], without any effort to verify the scientific validity of the proposed models for nanofluids.

Contradicting these results, Nelson et al. (2009) [28] were the first to report dramatic enhancements in the specific heat capacity of nanofluids where organic nanoparticles were dispersed in oil based solvent (Poly Alpha Olefin or “PAO” oil). In this study the authors reported that the specific heat capacity of PAO was enhanced by ~50% on mixing with exfoliated graphite nanoparticles (EGN) at 0.6% mass concentration. The other thermo-physical properties of the PAO-EGN nanofluid were also enhanced dramatically at these minute concentrations. Forced convective heat transfer experiments were also conducted using the PAO-EGN nanofluid. The forced convective heat transfer of the nanofluid was enhanced by ~10% (compared to that for the neat PAO solvent). The forced convective heat transfer experiments were performed using a flow loop apparatus with a pin-fin heat exchanger configuration. This anomaly can be explained to be a result of various nano-scale and molecular level transport phenomena (as opposed to bulk flow behavior). For example, the authors reported that the discrete precipitation of the nanoparticles from the suspension on the heat exchanging surface led to the formation of isolated "nano-fins" which effectively enhanced the surface area for heat transfer – which can be misinterpreted as an enhancement of the heat transfer coefficient due to the observed increase in the effective heat transfer (the erroneous conclusion can arise from the erroneous assumption that the surface area for heat exchange remains constant). Similar erroneous logical deductions for interpreting anomalous experimental data and other counter-intuitive nano-scale transport phenomena are explored in the succeeding discussions.

To begin with, the specific heat capacity of individual nanoparticles is enhanced by ~20% than say, that of a meso-scale particle of the same material. The specific heat capacity of solid nanoparticles was estimated using the Einstein and Debye model by Wang et al. (2006) [29]. This study showed that the nanoparticles have a higher specific heat capacity than the "bulk" material properties (i.e., for meso-scale particles), and the enhancement in specific heat capacity of nanoparticles was estimated to be as much as ~25%. The specific heat capacity of nanostructured amorphous silica (na-SiO_2) was measured by adiabatic calorimetric method over the temperature range 9-354K. The average grain size of two na-SiO_2 samples in this study was characterized and reported to be ~20nm. The corresponding specific surface area was measured for two nanoparticle samples and reported to be $160m^2/g$ (SiO_2-1) and $640m^2/g$ (SiO_2-2). The results indicated that the specific heat capacity enhancement is higher for finer grained nanoparticle samples than those of the coarse-grained silica (SiO_2) nanoparticles; i.e., the specific heat capacity values of SiO_2-2 samples were measured to be higher than those of the SiO_2-1 samples [30].

Several transport mechanisms and associated numerical models have been proposed in the literature for the anomalous enhancements in the measured values of thermal conductivity of nanofluids. The proposed transport mechanisms include the following: (1) simple conduction through the liquid/solid composite, (2) ordered layering of liquid on the surface of a solid nanoparticle, (3) thermal energy transfer due to Brownian motion, (4) thermal energy transfer due to the interparticle potential, (5) thermophoresis, and (6) localized convection due to the Brownian motion of the particles [31]. However, the models (in isolation or in combination) were found to be inadequate since the predicted values from the models did not match the experimental data.

At solid-liquid interfaces the semi-crystalline ordering of liquid molecules has been reported in various studies. The semi-crystalline ordering of the liquid molecules leads to the formation of a “compressed phase” – which is estimated to have an effective thickness of a few nanometers (nm). Using a High Resolution Tunneling Electron Microscope (HRTEM) at a crystalline solid surface – ensembles of liquid molecules were observed to exist in an altered state by Oh et al. (2005) [32]. The liquid molecules were observed to form a semi-crystalline layer where the liquid molecules were aligned in an orderly configuration with a periodicity similar to the inter-atomic distance in the crystal lattice (i.e., of the solid wall). This semi-crystalline layer of solvent molecules was observed in these images (from HRTEM) to adhere to the solid surface as if the liquid molecules were virtually an extension of the underlying crystalline lattice structure and thus had a mass density higher than the liquid phase [32]. This layer with a higher density can be termed as the "compressed phase" (Fig. 1).

Gerardi et al. (2009) [33] observed the structure of a water-based nanofluid with alumina (Al_2O_3) nanoparticles through nuclear magnetic resonance (NMR) measurement. A thin layer of water molecules was found to surround each nanoparticle. The thickness of thin layer was measured to be 1.4nm. Ocko et al. (2011) [34] experimentally measured that the monolayers formed at the bulk alkanol-sapphire interface using X-ray characterization techniques. The authors observed that in the vicinity of the sphere surface, the solvent molecules were densely packed with the surface-normal molecules hydrogen bound to the sapphire. Feibelman (2010) [35] recently reviewed the reports in the literature on the properties of the adsorbed water layer on solid surfaces.

In numerous reports in the literature - based on non-continuum flow regimes and involving molecular dynamics (MD) simulations – a compressed phase was predicted to form on a solid wall and the mass density of this compressed phase was predicted to be significantly higher than the liquid phase density [36]. The MD simulations show that primarily due to Van der Waals type of inter-molecular interactions (adhesive interactions in competition with cohesive interactions) the liquid molecules are observed to form a distinct layer of molecules with lower inter-molecular spacing – thereby forming a layer on the surface of the solid with a higher density. Singh (2010) [37] performed MD simulations of n-Tridecane matrix molecules with a single walled carbon nanotube (SWCNT). The result shows that liquid molecules form a layer on the surface of the SWCNT with a higher density.

In retrospect the existence of such a compressed phase is not counter-intuitive and can be expected by a simple extension of the no-slip boundary condition (that is often invoked in continuum models in fluid mechanics) – to the molecular level. Hence, in nanofluids containing the suspension of the nanoparticles - the liquid molecules adhering to the nanoparticle surface are expected to form a compressed phase that envelopes the nanoparticle and behaves much like a solid phase [38-40].

Xue et al. (2004) [41] studied the effect of liquid layering at the solid-liquid interface on thermal transport using molecular dynamics (MD) simulations. A wetting liquid and a non-wetting liquid were explored to establish the effect of wettability and liquid layering on thermal transport. Yu and Choi (2004) [42] studied the role of interfacial layers in the thermal conductivity enhancement of nanofluids by extending the Hamilton-Crosser model for suspensions of non-spherical particles to include the effect of a solid-liquid interface. Using a generalized empirical shape factor in the renovated Hamilton–Crosser model, it was observed that the solid-liquid interfacial layers play a significant role in the thermal conductivity enhancement of nanofluids.

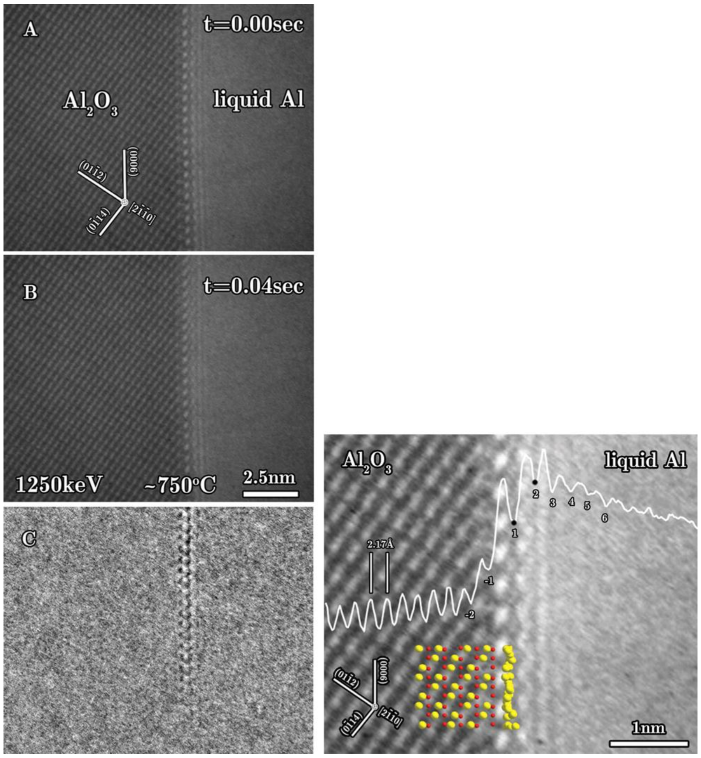

Fig. 1. HRTEM image obtained by Oh et al. (Science, 2005) [32] showing the ordered liquid aluminum molecules at the interface with crystalline sapphire. (LEFT) Frame-by-frame HRTEM images of the solid-liquid interface. The frame images A and B were captured from the real-time movie recorded at ~750℃ in a time sequence of 0.04s. C Difference image obtained by subtracting image A from image B. The difference image clearly shows the formation of a semi-crystalline phase ("compressed phase") at the solid-liquid interface. (RIGHT) Magnified area from a movie image acquired at ~750℃ showing the contrast perturbations in the liquid parallel to the (0006) planes in alumina. The atom positions in the Al_2O_3 (red for oxygen and yellow for aluminum) were determined by contrast matching between simulated and experimental images at different objective lens defocus and specimen thickness values. The first layer of liquid atoms is shown schematically. The white line is an average-intensity line scan perpendicular to the interface. The numbers indicate the minima in intensity, which for the negative numbers correlate to the columns of atoms in the sapphire and for the positive numbers correlate to the intensity perturbations in the Al. The two black points at 1 and 2 indicate identified layers of ordered liquid Al. The white line shows the quantitative distribution of the higher density phase ("compressed phase") that is formed at the solid-liquid interface in Aluminum.[*]

---

[*] Reprinted with permission from "Ordered Liquid Aluminum at the Interface with Sapphire" by S. H. Oh, Y. Kauffmann, C. Scheu, W. D. Kaplan, M. Ruhle, 2005, *Science*, 310, pp. 661-663, Copyright 2005 by the American Association for the Advancement of Science (AAAS).

A closer look at the results from these Molecular Dynamics (MD) simulations shows that the average mass density of this compressed phase approaches the solid phase density of the solvent material. However, the role of the liquid layering ("compressed phase" at the liquid-solid interface) on the total specific heat capacity of the mixture is currently open to interpretation.

This study is therefore focused on investigating the variation of the thermo-physical properties of nitrate salt-based nanomaterials for high temperature applications (e.g., TES for CSP stations). Materials characterization is performed to explore the underlying material transport mechanisms and energy storage modes responsible for the observed results. In addition, analytical and computational studies are performed to explore the role of the material properties of different components in the mixture for the observed experimental data.

The dissertation is divided into five different chapters. The first chapter provides the introduction of CSP stations and TES as well as HTF. In this chapter a brief literature review of nanofluids was provided and their effect on the potential enhancement of system efficiency for CSP stations was provided. In addition, literature review for the formation of compressed phase at the solid-liquid interface was provided.

Chapter II presents the formulation of the analytical model for predicting the specific heat capacity of nanofluids, based on the compressed phase. The specific heat capacity values of four types of nanofluids are calculated using the proposed analytical model. In addition, criteria for maximizing the enhancement in the specific heat capacity are presented based on the predictions from the analytical model. Furthermore, interfacial thermal resistance of various nanofluids is estimated using Molecular Dynamics (MD) simulation. The interfacial thermal resistance (Kapitza resistance) represents a barrier to the transfer of molecular-scale vibrations (micro/nano-scale heat transfer) at the interface between two phases (e.g., between a solid crystalline material and surrounding liquid phase). The values of interfacial thermal resistance are estimated as a function of material properties of the nanoparticle and the solvent as well as the nanoparticle geometry (size, shape, aspect ratio, etc.). The objective of estimating the Kapitza resistance is to estimate the optimum size of the nanoparticles for a specified solvent composition.

Chapter III presents the experimental method and results for measurement of specific heat capacity and viscosity of nitrate salt-based nanomaterials (and that of the neat solvent). These measurements were performed for different nanoparticle material types, mass concentrations and temperatures. The predictions from the numerical models are compared with the experimental data.

Chapter IV presents some of the relevant issues for the application of nanomaterials to CSP/TES systems. Commercial solar thermal systems are introduced and their advantages as well as disadvantages are discussed. In addition, exergy of these nanomaterials is analyzed. Furthermore, some major barriers for their application in conventional/commercial systems are explained.

The final chapter of the dissertation provides a summary of the results obtained in this study. The future directions for this study are also presented.

This study contributes to the field of thermo-fluids research as follows:

(a) The thermo-physical properties of nanomaterials (nanofluids and nanocomposites) were characterized for various heat transfer applications such as thermal energy storage as well as concentrated solar power systems.

(b) Theoretical models were developed for predicting the thermo-physical properties of nanomaterials. (e.g., by utilizing the concepts such as compressed phase, Van der Waals force, Coulombic force interactions in Molecular Dynamics, etc.)

(c) The optimum synthesis method was developed for obtaining colloidal suspensions of well-dispersed nanoparticles in a solvent to maximize the thermal performance. (e.g., by controlling pH, application of surfactant, etc.)

(d) Rheological properties of these nanomaterials were measured and compared with analytical models in the literature (this is the first instance of such measurements for molten salt based nanomaterials).

CHAPTER II

THEORETICAL INVESTIGATION

A. Theoretical Model for Estimating Specific Heat Capacity of Nanofluids

In this study a simple analytical model for the specific heat capacity of nanoparticle suspensions in a liquid (solvent) is explored. The model accounts for the effect of a compressed phase formed at the solid-liquid interface between a spherical nanoparticle and the solvent phase. The total specific heat capacity of the mixture is calculated based on the mass fractions of the three individual components (nanoparticle, solvent and compressed phase). The size and mass fraction of the compressed phase is estimated based on information available in the literature. The nanofluid systems (nanoparticle/ solvent medium) explored in this study are: sapphire/ liquid aluminum, gold/ water, copper/ liquid argon, and silica/ liquid carbonate salt eutectic, respectively. The results show that the properties of the compressed phase (relative to the thermo-physical properties of the nanoparticle and solvent bulk liquid phase) can cause the nanofluid specific heat capacity to increase dramatically (or to decrease). For example, for aqueous nanofluids the specific heat capacity of the mixture decreases on addition of nanoparticles (due to high specific heat capacity of water relative to ice). However, for nanofluids obtained from liquid aluminum and from carbonate salt eutectic – the specific heat capacity is increased on addition of the nanoparticles. In addition, the analytical model suggests that spherical nanoparticles with diameters less than 5-6nm can cause dramatic enhancement in specific heat capacity of the nanofluid, if the specific heat capacity of the compressed phase is higher than that of the liquid phase.

1. Model Formulation

For nanoparticle suspensions in a liquid solvent, the liquid molecules in the vicinity of a nanoparticle surface form a compressed phase. Based on experimental measurements (using HRTEM) and predictions from MD simulations - the thickness of this compressed phase is estimated to range from a few Angstroms (Å) to a few nanometers (nm). The compressed phase forms due to the intermolecular interactions (adhesive forces competing with the cohesive forces) between the solvent molecules and the surface atoms of the nanoparticles. A distinct void layer exists between the solid surface and the compressed phase - due to the competition between the long-range attractive forces and the short range repulsive forces (i.e., equilibrium distance for intermolecular interactions). This void layer is therefore caused by the relative balance between Van Der Waals forces (which are typically modeled by Lennard-Jones type inter-molecular interactions) and the electrostatic interactions. The thickness of the compressed phase enveloping a solid surface and the size of the intervening void layer were culled from various numerical and experimental studies (e.g., Oh et al., 2005 [32]; Xie et al., 2005 [39]; Yu et al., 2000 [40]). The relative size and thermo-physical properties of the compressed phase can affect the overall thermal properties of a nanofluid or a nanocomposite material [2, 39, 42-43].

Oh et al. (2005) [32] employed High Resolution Tunneling Electron Microscope (HRTEM) to visually observe an ordered layer of liquid aluminum (compressed phase) at an interface with solid crystalline sapphire (Fig. 1). The spacing (d_{sl}) between the sapphire atoms (on the surface of the crystal) and the first contrast perturbation in the liquid molecules was measured accurately by Oh et al (2005) [32]. Based on the experimental observations by Oh et al. (2005) [32] – the model used in this study was formulated by considering an ensemble of spherical nanoparticles suspended and dispersed uniformly in a liquid phase. A compressed phase of the solvent molecules of a certain thickness (δ) was assumed to envelope each nanoparticle. An intervening void layer (equilibrium inter-molecular distance) was assumed to exist between the surface of the spherical nanoparticle and the compressed phase of solvent molecules that was assumed to envelope the nanoparticle. The void layer was assumed to have a certain thickness and is represented by the symbol: d_{sl}. Fig. 2 shows the schematic representation of the described model (that was based on the HRTEM image shown in Fig. 1).

The molecules in the compressed phase have a more ordered intermolecular spacing than in the bulk liquid phase [39]. The thickness and the physicochemical properties of this compressed phase would result from the balance between cohesive and adhesive forces – primarily by Van der Waals interactions (and possibly by other types of force fields such as electrostatic and ionic interactions). Therefore, estimating the thermo-physical behaviors of this compressed phase is open to interpretation. Currently there is no available data (experimental or numerical) for estimating the thermo-physical properties of this compressed phase.

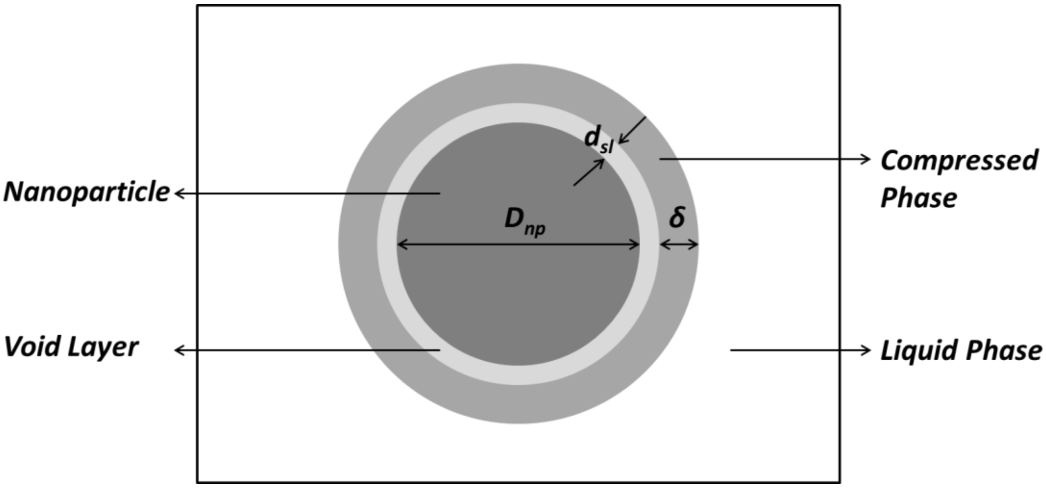

Fig. 2. Schematic showing the compressed phase along with the void layer that envelops a nanoparticle. The nanoparticle is assumed to have a spherical shape.

In this study a simple analytical model for estimating the total specific heat capacity of this suspension was developed by assuming that the compressed phase has the same properties as the solid phase of the solvent material. This analysis is performed for a spherical nanoparticle. The same procedure can be applied to other nanoparticle shapes - such as for cylindrical structures (e.g., CNT) or disk shaped / lamellar structures (such as graphene). For all of these shapes, the thickness of the compressed phase can be estimated using MD simulations.

The material property values of the compressed phase are calculated at the reference temperature corresponding to the melting point of the material. The justification for this assumption is that the results from MD simulation show that the mass density of this compressed phase matches that of the solid phase of the solvent. Hence, by extension the other material properties are expected to be similar to that of the solid phase of the solvent material. In addition, the compressed phase has a semi-crystalline structure that is akin to the structure of the solid phase of the solvent at the melting point. Hence, the material properties of the compressed phase are assumed to correspond to that of the solid phase of the solvent material and at a temperature corresponding to the melting point of the solvent.

Considering a nanofluid suspension with a total mass of M with a mass fraction of the nanoparticles in the mixture to be x, the total mass of nanoparticles is then (Mx). The total number of nanoparticles is then expected to be ($M\,x\,/\,m_n$) and total mass of the compressed phase is then expected to be ($M\,x\,m_s\,/\,m_n$); where m_n is the mass of an individual spherical nanoparticle of diameter (D_{np}) and m_s is the mass of the compressed phase that envelopes an individual nanoparticle. Hence, using an extension of the simple mixing rule the total specific heat capacity (C_{total}) of nanofluid can be expressed as:

$$C_{total} = \frac{[MxC_n] + [\frac{Mx}{m_n} m_s C_s] + [(M - Mx - \frac{Mx}{m_n} m_s) C_l]}{M} \tag{II-1}$$

where C_n, C_s and C_l are the specific heat capacity of nanoparticle, compressed phase and the bulk liquid phase (solvent), respectively. The mass of a spherical nanoparticle of diameter (D_{np}) can be expressed as:

$$m_n = \rho_n V_n = \rho_n \left(\frac{\pi D_{np}^3}{6} \right) \tag{II-2}$$

where ρ_n and V_n are the density and volume of nanoparticle, respectively. The mass of compressed phase enveloping a single nanoparticle can be expressed as:

$$m_s = \rho_s V_s = \rho_s \frac{4}{3}\pi\left[\left(\frac{D_{np}}{2}+\delta+d_{sl}\right)^3-\left(\frac{D_{np}}{2}+d_{sl}\right)^3\right] \tag{II-3}$$

where ρ_s and V_s are the density and volume of compressed phase, respectively.

These equations can be combined to calculate the specific heat capacity of the nanofluid as follows:

$$\begin{aligned} C_{total} = {} & [x]C_n + \left[\left(x\frac{\rho_s}{\rho_n}\right)\left\{\left(1+\frac{2(\delta+d_{sl})}{D_{np}}\right)^3-\left(1+\frac{2d_{sl}}{D_{np}}\right)^3\right\}\right]C_s \\ & + \left[1-x-\left(x\frac{\rho_s}{\rho_n}\right)\left\{\left(1+\frac{2(\delta+d_{sl})}{D_{np}}\right)^3-\left(1+\frac{2d_{sl}}{D_{np}}\right)^3\right\}\right]C_l \end{aligned} \tag{II-4}$$

2. Model Implementation

To ascertain the system temperature for performing the calculations for the nanofluids by using the model outlined by Eq. (II-4), the melting point and boiling point of the neat solvents are evaluated. Melting point and boiling point for the neat solvents explored in this study are listed in Table 1. The total specific heat capacity of the different nanofluids considered in this study - are therefore calculated for different system temperatures, which are chosen to be between the melting point and the boiling point of the neat solvent. The system temperatures used in this study for each nanofluid are also listed in Table 1.

Table 1. Melting point and boiling point for the neat solvents used for choosing the reference temperature for calculation of the total specific heat capacity of nanofluids.

Neat Solvent	Melting Point (K)	Boiling Point (K)	Temperature for calculation (K)
Water	273	373	300
Liquid Aluminum	933.15	2792	1000
Liquid Argon	83.80	87.30	87
Liquid Alkaline metal carbonate salt eutectic	761	-	800

The specific heat capacity of the nanoparticle is expected to be higher than the bulk property values that are usually listed in the conventional material property databases. Since the mass concentration of the nanoparticles in nanofluids are typically less than 5% - the values for the total specific heat capacity of the nanofluid are not found to be affected significantly by using either the bulk values or the actual values for the specific heat capacity of the nanoparticle. However, in the interest of maintaining consistency in the model – the actual property values (i.e., usually the enhanced values) for the nanoparticle are used in Eq. (II-4). The specific heat capacity values of the nanoparticles used in this study are listed in Table 2.

Table 2. Specific heat capacity values for bulk materials and the enhanced specific heat capacity values for the corresponding nanoparticles.

Nanoparticles	*C* of bulk material (J/g-K)	Enhancement (%)	C_n of nanoparticle (J/g-K)
Gold	0.129	17	0.1509
Sapphire	1.2237	0	1.2237
Copper	0.2360	0	0.2360
Silica	1.2266	10	1.3493

Tan et al. (2009) [44] measured the specific heat capacity of a few nanostructured oxides, metals, and zeolites. The specific heat capacity of 40nm nanocrystalline nickel was compared with coarse-grained crystalline nickel. The experimental results show that the specific heat capacity for coarse grained particles varies between 2 and 4% in the temperature range from 100K to 370K. The specific heat capacity of 50nm nanocrystalline copper was observed to be enhanced by 3-17% in the temperature range from 100K to 370K, compared to that of the coarse grained copper. However, in this study the specific heat capacity of copper was not found to be enhanced significantly for the temperature range of 80K to 100K. Hence, the specific heat capacity of copper nanoparticle at a system temperature of 87K is assumed to be the same as that of the bulk material. The specific heat capacity of copper bulk material is 0.2360J/g-K at 87K [44]. In this study, it is assumed that the specific heat capacity of gold nanoparticle is 17% higher than that of gold bulk material based on the numerical studies performed by Wang et al (2006) [29]. The specific heat capacity of gold in the bulk phase is

0.129J/g-K at 300K [20]. The experimental measurements reported for the specific heat capacity of sapphire nanoparticles indicates that no significant enhancement was observed for a temperature range of 75K to 375K [44]. Hence, it is assumed that the specific heat capacity of the sapphire nanoparticles is the same as that of sapphire bulk material at 1000K. The specific heat capacity of sapphire bulk material is 1.2237J/g-K at 1000K [45]. As mentioned before, in a prior study reported in the literature - the molar heat capacity of nanostructured silica (SiO_2) and coarse-grained silica (SiO_2) was measured over the temperature range from 9K to 354K [44]. For two different varieties of SiO_2 nanoparticles with a nominal diameter of 20nm and 40nm the specific surface area was reported to be 160m^2/g (SiO_2-1) and 640m^2/g (SiO_2-2), respectively. The experimental results indicate that the specific heat capacity enhancement for the temperature range of 150K to 350K for nanostructured SiO_2-1 and nanostructured SiO_2-2 are about 2–7% and 4–10% higher than those of coarse-grained SiO_2, respectively. Based on this data it is assumed that the specific heat capacity of SiO_2 nanoparticle is 10% higher than that of SiO_2 bulk material at 800K. The specific heat capacity of SiO_2 bulk material is therefore chosen to be 1.2266J/g-K at 800K [20].

The molecules in the compressed phase that are assumed to envelope the nanoparticle surface are reported to behave like a solid [39-40]. Since there is no available expression (or measured data) for calculating the specific heat capacity of the compressed phase, it is assumed that it has the same properties as the solid phase of the solvent material at the corresponding melting point. The density values of the nanoparticles are assumed to be the same as that of the bulk materials. The thermo-physical property values of the solvent phase, the compressed phase, and the nanoparticle are listed in Table 3.

Table 3. The thermo-physical property values (of the solvent phase, the compressed phase, and the nanoparticles) as well as the thickness of compressed phase and thickness of the void layer (inter-molecular equilibrium distance) used in Eq. (II-4).

Nanofluids	ρ_n (g/cm^3)	ρ_s (g/cm^3)	ρ_l (g/cm^3)	C_n (J/g-K)	C_s (J/g-K)	C_l (J/g-K)	d_{sl} (nm)	δ (nm)
Gold/ Water	19.3^a	0.92^a	0.997^a	0.1509^a	2.04^a	4.179^a	0.326^e	1.0^d
Sapphire/ Liquid Aluminum	3.97^a	2.38^h	2.36^g	1.2237^a	1.2552^a	1.1769^b	0.35$^{f, i}$	1.2$^{f, g}$
Copper/ Liquid Argon	8.96 ^{a}	1.625^j	1.43^k	0.2360^a	1.0254^k	1.078^k	0.2872^l	0.7$^{l, e}$
Silica/ Carbonate salt eutectic ^{n}	2.65^a	1.99^a	1.98^a	1.3493^a	6.0^c	1.6^c	0.3^m	0.8^m

[a] Incropera et al. (2006) [20]; [b] Buyco and Davis (1970) [46]; [c] Araki et al. (1988) [47]; [d] Chang et al. (2008) [48]; [e] Sarkar and Selvam (2007) [49]; [f] Oh et al. (2005) [32]; [g] Buyco and Davis (1970) [46]; [h] Assaela et al. (2006) [50]; [i] Swiler and Loehman (2000) [51]; [j] Dobbs et al. (1957) [52]; [k] Figgins (1960) [53]; [l] Li et al. (2009) [14]; [m] Shin and Banerjee (2009) [15]; [n] Silica/ Liquid phase of alkaline metal carbonate salt eutectic mixture (Li_2CO_3 and K_2CO_3 in 62:38 molar ratio).

Chang et al. (2008) [48] performed MD simulations to investigate the adsorption mechanisms for water molecules on the surface of gold nanoparticles of different sizes. The results of the MD simulations show the enhancement in the local mass density distributions of the oxygen and hydrogen atoms (contributed by the adhered layers of water molecules). Based on this result, it is assumed that the density of the compressed phase (ρ_s) is same as that of ice at its melting point (273K). The density of liquid water is

0.997g/cm^3 at 300K and the density of the compressed phase (ρ_s) is assumed to be 0.92g/cm^3 [20]. The value of C_s in this study is assumed to be 2.04J/g-K which is the value for ice at the melting point [20]. Also, in these simulations it was observed that at a distance greater than ~1nm from the gold nanoparticle surface, the water molecules were found to represent a bulk structure (i.e., disordered structure observed in the liquid phase). Based on this result the thickness of the compressed phase (δ) is assumed to be 1nm. The void layer (d_{sl}) between the surface of the nanoparticle surface and the first molecule in the compressed phase is estimated using the Berthlot mixing rule [49]:

$$d_{sl} = \frac{d_{ss} + d_{ll}}{2} \tag{II-5}$$

where d_{ss} is equilibrium distance of solid-solid molecules and d_{ll} is equilibrium distance of liquid-liquid molecules. Hence, using Eq. (II-5) the value of d_{sl} is estimated to be 0.326nm in the gold/ water nanofluid system. In the case of sapphire/ liquid aluminum nanofluid system, it is assumed that the density of the compressed phase (ρ_s) is same as that of solid aluminum at its melting point (933.47K). The density of liquid aluminum is 0.236g/cm^3 at 1000K and the density of the compressed phase (ρ_s) is 0.238g/cm^3 at 933.47K [50]. The value of C_s in this study is assumed to be 1.2552J/g-K which is the value for solid aluminum at the melting point [46]. Based on the results obtained by Swiler and Loehman (2000) [51] using MD simulations - the thickness of compressed phase (δ) can be estimated to be 1.2nm. This value is consistent with the experimental measurements performed by Oh et al. (2005) [32] using HRTEM, as shown in Fig. 1. The size of the void layer (d_{sl}) between the nanoparticle surface and the first liquid molecule in the compressed phase is obtained from the experimental results reported by

Oh et al. (2005) [32]. The value of d_{sl} is assumed to be 0.35nm for the sapphire/liquid aluminum nanofluid system. Using MD simulations Li et al. (2009) [14] explored the effect of the ordered compressed phase between the liquid argon and copper nanoparticle on the thermal conductivity enhancement. It is assumed that the density of the compressed phase (ρ_s) is same as that of solid argon at its melting point (83.80K). The density of liquid argon is 0.143g/cm^3 at 87K and the density of the compressed phase (ρ_s) is assumed to be 1.625g/cm^3 [52]. The value of C_s in this study is assumed to be 1.0254J/g-K (which is the value for solid argon at the melting point) from the experimental results by Figgins (1960) [53]. Based on the results obtained by Li et al. (2009) [14] using MD simulations - the thickness of compressed phase (δ) can be estimated to be 0.7nm. The size of the void layer (d_{sl}) is obtained using Berthlot mixing rule [14, 49]. The value d_{sl} is 0.287nm in the copper/ liquid argon nanofluid. MD simulation of silica/ liquid phase of alkaline metal carbonate salt eutectic mixture was implemented to investigate the density distribution of the liquid molecules near the nanoparticle of 1nm diameter by Shin and Banerjee (2009) [15]. It is assumed that the density of the compressed phase (ρ_s) is same as that of solid phase of alkaline metal carbonate salt eutectic at its melting point (761K). The density of liquid phase of alkaline metal carbonate salt eutectic is 0.198g/cm^3 at 800K and the density of the compressed phase (ρ_s) is assumed to be 1.990g/cm^3 from the experimental results reported by Araki et al. (1988) [47]. The value of C_s in this study is assumed to be 6.0J/g-K (which is the value for solid phase of alkaline metal carbonate salt eutectic at the melting point) from the experimental results by Araki et al. (1988) [47]. Based on the results of MD simulation (Shin and Banerjee, 2009 [15]) - the thickness of compressed phase (δ) can be estimated to be 0.8nm; and the size of the void layer (d_{sl}) between the nanoparticle surface and the first liquid molecule in the compressed phase is assumed to be 0.3nm.

3. Results and Discussions

Eq. (II-4) was used to calculate the specific heat capacity values of the nanofluids based on property values listed in Table 3. The total specific heat capacity of gold/ water nanofluid increases marginally with the diameter of nanoparticle, but decreases significantly with the mass concentration of nanoparticle, as shown Fig. 3 (a). These values of the specific heat capacity of the nanofluid are significantly below that of water. This is because the specific heat capacity of water is much higher than that of nanoparticle as well as the compressed phase. For gold/ water nanofluid, it is assumed that the specific heat capacity of the compressed phase is same as that of ice (i.e., 2.04J/g-K). The compressed phase has marginal effect on the total specific heat capacity of gold/ water nanofluid because the density of the compressed phase is much smaller than that of the nanoparticle (cf. Eq. (II-4)).

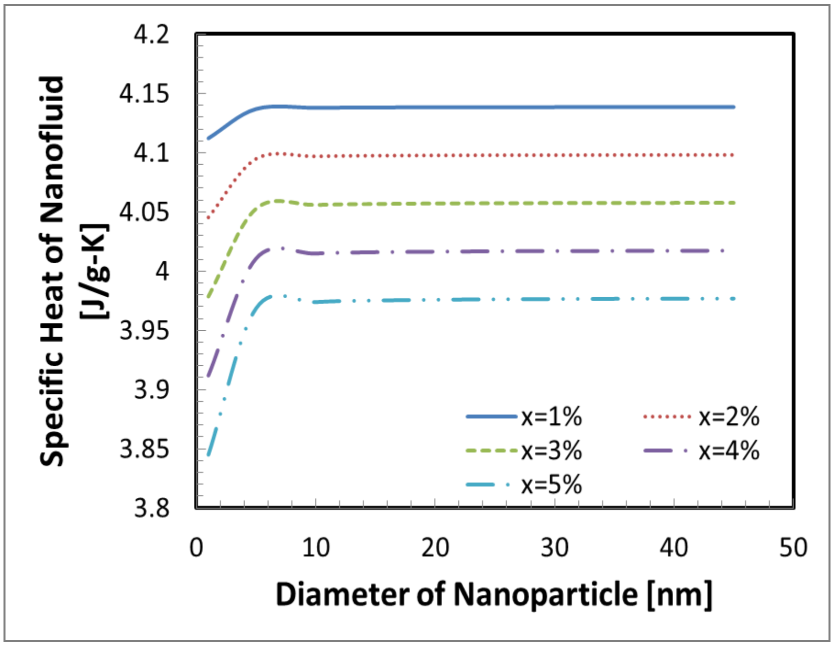

(a)

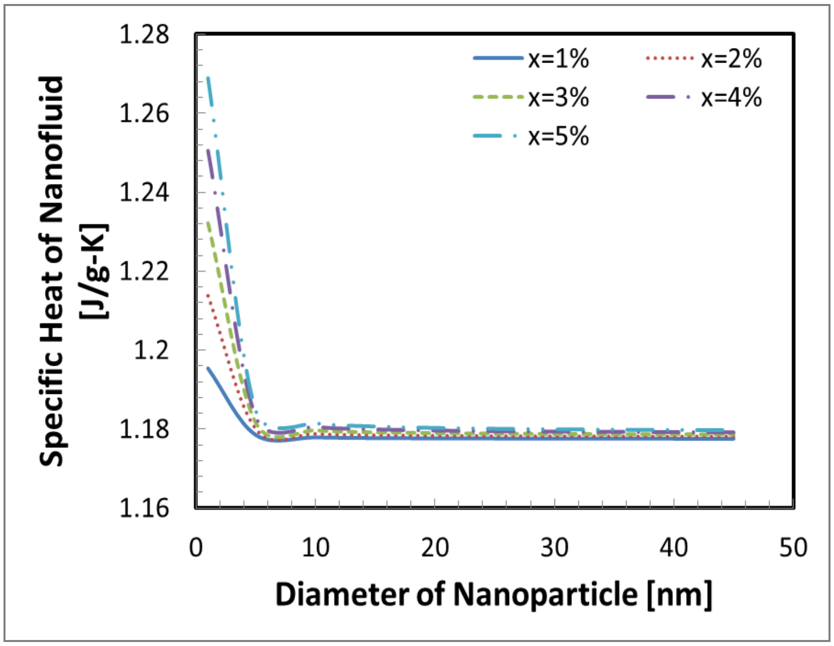

(b)

Fig. 3. Variation of specific heat capacity values of nanofluids with diameter of nanoparticle and mass concentrations (a) gold/ water nanofluid, (b) sapphire/ liquid aluminum, (c) copper/ liquid argon, (d) silica/liquid carbonate salt eutectic.

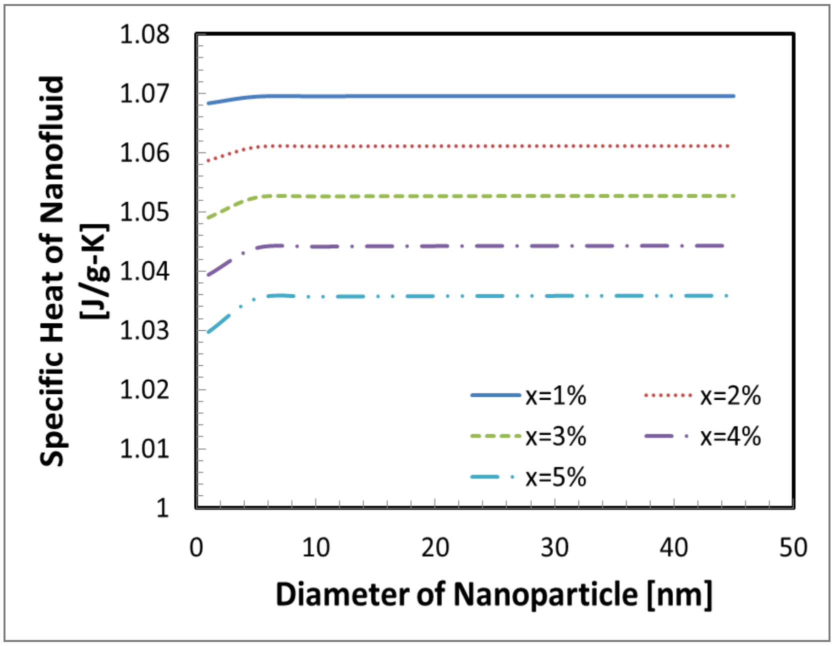

(c)

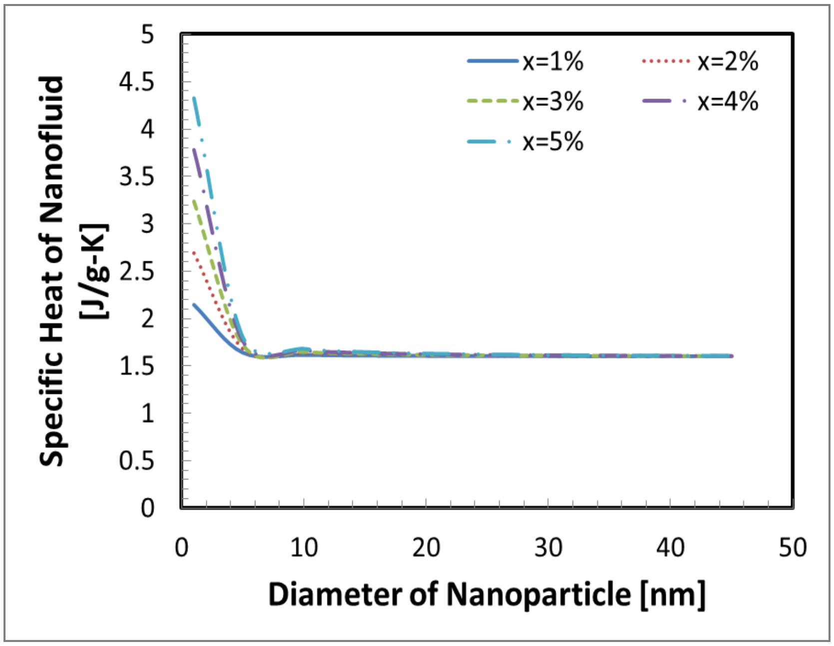

(d)

Fig. 3. Continued

In contrast, the total specific heat capacity of sapphire/ liquid aluminum nanofluid decreases with the diameter of the nanoparticle, but increases with mass concentration of nanoparticle as shown Fig. 3 (b). These values of the specific heat capacity of the nanofluid are significantly enhanced to that of pure liquid aluminum. This is because the specific heat capacity of sapphire nanoparticle is higher than that of liquid aluminum and the specific heat capacity of compressed phase is also higher than that of liquid aluminum. The enhancements are more significant at higher concentrations and are more sensitive at smaller nanoparticle sizes. However, there is only marginal enhancement of the specific heat capacity of the nanofluid for nanoparticle size exceeding 10nm. Also, the density of the compressed phase is similar to that of the liquid phase and significantly lower than the nanoparticle density. The total specific heat capacity of nanofluid marginally increases, primarily due to the large density ratio between the nanoparticle and the compressed phase.

The total specific heat capacity of copper/ liquid argon nanofluid slightly increases with the diameter of the nanoparticle, and significantly decreases with the mass concentration of the nanoparticle as shown Fig. 3 (c). These values of the specific heat capacity are significantly lower than that of pure liquid argon. This is because the specific heat capacity of liquid argon is much higher than that of the nanoparticle as well as the compressed phase. The total specific heat capacity of nanofluid is not affected by the specific heat capacity of the compressed phase. This is due to the high density of the nanoparticle in relation to the density of the compressed phase as well as due to the low specific heat capacity value of the compressed phase.

The total specific heat capacity of silica/ liquid carbonate eutectic nanofluid is explored next. The liquid phase of the alkaline metal carbonate salt eutectic (Li_2CO_3:K_2CO_3 = 62:38 in molar ratio) mixture has a similar density as the compressed phase but a much lower specific heat capacity than the compressed phase. The nanoparticle has a higher density than the eutectic material (for both solid and liquid phases) but has a much lower value of the specific heat capacity. The calculations based on Eq. (II-4) and Table 3 shows that the total specific heat capacity of the nanofluid decreases with the size of the nanoparticle, but increases significantly with the mass concentration of nanoparticle as shown Fig. 3 (d). The enhancement in the values of the specific heat capacity for the nanofluid is more sensitive for smaller nanoparticles. For nanoparticle diameters exceeding 20nm no significant enhancement in specific heat capacity is observed, even with increase in concentration of the nanoparticles. This anomalous trend can be explained based on the relative density ratio between the nanoparticle and the compressed phase and the high specific heat capacity of the compressed phase. The thickness of the compressed phase is independent of the size of the nanoparticle. Hence, the compressed phase is more effective in enhancing the specific heat capacity of the nanofluid for smaller nanoparticles. The relative contribution of the compressed phase on the overall specific heat capacity is increased when the particle size is reduced – due to the marginally higher density and relatively high value of the specific heat capacity for the compressed phase compared to the liquid phase. Ironically, even though the nanoparticle has a lower specific heat capacity value, the contribution from the compressed phase confounds the contribution from the nanoparticle to the total specific heat capacity values.

Bergman (2009) [54] predicted that in cooling applications involving forced convection, the efficacy of the nanofluids is enhanced at lower flow rates whereas the nanofluids can lead to degradation in heat transfer at higher values of flow rates (when compared with the pure solvent such as water or refrigerants). This analysis was based on the experimentally observed degradation in specific heat capacity of aqueous nanofluids as well analytical estimates for specific heat capacity of nanofluids based on the thermodynamic mixture rules for fluids that were applied to nanoparticle-solvent mixtures. These mixture rules only accounted for the specific heat capacity of the nanoparticle and the neat solvent, while neglecting the contribution from the compressed phase. The analyses performed in our study show that the nanofluids with enhanced specific heat capacity will have substantially better efficacy in cooling applications for all flow rates (compared to the neat solvent). In addition, the nanofluids with enhanced specific heat capacity (compared to the neat solvent) may be an attractive option for thermal energy storage applications.

On closer examination of Eq. (II-4) and after simplification of the various terms, it is observed that C_s is weighed by a product of two factors: (a) [$x\ \rho_s/\rho_n$]; and (b) [$6\delta/D_{np}$] (i.e., after neglecting higher powers or products of [δ/D_{np}] and [d_{sl}/D_{np}]). The first term shows that the relative density ratio of the nanoparticle and the compressed phase plays a decisive role in determining the enhancement of the specific heat capacity of the nanofluid. The second term shows that the contribution from the material properties of the compressed phase towards the specific heat capacity of the nanofluid is enhanced significantly for nanoparticles smaller than a certain size determined by the value of δ. Examination of the values for d_{sl} and in Table 3 shows that typically d_{sl} ~ 0.3 nm, whereas typically δ ~ 1nm. Hence, for spherical nanoparticles that are smaller than 5-6nm diameter the contribution from the compressed phase is enhanced dramatically in augmenting the specific heat capacity of the nanofluid.

Based on the results from this study the following criteria are identified for the purpose of enhancing the specific heat capacity of the nanofluid:

(a) The specific heat capacity of the compressed phase should be higher than the liquid phase.

(b) It is beneficial to have the nanoparticle specific heat capacity to be higher than the specific heat capacity of the liquid phase, but it is not a necessary condition (e.g., for the silica/ liquid carbonate eutectic nanofluid). It is not necessary for the nanoparticle to have a higher specific heat capacity in enhancing the specific heat capacity of the nanofluid, provided the compressed phase has a higher specific heat capacity.

(c) The nanoparticle diameter should be below a certain critical threshold (that is determined by six times the thickness of the compressed phase). Since the thickness of the compressed phase is typically ~ 1nm the critical threshold is universally expected to be ~ 5-6nm.

(d) The density of the nanoparticle should be as small as possible. If the density of the nanoparticle is significantly higher than the density of the compressed phase, the compressed phase will have marginal effect on the specific heat capacity of the nanofluid.

Hence, from a global perspective – it is essential to choose a solvent whose solid phase properties (at or near the melting point) are significantly higher than the liquid phase properties. At the same time, the nanoparticle density should be as low as possible.

4. Summary and Implications

In this study, a simple analytical model is developed for calculating the total specific heat capacity of a nanofluid as a function of the nanoparticle mass concentration and nanoparticle diameter, by considering the contribution from the compressed phase enveloping a spherical nanoparticle. The total specific heat capacity of nanofluids is calculated for gold/ water, sapphire/ liquid aluminum, copper/ liquid argon, and silica /liquid carbonate eutectic (for alkaline metal carbonate salt eutectic of Li_2CO_3:K_2CO_3 at a molar ratio of 62:38).

The results from this analytical model show that the properties that should be considered for evaluating the specific heat capacity of a nanofluid are:

(a) the individual specific heat capacity values of the components (i.e., for nanoparticle, liquid phase and compressed phase),

(b) the density values of the components (i.e., for nanoparticle, liquid phase and compressed phase),

(c) the thickness of the compressed phase (typically ~ 1nm), and

(d) the diameter of the spherical nanoparticles.

For enhancing the specific heat capacity of the nanofluid involving spherical nanoparticles:

(a) The specific heat capacity of the compressed phase should be higher than that of the liquid phase.

(b) The density of the nanoparticles should be as low as possible.

(c) The density ratio of the compressed phase to that of the nanoparticle should be maximized.

(d) The nanoparticle size should be minimized below a critical threshold (typically 5-6nm).

The results show that for spherical nanoparticles smaller than 5-6nm diameter the contribution from the compressed phase are more pronounced in augmenting or reducing the total specific heat capacity values for a nanofluid.

B. Interfacial Thermal Resistance of Nitrate Salt-based Nanofluids

In cooling applications (especially those involving phase change), modifications of the heat exchanging surface characteristics can enhance heat transfer. Experimental results show that surfaces coated with carbon nanotubes (CNT) enhanced the critical heat flux (CHF) in pool boiling by ~60% [55-56]. Boiling experiments by Sriraman et al. (2007) [57] indicate that silicon nano-fins on a silicon surface enhanced CHF by as much as ~120%. CHF enhancement has also been reported for experiments using nanofluids [1, 21, 28, 58-59]. These nanoparticles precipitate on the heater surface to form nano-fins leading to heat transfer enhancement [60]. Hence, the formation of nano-fins on the heat exchanging surface can lead to enhancement of heat transfer. However, the enhancement in the case of silicon nano-fins is higher than in the case of carbon nanotubes as mentioned above. The thermal conductivity of silicon is 150W/m-K [61] whereas the thermal conductivity of carbon nanotubes is ~3000W/m-K for multi-walled nanotubes [62] and ~6000W/m-K for single wall nanotubes [63]. A potential reason for this counter-intuitive behavior is the existence and dominance of the interfacial thermal resistance (Kapitza resistance). Kapitza resistance impedes the propagation of molecular vibrations (i.e., nano-scale or molecular scale heat transfer) from the surface atoms of nano-fins to the surrounding fluid molecules. This arises from the different rates of propagation of the thermal vibrations in different media – resulting in the scattering and loss of the wave energy at the interface between two different materials (even if they are in perfect thermal contact, i.e., even if the thermal contact resistance is zero).

Turanov and Tolmachev (2009) [64] explored the effect of the interfacial thermal resistance on material diffusion. The solvent self-diffusion coefficient (SDC) in aqueous suspensions of quasi-monodisperse spherical silica nanoparticles was found to decrease with nanoparticle volume fraction. The rate of decrease was estimated to occur at a faster rate than predicted by the effective medium theory. These anomalous deviations were explained to be due to the effect of the interfacial thermal resistance. This shows that the effective material properties of nanomaterials and the associated transport phenomena are strongly affected by the interfacial properties (i.e., parameters such as Kapitza resistance).

Hence, in this study the effect of interfacial thermal resistance was estimated for nanomaterials composed of nitrate salt mixed with nanoparticles. The values of the interfacial thermal resistance for various nanofluid compositions were investigated using Molecular Dynamics (MD) simulation. Potassium nitrate (KNO_3) and sodium nitrate ($NaNO_3$) mixture is used as the solvent in these studies. The Kapitza resistance for various nanoparticles – such as alumina (Al_2O_3), silica (SiO_2), silicon carbide (SiC), and single walled carbon nanotube (SWCNT) was calculated using MD simulations as a function of the nanoparticle size and the system temperature. For comparing the Kapitza resistance values of nitrate salt with carbonate salt, additional MD simulations were performed using solvent phase to be composed of molten salt based on carbonate salt eutectic (Li_2CO_3:K_2CO_3 = 62:38 in molar ratio) and mixed with SWCNT.

1. Molecular Dynamics (MD) Simulation

MD simulations are typically performed by numerically solving the Newton's equations of motion for a set of atoms and molecules confined within a simulation domain (i.e., the model system). The MD simulations are used to obtain the temporal evolution of positions and velocities of individual atoms in the model system. MD simulations can provide insight into molecular scale transport phenomena – which are otherwise impossible to measure (or monitor) in experiments. The Newton’s equations of motion are too complex to integrate, so numerical integration techniques are typically used in MD simulations. A number of schemes are available but the two most commonly used are Verlet Algorithm and Gear Predictor-Corrector [37]. In this study, Verlet algorithm was used. Force field or potential energy functions (which are simplified mathematical equations) are used to simulate the intermolecular interactions in MD simulations. The total potential energy of a system is the sum of bonded and non-bonded interactions. The Lennard-Jones potential and Coulomb potentials are used for non-bonded interactions, and are expressed as:

$$E = 4\varepsilon\left[\left(\frac{\sigma}{r_{ij}}\right)^{12} - \left(\frac{\sigma}{r_{ij}}\right)^{6}\right] + \frac{q_i q_j}{r_{ij}} \qquad \text{(II-6)}$$

where q_i and q_j are partial charges, σ is collision diameter (units of length), ε is the dissociation energy, and r_{ij} is the distance between the atoms.

For simulating the bonded interactions of, harmonic style functions are used, which is expressed below:

$$E = K_b(r - r_0)^2 + \mathrm{K}_\theta(\theta - \theta_0)^2 + \mathrm{K}_\psi(\psi - \psi_0)^2 \qquad \text{(II-7)}$$

where r_0 is the equilibrium bond distance, θ_0 is the equilibrium value of the angle, and ψ_0 is the equilibrium value of the improper angle. For the bonded interactions of a nanoparticle, harmonic and Consistent Valence Force Field (CVFF) styles are used:

$$E = K_b(r - r_0)^2 + \mathrm{K}_\theta(\theta - \theta_0)^2 + \mathrm{K}_\phi\left[1 + d\cos(n\phi)\right] \qquad \text{(II-8)}$$

Table 4 lists the parameters of nitrate salt (KNO_3 and $NaNO_3$) that are used for MD simulation. These parameters were culled from literature [65-67]. Table 5 lists the parameters that are used for the MD simulations – corresponding to the material properties of the constituent atoms (or molecules) of the nanoparticles. These parameters were obtained from the standard library of Materials Studio (Accelrys, Inc., 2008) and other literature reports [68-69]. Bonded parameters of nanoparticles were generated from the standard library of Material Studio (Accelrys, Inc., 2008).

Table 4. Parameters for intermolecular interactions for the solvent materials: Potassium Nitrate (KNO_3) and Sodium Nitrate ($NaNO_3$).

Non-bonded Interaction	ε_{ii} (kcal/mol)	σ_{ii} (Å)	q_i (e)
O-O	0.15500	3.1540	-0.62
N-N	0.20000	3.9000	+0.86
K-K	0.08000	2.7600	+1.00
Na-Na	0.08600	2.7300	+1.00
Bonded Interaction			
Bonds	K_b (kcal/mol Å $^{-2}$) = 525.0	r_0 (Å) = 1.2676	
Angles	K_θ (kcal/mol rad^{-2}) = 105.0	θ_0 (deg) = 120.0	
Improper	K_ψ (kcal/mol rad^{-2}) = 60.0	ψ_0 (deg) = 0	

The cross terms were computed using the following mixing rules:
$\varepsilon_{ij} = (\varepsilon_{ii}\,\varepsilon_{jj})^{1/2}$, $1/\sigma_{ij} = 1/\sigma_{ii} + 1/\sigma_{jj}$.

Table 5. Parameters for intermolecular interactions for various materials (used as nanoparticles).

Nanoparticle	Interaction	ε_{ii} (kcal/mol)	σ_{ii} (Å)	q_i (e)
Al_2O_3	Al-Al	0.04002	4.05324	+1.4175
	O-O	0.22800	2.8598	-0.9450
SiO_2	Si-Si	0.04002	4.05324	+0.300 +0.450
	O-O	0.22800	2.8598	-0.300 -0.150 0
SiC	Si-Si	0.04002	4.0534	0
	C-C	0.16000	3.4745	0
CNT	C-C	0.43960	3.8510	0

2. Time Constant for Temperature Decay

The interfacial thermal resistance represents a barrier to heat transfer between two phases or two dissimilar materials. In a model proposed by Huxtable et al. (2003) [70], lumped capacitance analyses were used to predict the temperature decay of an individual CNT nanoparticle (that is heated) while losing heat to a surrounding colder fluid. The temperature of the nanoparticle was predicted by the model to exponentially decay with time. The decay time constant, τ, is given by:

$$\tau = \frac{C}{A_s G} = \frac{\rho V c_p R_b}{A_s} \tag{II-9}$$

where C is the total heat capacity, A_s is the total surface area of the nanoparticle, G is the interfacial conductance (inverse of the Kapitza resistance, R_b), ρ is the density of the nanoparticle, V is volume of the nanoparticle, c_p is the specific heat capacity, and R_b is interfacial thermal resistance. Hence, the interfacial thermal resistance, R_b, can be calculated if the time constant, τ, (for rate of temperature decay) can be estimated, since the other parameters are material (or geometrical) properties which can be estimated by consulting standard tables for material properties that are available in the literature. The time constant is estimated using MD simulations. The temperature of the nanoparticle is plotted as a function of time (based on results obtained from the MD simulations) and the slope of the curve plotted in the graph is the time constant for temperature decay.

3. Effect of Size of the Nanoparticle

For a carbon nanotube (CNT) suspension in a fluid - the effective thermal conductivity can be calculated using a model involving a long circular cylinder oriented perpendicular to the direction of heat transfer. This model was proposed by Hasselman and Johnson [71] and is expressed as:

$$\frac{k_{eff}}{k_b} = \frac{\left(\frac{k_{np}}{k_b} - 1 - \frac{2k_{np}R_b}{d}\right)\cdot V_{np} + \left(\frac{k_{np}}{k_b} + 1 + \frac{2k_{np}R_b}{d}\right)}{-\left(\frac{k_{np}}{k_b} - 1 - \frac{2k_{np}R_b}{d}\right)\cdot V_{np} + \left(\frac{k_{np}}{k_b} + 1 + \frac{2k_{np}R_b}{d}\right)} \qquad \text{(II-10)}$$

where k_{eff} is the effective thermal conductivity of the nanofluid, k_b is the thermal conductivity of the base fluid, k_{np} is the thermal conductivity of the nanotube, R_b is the interfacial thermal resistance, V_{np} is the volume concentration of the carbon nanotube, and d is the diameter of the carbon nanotube. By assuming $k_{np} >> k_b$, the Eq. (II-10) is simplified as:

$$\frac{k_{eff}}{k_b} = \frac{\left(1 - \frac{2k_bR_b}{d}\right)\cdot V_{np} + \left(1 + \frac{2k_bR_b}{d}\right)}{-\left(1 - \frac{2k_bR_b}{d}\right)\cdot V_{np} + \left(1 + \frac{2k_bR_b}{d}\right)} \qquad \text{(II-11)}$$

In the Eq. (II-11), the diameter of the nanotube, d, should be higher than $2R_bk_b$ in order to obviate the effect of the interfacial thermal resistance,

$$d_c > 2R_bk_b \qquad \text{(II-12)}$$

For a spherical nanoparticle suspension in a fluid, the effective thermal conductivity can be expressed as follows [71].

$$\frac{k_{eff}}{k_b}=\frac{\left(k_p\left(1+\frac{4R_bk_b}{d}\right)+2k_b\right)+2V_p\left(k_p\left(1-\frac{2R_bk_b}{d}\right)-k_b\right)}{\left(k_p\left(1+\frac{4R_bk_b}{d}\right)+2k_b\right)-V_p\left(k_p\left(1-\frac{2R_bk_b}{d}\right)-k_b\right)} \tag{II-13}$$

For enhancing the effective thermal conductivity by mixing with spherical nanoparticles, the following condition should be satisfied:

$$d_c>\frac{2R_bk_b}{1-\frac{k_b}{k_p}} \tag{II-14}$$

Eq. (II-12) shows that the optimum diameter (d_c) of the nanotube is a function of the interfacial thermal resistance (R_b) and the thermal conductivity of the fluid (k_b). Eq. (II-14) shows that the optimum diameter (d_c) of the nanoparticle is a function of the interfacial thermal resistance (R_b), the thermal conductivity of the fluid (k_b), and the thermal conductivity of the nanoparticle (k_p). Hence, it is necessary to compute the interfacial thermal resistance between a nanoparticle and the solvent (fluid) in order to estimate the optimum size of the nanoparticle.

4. Simulation Procedure

In this section the numerical procedures that were implemented in this study for performing the MD simulations are described. The first step in the simulations is to mathematically specify the contents, material configurations and extents of the simulation domain. The domain is prepared by placing a nanoparticle (SWCNT) of a chosen size at the center of the simulation box. The solvent molecules are placed within the simulation domain and surrounding the nanoparticle. Fig. 4 shows a typical simulation domain used in this study. After placing the SWCNT nanoparticle in the center of the simulation domain - the solvent molecules are placed in the remaining volume of the simulation box. The solvent is composed of 900 molecules of potassium nitrate (KNO_3) and 600 molecules of sodium nitrate ($NaNO_3$) to correspond to the molar ratio of the molten salt eutectic. The numerical procedure for specifying the simulation domain is implemented using Materials Studio (Accelrys, Inc., 2008), a commercial software tool. This simulation domain is then exported in the Materials Studio (MS) data format and a script file is then used to convert the numerical information from the MS data format to the LAMMPS input file. All the simulations were then performed using the LAMMPS software [72].

The potential energy of the system (bonded and non-bonded potential energy) is then minimized in the numerical procedure - in order to eliminate non-physical situations (such as, the matrix molecules that are co-located/ overlapped or are located at a distance closer than the equilibrium molecular distance). The kinetic energy of the system is not considered during minimization, since the effective temperature of the system for this numerical procedure is 0K. In this study, the minimization procedure is implemented in two steps. Initially, the nanoparticle within the simulation domain is placed at a fixed location (i.e., at the center of the simulation domain) and the energy of the surrounding solvent molecules is minimized. Then, the nanoparticle is relaxed and the whole system is allowed to equilibrate. Equilibration step is then followed by global energy minimization. After the minimization step is completed, the system has zero energy and is therefore theoretically at 0K (as mentioned before).

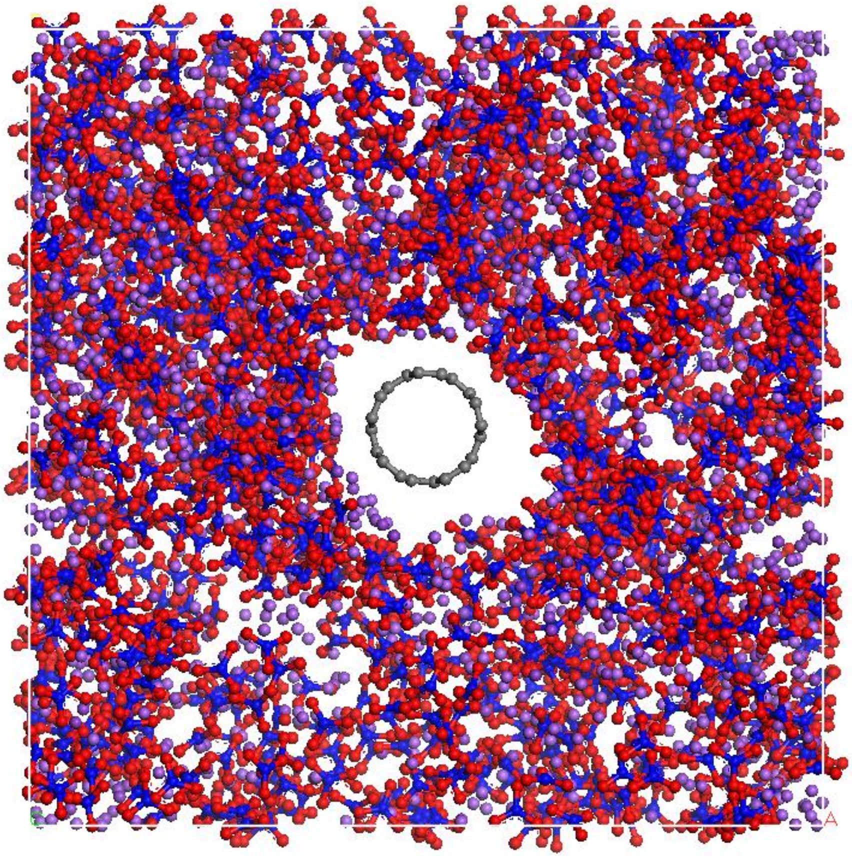

Fig. 4. Simulation domain showing SWCNT nanoparticle placed in the center and the solvent molecules (nitrate salt) located around the crystal lattice of the nanoparticle.

To estimate the Kapitza resistance of the nanoparticle using MD simulations, the system temperature is increased uniformly to 600K (by imposing kinetic energy to the individual atoms within the simulation domain). An equilibration step is performed, and this is implemented in two steps. In the first step, velocities are assigned to the atoms randomly at 600K, and the system is allowed to relax as a NVE ensemble with time step of 0.5fs. In this study, 600K is chosen as the initial temperature in order to obtain liquid phase of the solvent (molten salt) - due to the physical restrictions imposed by the high melting point of the nitrate salt mixture (500K). The system is then equilibrated to a starting temperature by NPT integration.

To calculate the interfacial thermal resistance between a nanoparticle and surrounding solvent, only the nanoparticle is then heated up to a specified temperature (1400K) while the surrounding solvent is maintained at 600K. The nanoparticle is then allowed to lose heat to the surrounding solvent. The rate of decay of temperature of the nanoparticle is then monitored at fixed intervals of time.

5. Results and Discussions

MD simulations were performed to determine the interfacial thermal resistance between a nanoparticle and the surrounding solvent. The solvent composition chosen in in this study are: (1) KNO_3:$NaNO_3$=60:40 in molar ratio, and (2) KNO_3:$NaNO_3$=40:60 in molar ratio. For these solvent compositions, the Kapitza resistance values of different nanoparticle materials were then explored in this study, such as: Alumina (Al_2O_3), silica (SiO_2), silicon carbide (SiC), and single walled carbon nanotube (SWCNT).

Fig. 5 shows the representative data for temperature decay obtained from these simulations. The results shown in this figure correspond to that of Al_2O_3 nanoparticle and solvent composition consisting of KNO_3:$NaNO_3$ = 60:40 in molar ratio. From the plot it is observed that the temperature of the solvent molecules is almost constant (further confirming the validity of applying the lumped capacitance analyses in the model formulation). In the plots it is observed that the difference of temperature between a nanoparticle and solvent molecules decays exponentially – which is consistent with the lumped capacitance assumption. The exponential decay in temperature profile occurs due to the resistance to heat transfer (Kapitza resistance) from the hot nanoparticle to the surrounding colder solvent molecules. Since the plot validates the applicability of lumped capacitance analysis, hence the interfacial thermal resistance (Kapitza resistance) between the nanoparticle to the solvent molecules is calculated using Eq. (II-9). The relaxation time constant is obtained from the slope of the temperature decay (from the logarithmic plot).

Fig. 6 shows the plots for temperature decay of a hot SiO_2 nanoparticle surrounded by colder solvent molecules (KNO_3:$NaNO_3$=60:40 in molar ratio). Fig. 7 shows the plots for temperature decay of a hot SiC nanoparticle surrounded by colder solvent molecules (KNO_3:$NaNO_3$=60:40 in molar ratio). Fig. 8 shows the plots for temperature decay of a hot SWCNT nanoparticle surrounded by colder solvent molecules (KNO_3:$NaNO_3$=60:40 in molar ratio). Based on the time constant obtained from these plots the corresponding values of the Kapitza resistance were calculated and are listed in Table 6.

The results show that the Kapitza resistance values are independent of the nanoparticle size. The Kapitza resistance of SWCNT is calculated to be the highest. The interfacial thermal resistance of Al_2O_3 nanoparticle is similar in magnitude to those of SiO_2 nanoparticle. The Kapitza resistance of the SiC nanoparticle is higher than that of the oxide nanoparticle. Hence, this demonstrates that the enhancement in thermal properties (as well as heat transfer) for the case of nanofluids containing silicon based nanoparticles (or nanocoatings on heat exchanging surfaces) is higher than those of the SWCNT. This result is counterintuitive since the thermal conductivity of silicon is significantly lower than that of SWCNT.

Fig. 9 shows the temperature variation of SWCNT nanoparticles and the solvent molecules where the composition of the solvent was varied. The calculated values of the interfacial thermal resistance obtained from these MD simulations are summarized in Table 7. The results show that the values of the Kapitza resistance do not vary significantly (i.e., a clear trend was not be observed) with the composition of the solvent. Fig. 10 shows the temperature variation of SWCNT nanoparticle and solvent molecules composed of alkali carbonate salt (Li_2CO_3:K_2CO_3=62:38 in molar ratio). The result for the interfacial thermal resistance for this simulation is summarized in Table 8. The results show that the carbonate salt provides a smaller interfacial thermal resistance than the nitrate salt – for the same nanoparticle (i.e., SWCNT).

The optimum nanoparticle size can be computed using Eq. (II-12) and (II-14) based on the value of the interfacial thermal resistance. The lower limit of the nanoparticle diameter is shown in Table 6.

In addition, from the simulation results a density plot is generated to visualize the spatial variation of density within the simulation domain. The density plot along the radial direction from the SWCNT surface is shown in Fig. 11. The peak at 4Å indicates the formation of a layer of molten salt molecules on the surface of the SWCNT. As mentioned in previous section, layering of the liquid molecules is one of the factors for the enhanced effective thermal conductivity of the nanofluids. Furthermore, the peak at 4Å using small SWCNT (6.78Å in diameter) is identical to that using the bigger SWCNT (9.49Å in diameter), which implies that the formation of the compressed phase (higher density layer) of the liquid molecules around the individual SWCNT crystals is independent of the size of the individual nanoparticle. It depends on the interaction (potential field) between carbon atoms at the surface of SWCNT and the liquid molecules (in the molten salt). This is also consistent with the previous statement that the interfacial thermal resistance is independent of the size of the CNT.

In addition, atomic concentration of each atom was predicted by the simulation as shown in Fig. 11. It was observed that the chemical composition of the KNO_3 molecules and $NaNO_3$ molecules in the compressed phase is different from that of the bulk of the mixture (solvent phase). The compressed phase is expected to melt at higher temperature than the bulk phase of the mixture. This result from the numerical models therefore implies the existence of compressed (semisolid) phase surrounding nanoparticles in the nanofluid samples.

Hence, in summary – MD simulations were performed to calculate the interfacial thermal resistance between a nanoparticle and surrounding solvent molecules. From the results, it can be concluded that

(a) The interfacial thermal resistance is independent on the nanoparticle size.

(b) The interfacial thermal resistance is weakly dependent on the chemical composition of the solvent molecules – for alkali-nitrate molten salt chosen for this study.

(c) The interfacial thermal resistance between a SWCNT nanoparticle and nitrate salt mixture is the highest among the nanofluid systems investigated in this study.

(d) Carbonate-based nanofluid with SWCNT has lower interfacial thermal resistance compared to nitrate-based nanofluids with SWCNT.

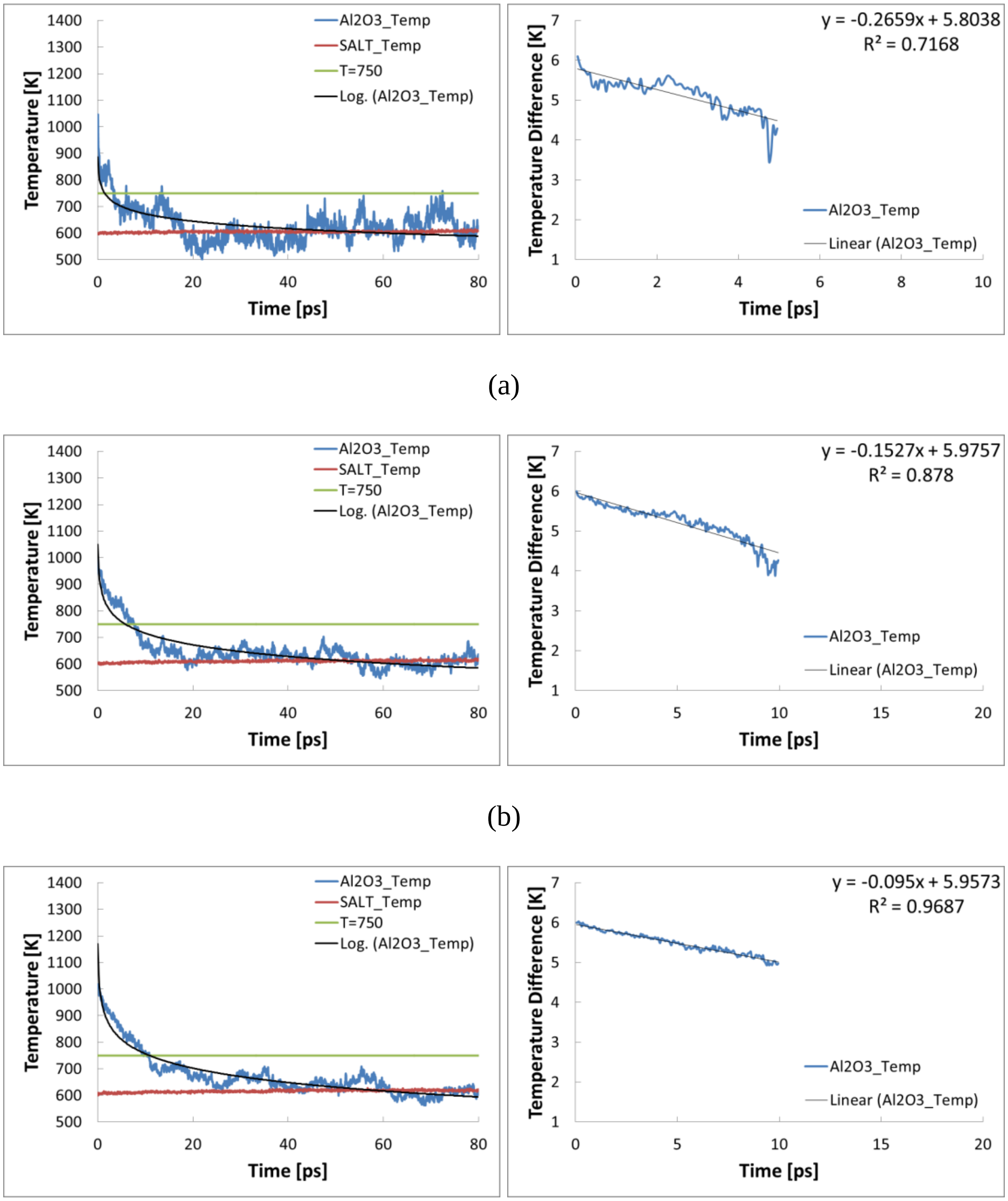

(a)

(b)

(c)

Fig. 5. Temporal variation of temperature: Al_2O_3/Nitrate salt mixture nanofluid (KNO_3:$NaNO_3$=60:40 in molar ratio) (a) radius of Al_2O_3 nanoparticle = 5Å , (b) radius of Al_2O_3 nanoparticle = 6Å , (c) radius of Al_2O_3 nanoparticle = 7Å .

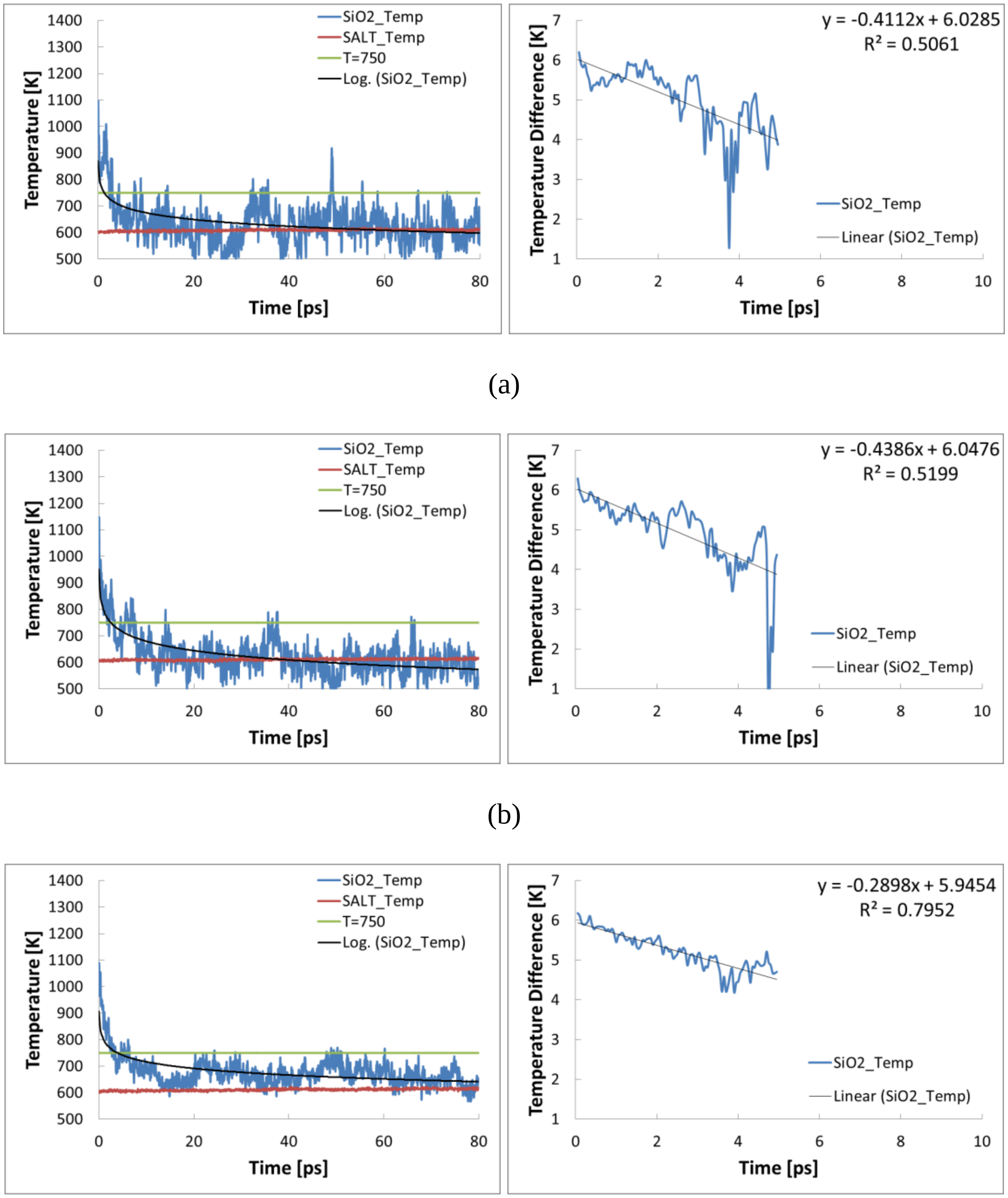

(a)

(b)

(c)

Fig. 6. Temporal variation of temperature: SiO_2/Nitrate salt mixture nanofluid (KNO_3:$NaNO_3$=60:40 in molar ratio) (a) radius of SiO_2 nanoparticle = 5Å, (b) radius of SiO_2 nanoparticle = 6Å, (c) radius of SiO_2 nanoparticle = 7Å.

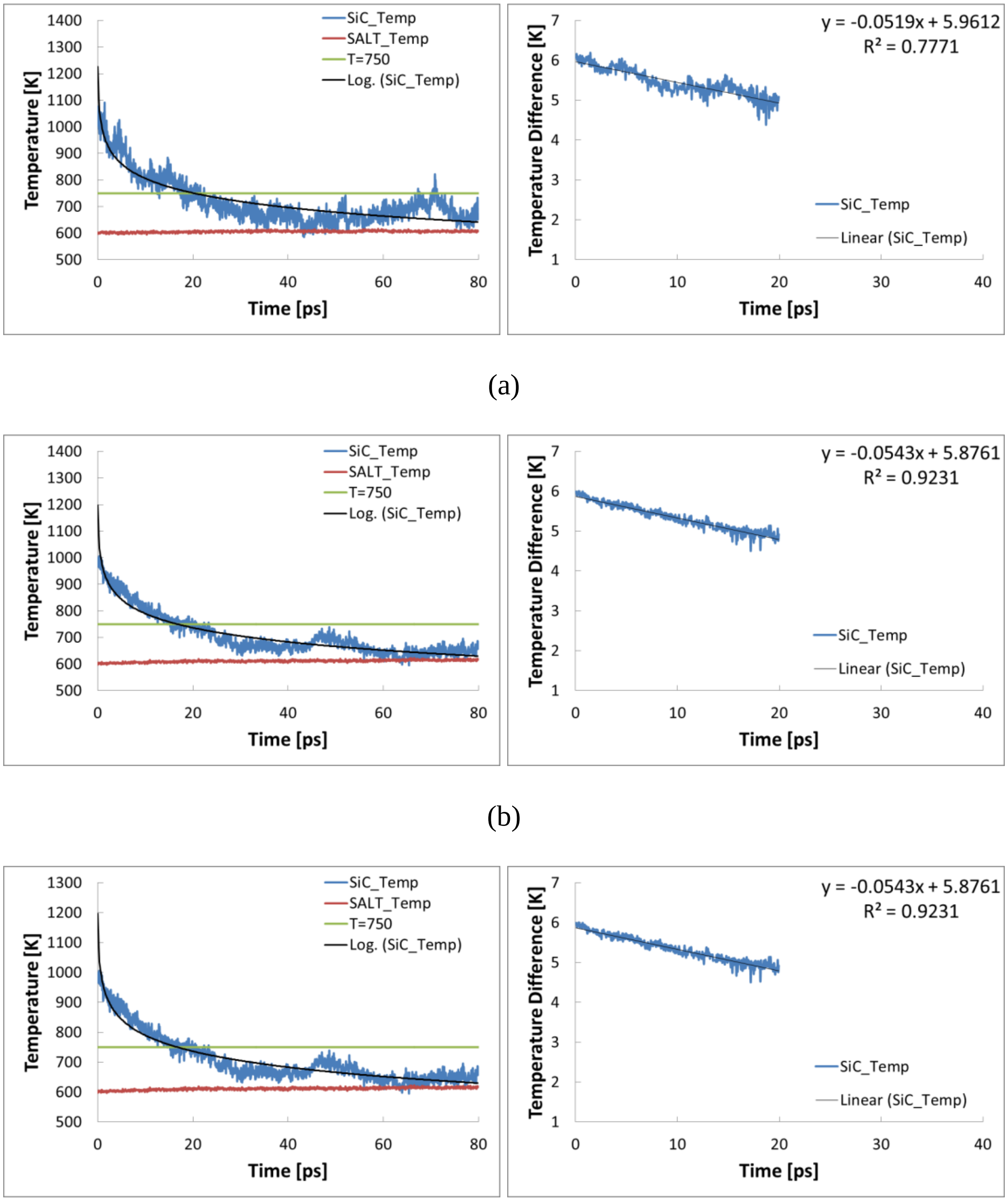

(a)

(b)

(c)

Fig. 7. Temporal variation of temperature: SiC/Nitrate salt mixture nanofluid (KNO_3:$NaNO_3$=60:40 in molar ratio) (a) radius of SiC nanoparticle = 5Å, (b) radius of SiC nanoparticle = 6Å, (c) radius of SiC nanoparticle = 7Å.

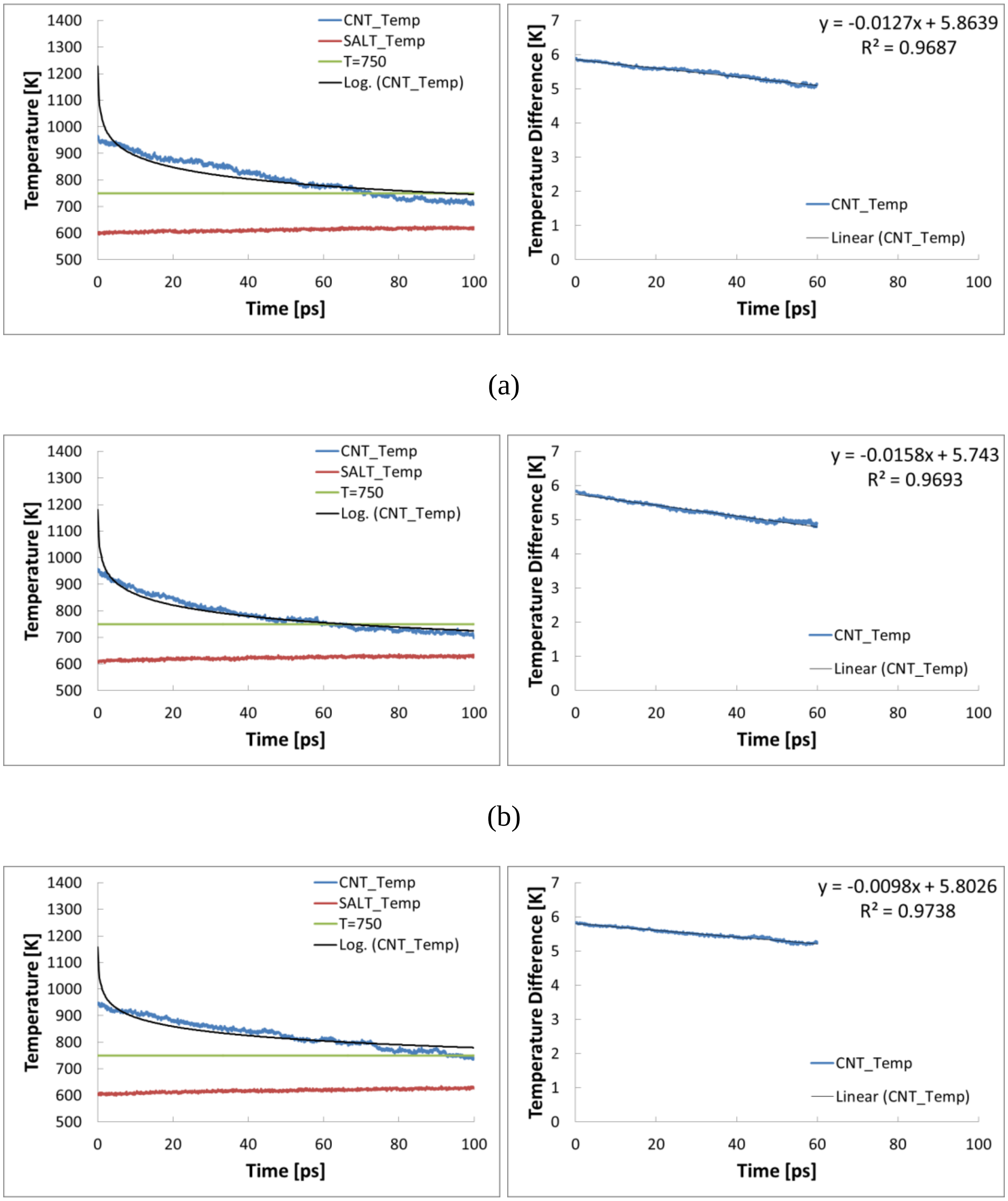

(a)

(b)

(c)

Fig. 8. Temporal variation of temperature: SWCNT/Nitrate salt mixture nanofluid (KNO_3:$NaNO_3$=60:40 in molar ratio) (a) (5, 5) armchair SWCNT, (b) (6, 6) armchair SWCNT, (c) (7, 7) armchair SWCNT.

Table 6. The relaxation time constant and the interfacial thermal resistance for nanofluid systems with different sizes of nanoparticles.

Nanoparticle	Size	slope	Time constant (ps)	Interfacial thermal resistance ($\times 10^{-8}$ m^2K/W)	d_c (nm)
Al_2O_3	5	0.2659	3.76	0.45	4.8
	6	0.1527	6.55	0.66	7.0
	7	0.0950	10.53	0.91	9.7
SiO_2	5	0.4112	2.43	0.46	6.5
	6	0.4386	2.28	0.36	5.1
	7	0.2898	3.45	0.47	6.6
SiC	5	0.0519	19.27	3.03	31.4
	6	0.0543	18.42	2.07	21.5
	7	0.0619	16.15	2.12	22.0
CNT	6.78	0.0127	78.74	14.06	145.3
	8.14	0.0158	63.29	11.30	116.8
	9.49	0.0098	102.04	18.22	188.2

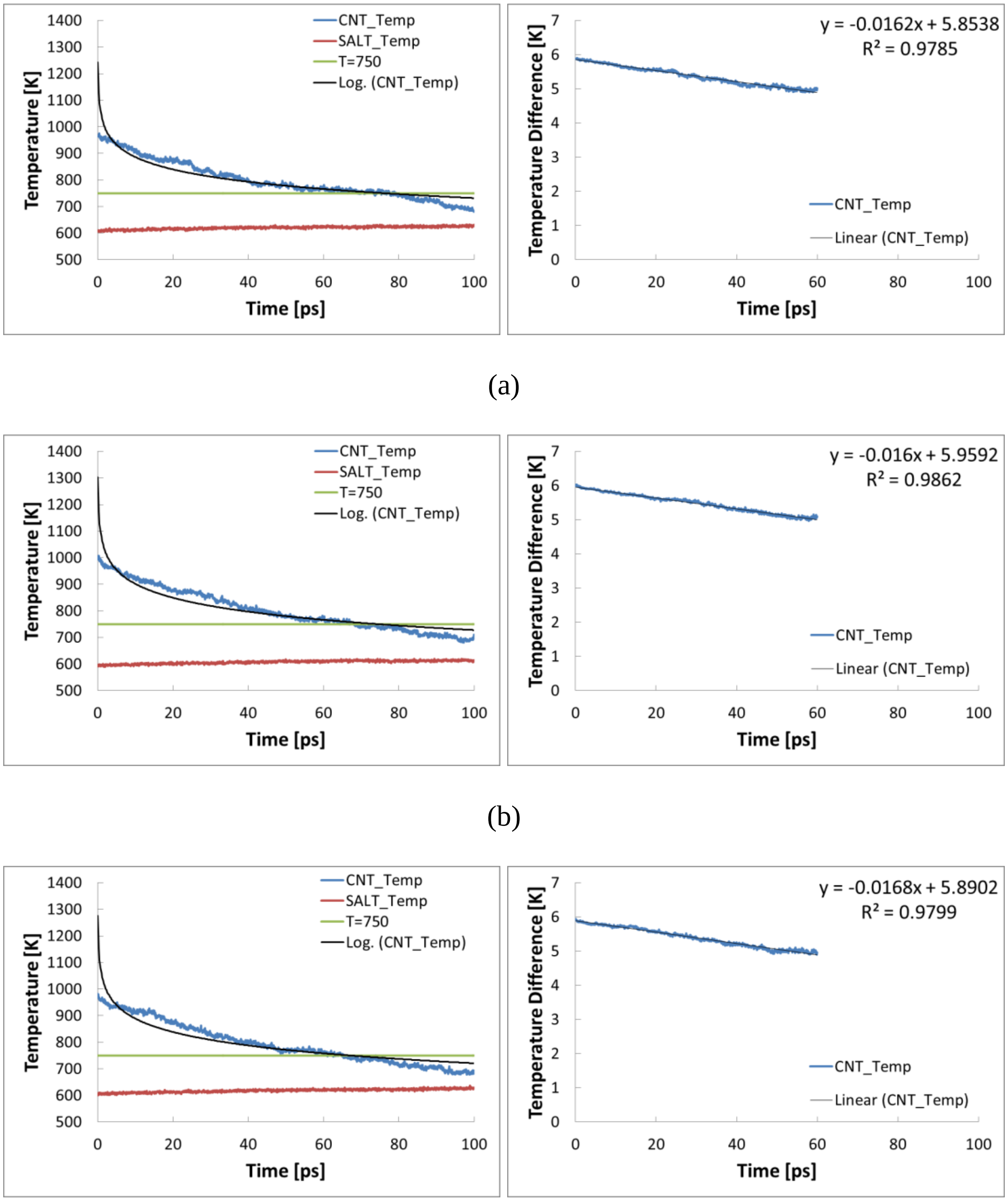

(a)

(b)

(c)

Fig. 9. Temporal variation of temperature: SWCNT/Nitrate salt mixture nanofluids (a) pure KNO_3, (b) pure $NaNO_3$, (c) KNO_3:$NaNO_3$=40:60 in molar ratio.

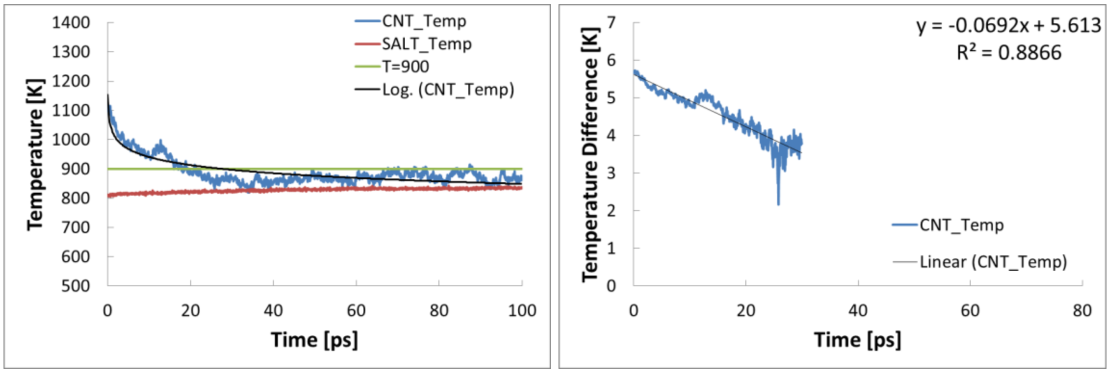

Fig. 10. Temporal variation of temperature: SWCNT/Carbonate salt mixture nanofluid (Li_2CO_3:K_2CO_3=62:38 in molar ratio).

Table 7. The relaxation time constant and the interfacial thermal resistance between SWCNT and molten alkali-nitrate salt mixture.

KNO_3:$NaNO_3$ in molar ratio	slope	Time Constant (ps)	Interfacial thermal resistance ($\times 10^{-8}$ m^2K/W)
100:0	0.0162	61.7	11.02
60:40	0.0127	78.7	14.06
40:60	0.0168	59.5	10.63
0:100	0.0160	62.5	11.16

Table 8. The relaxation time constant and the interfacial thermal resistance between SWCNT and molten alkali-carbonate salt mixture.

Li_2CO_3:K_2CO_3 in molar ratio	slope	Time Constant (ps)	Interfacial thermal resistance ($\times 10^{-8}$ m^2K/W)
62:38	0.0692	14.4	2.58

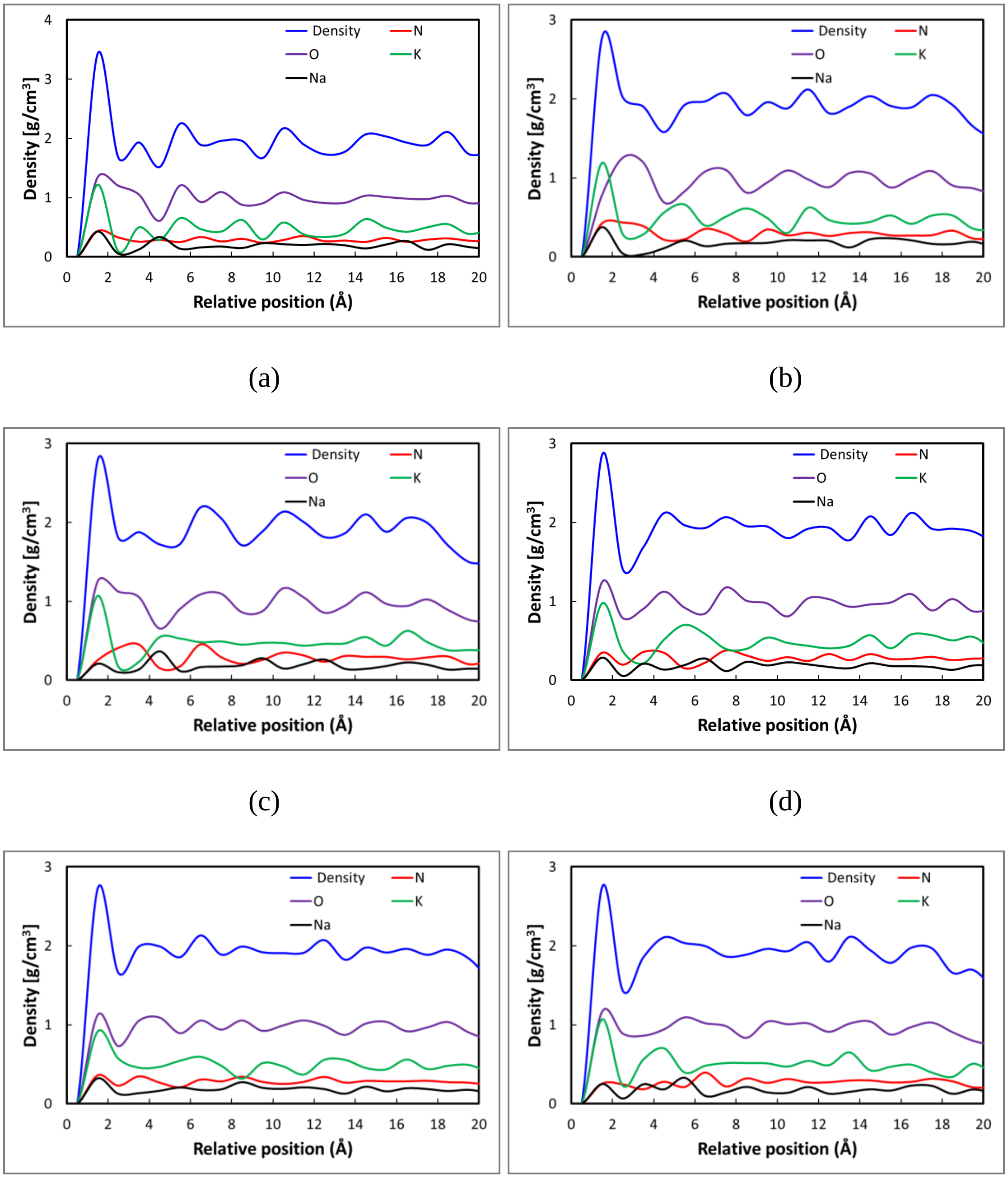

(a)

(b)

(c)

(d)

(e)

(f)

Fig. 11. Density plots and spatial distributions of atomic concentration of different elements of nitrate salt mixture nanofluids: (a) Al_2O_3 (5Å), (b) Al_2O_3 (6Å), (c) Al_2O_3 (7Å), (d) SiO_2 (5Å), (e) SiO_2 (6Å), (f) SiO_2 (7Å), (g) SiC (5Å), (h) SiC (6Å), (i) SiC (7Å), (j) (5, 5) armchair SWCNT, (k) (6, 6) armchair SWCNT, (l) (7, 7) armchair SWCNT.

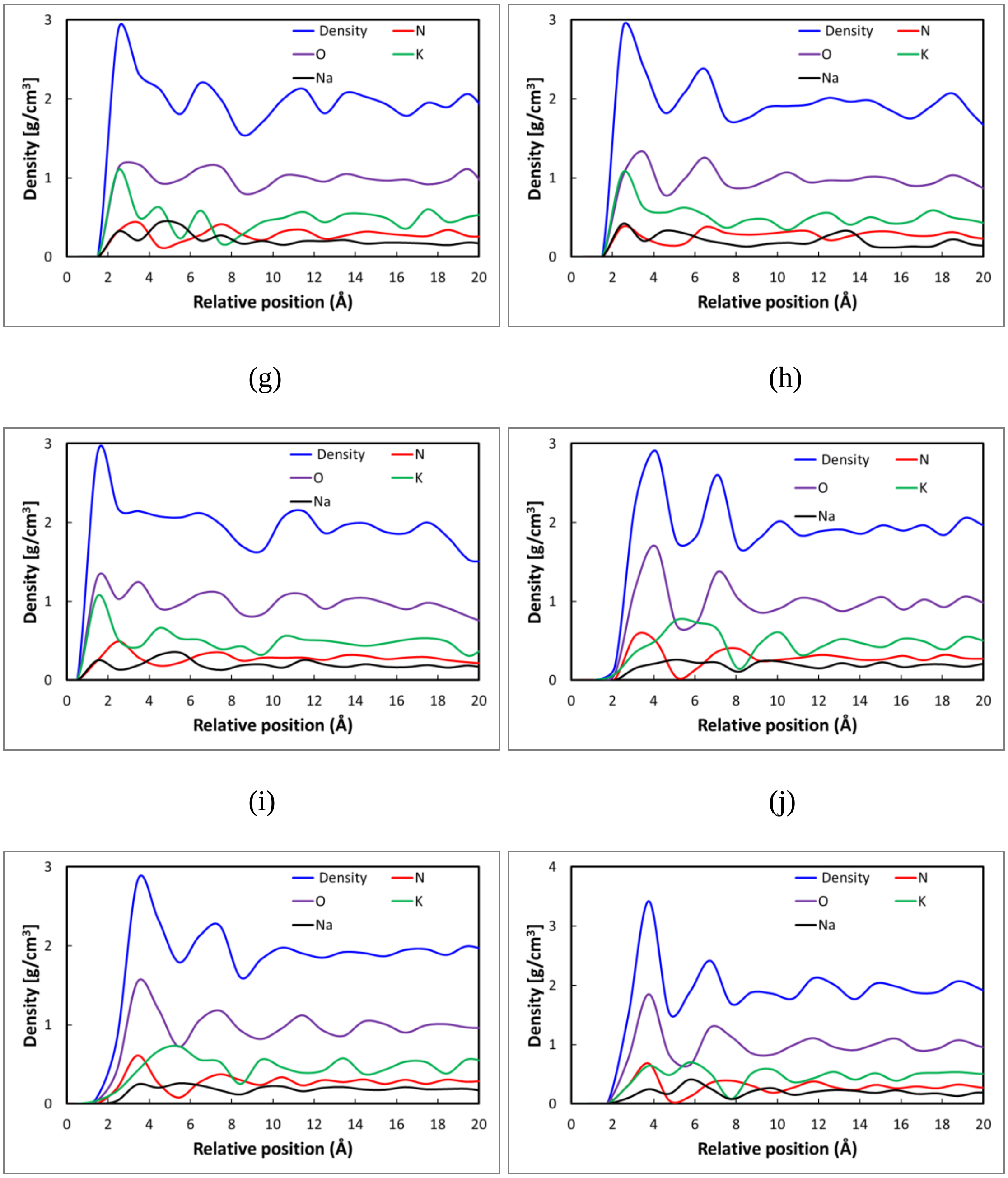

(g) (h)

(i) (j)

(k) (l)

Fig. 11. Continued

6. Summary and Conclusions

In this study, MD simulation was performed for calculating the interfacial thermal resistance of nanomaterials. The calculations were performed by varying the nanoparticle size, nanoparticle material, and composition of the solvent phase surrounding the nanoparticles. The results show that nitrate salt-based nanofluid systems with oxide nanoparticles have the lowest value for the interfacial thermal resistance, while that of the SWCNT is the highest. In addition, carbonate-based nanofluid with SWCNT has lower value compared to that of the nitrate-based nanofluid with SWCNT.

CHAPTER III

EXPERIMENTAL INVESTIGATION

A. Phase Diagram of Alkali Nitrate Salt

Nitrate salt mixtures are used as the base material (solvent) for synthesizing the molten salt nanomaterials. Nitrate salt is typically thermally stable up to 600℃. The nitrate salt mixture used in this study consists of potassium nitrate (KNO_3) and sodium nitrate ($NaNO_3$). The phase diagram of binary mixture of the nitrate salt was presented by Janz et al. (1979) [73]. The phase diagram indicates that it has a eutectic point where the molar ratio of the two salts is 54:46 (KNO_3:$NaNO_3$). In this study, the 60:40 eutectic is chosen as a base material for the initial mixture. The melting point is the eutectic (60:40 in molar ratio) is around 230℃.

B. Specific Heat Capacity of Nanomaterials: Mica and Nitrate Salt Mixture

The specific heat capacity of the alkali-nitrate salt-based nanomaterials (at low mass concentration of mica nanoparticles) was measured for both solid and liquid phase. The specific heat capacity of binary mixture of alkali-nitrate salt samples (KNO_3: $NaNO_3$ in 60:40 molar ratio) was measured and compared to that of the corresponding nanomaterial (that was obtained by mixing the binary salt mixture with mica nanoparticles). The specific heat capacity measurements were performed for a temperature range of 150℃-500℃. The melting point of the binary mixture of the nitrate salt for this composition is 230℃. The measurements were performed for different mass concentrations of mica nanoparticles, which ranged from 0.5% to 2%.

1. Synthesis Protocol, Experimental Apparatus and Measurement Procedure

The measurements were performed using a differential scanning calorimeter (DSC) (TA Instruments, Model: Q20). Potassium nitrate (KNO_3), sodium nitrate ($NaNO_3$), and mica nanoparticles were procured from Spectrum Inc. The nominal size of the mica nanoparticles was ~45μm (or 325mesh) by reported manufacturer's specification. However, the actual size of the nanoparticles was observed by transmission electron microscopy (TEM) images. The results indicate that the size of nanoparticles is from a few nano-meters (nm) to a few micro-meters (μm) as shown in Fig. 12.

The synthesis method for the nanomaterials is described next. Initially, potassium nitrate and sodium nitrate mixture (KNO_3:$NaNO_3$ = 60:40 in molar ratio) and mica nanoparticles were weighed in a measuring balance and deposited into a glass vial. The glass vial had a volume of 25ml volume. The total mass of the nitrate salt mixture containing the mica nanoparticles was 200mg. The vial was then filled with 20ml of distilled water (DI water). To ensure homogenous dispersion of the mica nanoparticles, the suspension was placed in an ultrasonication bath for 1.5 hours. The aqueous solution was then placed on a hot plate (set at 100℃) to evaporate the water from the solution. After the evaporation was completed, the nitrate salt mixture containing the mica nanoparticles was scraped off using a spatula and used for the DSC measurements. Fig.

13 shows the schematic for the synthesis method for the nitrate salt-based nanomaterial using mica nanoparticles.

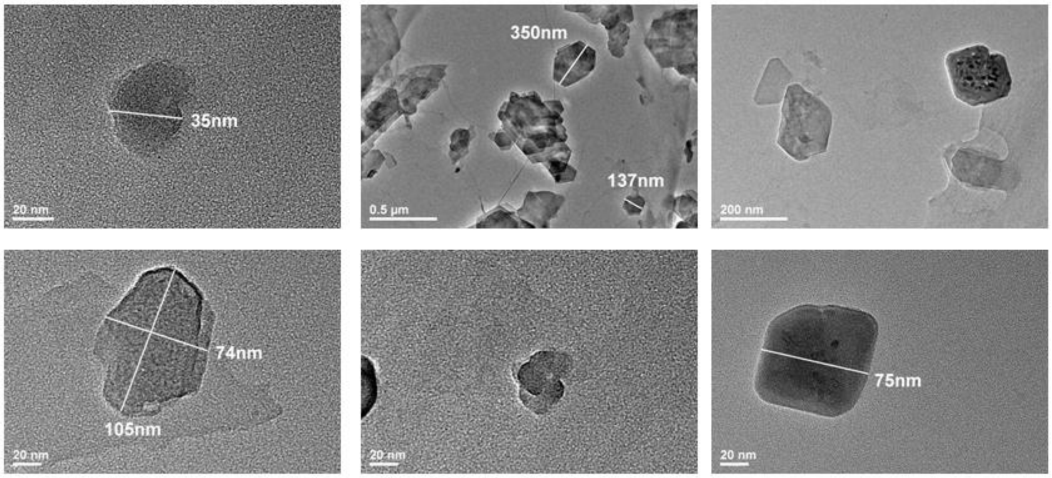

Fig. 12. TEM images of the mica nanoparticles used in this study [74].*

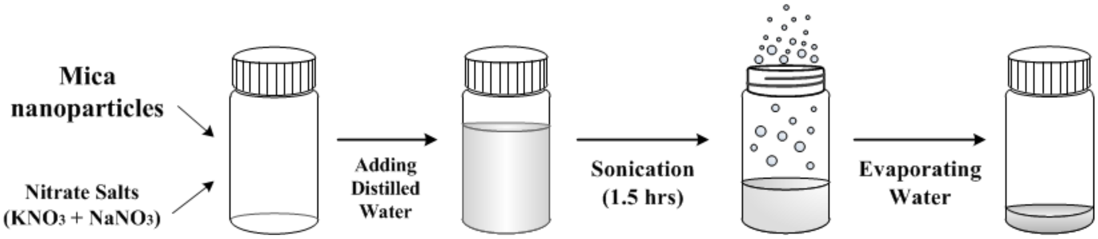

Fig. 13. Synthesis procedure for nitrate salt nanomaterials mixed with mica nanoparticles.

---

[*] Reprinted with permission from *Developments in Strategic Materials and Computational Design II: Ceramic Engineering and Science Proceedings, Volume 32*, by Jung, S. and Banerjee, D., 2011, John Wiley & Sons, Inc., Hoboken, NJ, USA.Copyright 2011 by John Wiley & Sons, Inc.

Using this synthesis method, nanomaterial samples were synthesized with the mass concentration of nanoparticles being 0.5%, 1%, and 2%. These nanomaterial samples were characterized using scanning electron microscopy (SEM). Pure nitrate salt mixture sample was characterized in Fig. 14 while the representative SEM images of nanomaterial samples are shown in Fig. 15. SEM images indicate that the mica nanoparticle was observed to be enveloped with nitrate salt. From energy dispersive X-ray spectroscopy (EDS) analysis, the existence of mica nanoparticle was identified as shown in Fig. 16. To measure the specific heat capacity of the samples of nanomaterials, a standard protocol for differential scanning calorimeter (DSC) testing (ASTM-E1269 [75]) was implemented. Standard T-zero hermetic pan and lid (from TA instruments, Inc.) were used to minimize any loss of the samples during repeated thermo-cycling. Prior to dispensing the samples into the hermetic pans, the samples were heated at 150℃ for 2 hours to eliminate any chemically adsorbed water molecules. Specific heat capacity values were measured using a differential scanning calorimeter (from TA Instrument, Model: Q20).

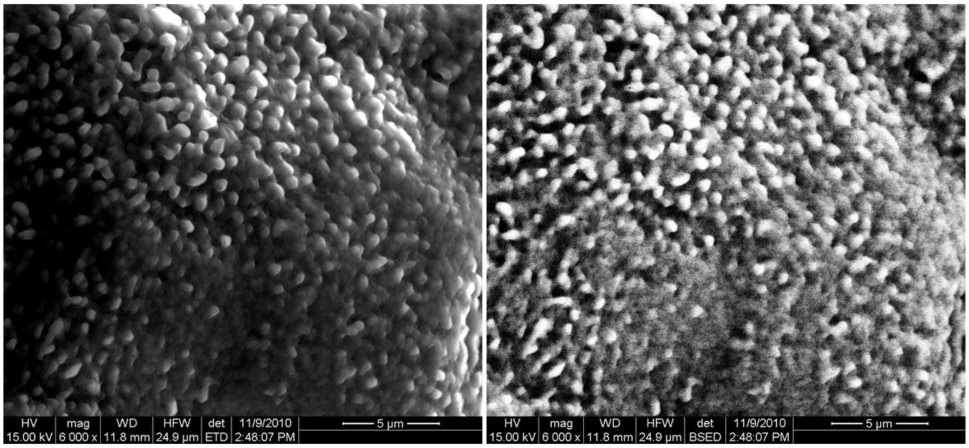

(a) (b)

Fig. 14. SEM images of the pure nitrate salt (KNO_3:$NaNO_3$ = 60:40 in molar ratio) mixture: (a) secondary electron image, (b) backscattered electron image.

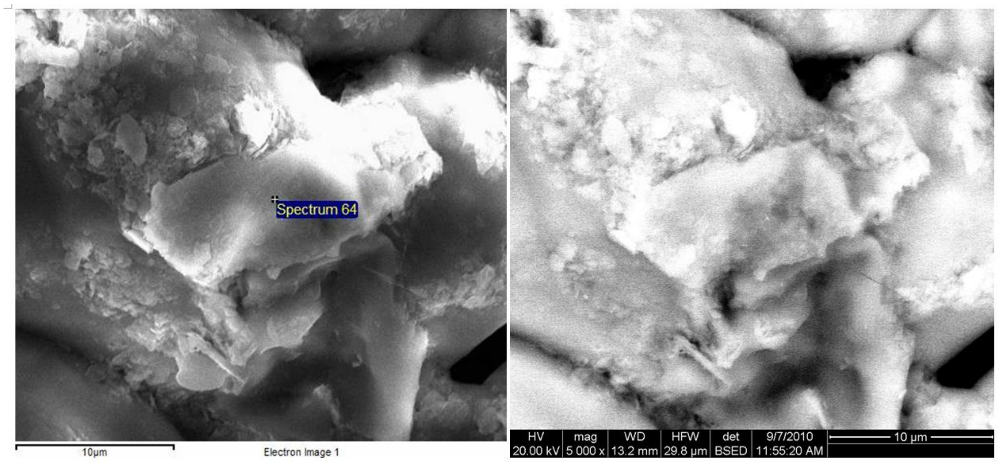

(a) (b)

Fig. 15. SEM images of the nitrate salt nanomaterials using mica nanoparticles with 2% mass concentration: (a) secondary electron image, (b) backscattered electron image [74].[*]

---

[*] Reprinted with permission from *Developments in Strategic Materials and Computational Design II: Ceramic Engineering and Science Proceedings, Volume 32*, by Jung, S. and Banerjee, D., 2011, John Wiley & Sons, Inc., Hoboken, NJ, USA.Copyright 2011 by John Wiley & Sons, Inc.

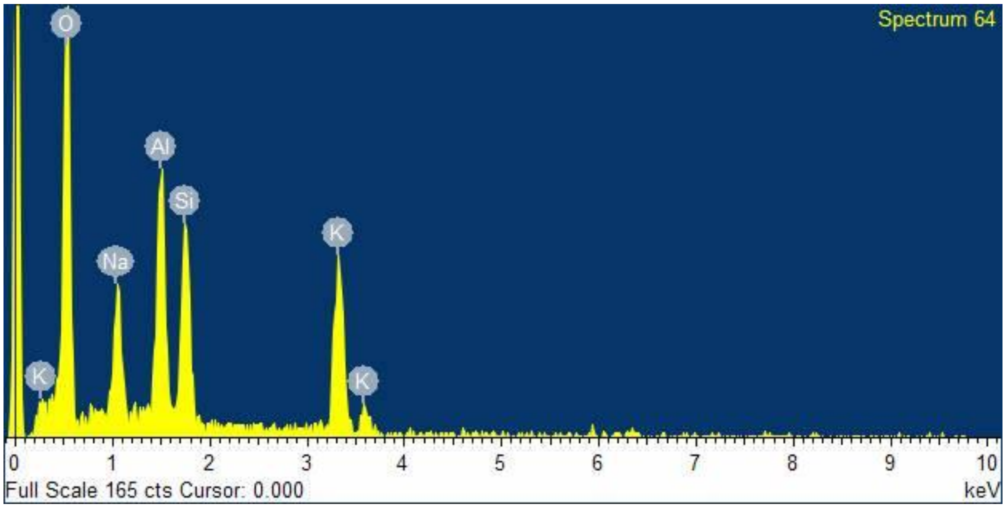

Fig. 16. EDS analysis from SEM [74].*

---

* Reprinted with permission from *Developments in Strategic Materials and Computational Design II: Ceramic Engineering and Science Proceedings, Volume 32*, by Jung, S. and Banerjee, D., 2011, John Wiley & Sons, Inc., Hoboken, NJ, USA.Copyright 2011 by John Wiley & Sons, Inc.

To calculate the specific heat capacity values by the ASTM method, measurements for the total “differential” amount of heat transfer were performed as the temperature of the sample was ramped at a set ramp rate. Initially measurements for the differential heat flow were performed using an empty pan and another reference pan (also empty). The measurements were then repeated by the same pan now containing a sapphire standard disc (in comparison to the empty reference pan). The sapphire standard was removed from the pan and the pan was then filled with the salt sample (pure salt sample or the nanomaterial sample). The pan was hermetically sealed. The ratio of the differential heat flow for empty pan to that of the pan containing the sapphire standard was used to calibrate the measurements, (since sapphire has a specific heat capacity of 1J/g-K, which is fairly independent of temperature). After the calibration step (performed for every sample and for every measurement) the specific heat capacity of the sample was determined from the ratio of the differential heat flow for empty pan to that of the hermetically sealed pan containing the sample (and also after accounting for the mass ratios of the sapphire to that of the samples). A ramp rate of 20℃/min was used for the thermo-cycling experiments. In each measurement experiment - the thermo-cycles (melting and resolidification) were repeated 5 times for each sample in order to verify the repeatability of the measurements. The thermo-cycles were repeated to verify if the nanoparticles were stable in the nitrate salt mixture.

2. Measurement Uncertainty

The specific heat capacity value of nanomaterials was determined by ASTM method by the following equation [76]:

$$c_s = c_{st} \frac{\Delta q_s \cdot m_{st}}{\Delta q_{st} \cdot m_s} \tag{III-1}$$

where c is the specific heat capacity, Δq is the differential heat flow measurement between the sample pan (containing a sapphire standard disc or pure salt sample or the nanomaterial sample) and the reference pan (empty T-zero pan that was hermetically sealed), m is the mass. Subscript, s, indicates samples of nanomaterials, and subscript, st, indicates the standard materials which is sapphire in this study. The heat flow differences were obtained by subtracting baseline (empty pan, subscript b) heat flow from the heat flows of the sapphire (subscript st) and the sample (subscript s). The measurement uncertainty can be expressed as [76]:

$$\frac{U_{c_s}}{c_s} = \sqrt{\left(\frac{U\left(c_{st}\right)}{c_{st}}\right)^2 + \left(\frac{U\left(\Delta q_b\right)}{\delta\left(q_b\right)}\right)^2 + \left(\frac{U\left(\Delta q_s\right)}{\delta\left(q_s\right)}\right)^2 + \left(\frac{U\left(\Delta q_{st}\right)}{\delta\left(q_{st}\right)}\right)^2 + \left(\frac{U\left(m_s\right)}{m_s}\right)^2 + \left(\frac{U\left(m_{st}\right)}{m_{st}}\right)^2} \tag{III-2}$$

Uncertainty values arise from the curve fitting of specific heat capacity of sapphire, the heat flow of the sample and the sapphire, and the mass of the samples of nanomaterials and the sapphire. The uncertainties for the curve fitted specific heat capacity of the sapphire and heat flow are ±0.3% and ±2%, respectively. The maximum uncertainty in the measurement of the specific heat capacity is estimated to be ±3.5%.

3. Results and Discussions

The measurements for the specific heat capacity of the nitrate salt nanomaterials were implemented for samples containing mica nanoparticles at mass concentration of 0.5%, 1%, and 2%. Specific heat capacity values of the pure nitrate salt mixture (KNO_3:$NaNO_3$ = 60:40 in molar ratio) were measured to compare with those of the corresponding nanomaterials. Table 9 lists the results from the measurement of the specific heat capacity of pure nitrate salt mixture. The measurement temperature range is 150℃ - 500℃. The specific heat capacity value listed in the table for the solid phase is the average value for the temperature range of 160℃ – 200℃. Also the specific heat capacity value listed in the table for the liquid phase is the average value for the temperature range of 250℃ – 495℃.

The average value of the specific heat capacity of the samples of pure mixture of nitrate salt was measured to be 1.191J/g-K in the solid phase with a standard deviation of 0.0746J/g-K (6.26%) and 1.315J/g-K in the liquid phase with a standard deviation of 0.099J/g-K (6.13%). The average values for specific heat capacity obtained from each thermo-cycle experiment in the DSC measurements for the nanomaterial samples are shown in Table 10, Table 11, and Table 12. The thermo-cycle data for each nanomaterial sample are ploted as a function of temperature as shown in Fig. 17, Fig. 18, and Fig. 19. These results are also plotted in Fig. 20.

Table 9. Specific heat capacity of pure samples of nitrate salt mixtures (KNO_3:$NaNO_3$ = 60:40 in molar ratio) [74].*

Sample No.	Specific Heat (J/g-K) in solid phase	Specific Heat (J/g-K) in liquid phase
1	1.251	1.408
2	1.098	1.255
3	1.211	1.258
4	1.297	1.471
5	1.153	1.254
6	1.141	1.244
Average	1.191	1.315
STD	0.0746	0.099

---

* Reprinted with permission from *Developments in Strategic Materials and Computational Design II: Ceramic Engineering and Science Proceedings, Volume 32*, by Jung, S. and Banerjee, D., 2011, John Wiley & Sons, Inc., Hoboken, NJ, USA.Copyright 2011 by John Wiley & Sons, Inc.

Table 10. Specific heat capacity of nanomaterials obtained by dispersing mica nanoparticles at a mass concentration of 0.5% into a pure mixture of alkali-nitrate salt [74].*

Thermo-cycle	Specific Heat (J/g-K) in solid phase	Specific Heat (J/g-K) in liquid phase
1st run	1.384	1.527
2nd run	1.358	1.477
3rd run	1.362	1.477
4th run	1.370	1.479
5th run	1.375	1.483
Average	1.370	1.488
Enhancement	15%	13.2%
STD	0.010	0.021

---

[*] Reprinted with permission from *Developments in Strategic Materials and Computational Design II: Ceramic Engineering and Science Proceedings, Volume 32*, by Jung, S. and Banerjee, D., 2011, John Wiley & Sons, Inc., Hoboken, NJ, USA.Copyright 2011 by John Wiley & Sons, Inc.

Table 11. Specific heat capacity of nanomaterials obtained by dispersing mica nanoparticles at a mass concentration of 1% into a pure mixture of alkali-nitrate salt [74].*

Thermo-cycle	Specific Heat (J/g-K) in solid phase	Specific Heat (J/g-K) in liquid phase
1st run	1.385	1.576
2nd run	1.326	1.502
3rd run	1.324	1.495
4th run	1.318	1.484
5th run	1.314	1.482
Average	1.333	1.508
Enhancement	11.9%	14.7%
STD	0.029	0.039

---

[*] Reprinted with permission from *Developments in Strategic Materials and Computational Design II: Ceramic Engineering and Science Proceedings, Volume 32*, by Jung, S. and Banerjee, D., 2011, John Wiley & Sons, Inc., Hoboken, NJ, USA.Copyright 2011 by John Wiley & Sons, Inc.

Table 12. Specific heat capacity of nanomaterials obtained by dispersing mica nanoparticles at a mass concentration of 2% into a pure mixture of alkali-nitrate salt [74].*

Thermo-cycle	Specific Heat (J/g-K) in solid phase	Specific Heat (J/g-K) in liquid phase
1st run	1.347	1.556
2nd run	1.342	1.559
3rd run	1.341	1.562
4th run	1.340	1.557
5th run	1.338	1.562
Average	1.342	1.559
Enhancement	12.7%	18.6%
STD	0.003	0.003

---

* Reprinted with permission from *Developments in Strategic Materials and Computational Design II: Ceramic Engineering and Science Proceedings, Volume 32*, by Jung, S. and Banerjee, D., 2011, John Wiley & Sons, Inc., Hoboken, NJ, USA.Copyright 2011 by John Wiley & Sons, Inc.

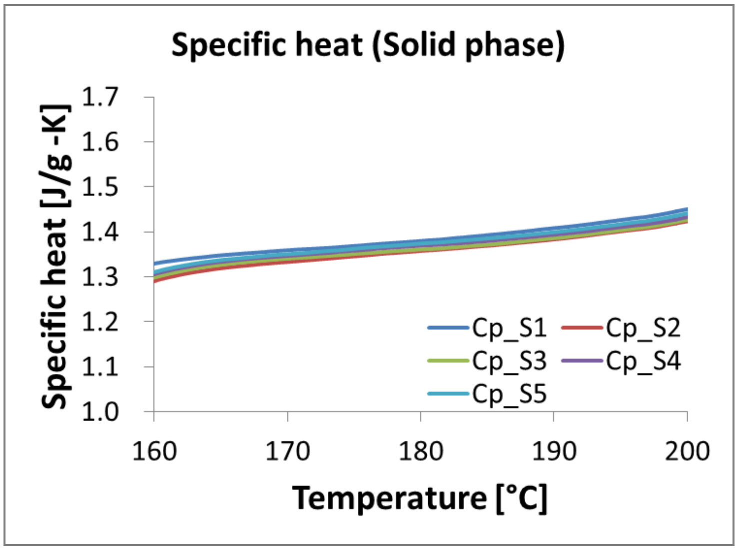

(a)

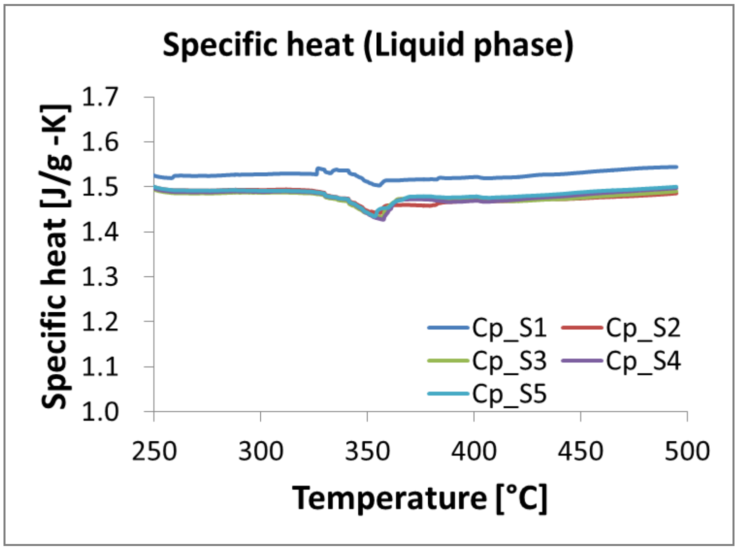

(b)

Fig. 17. Specific heat capacity values plotted as a function of temperature for each thermo-cycle. The samples alkali-nitrate salt-based nanomaterials with 0.5% mass concentration of mica nanoparticles. The measured property data were categorized into (a) solid phase, and (b) liquid phase.

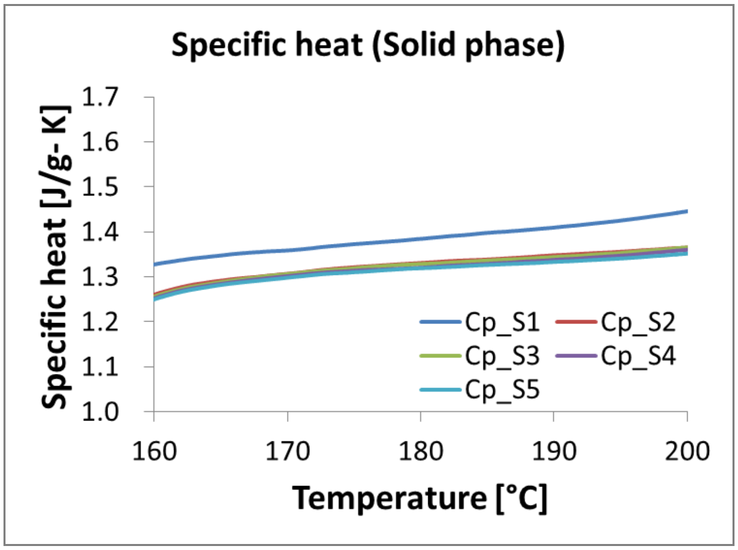

(a)

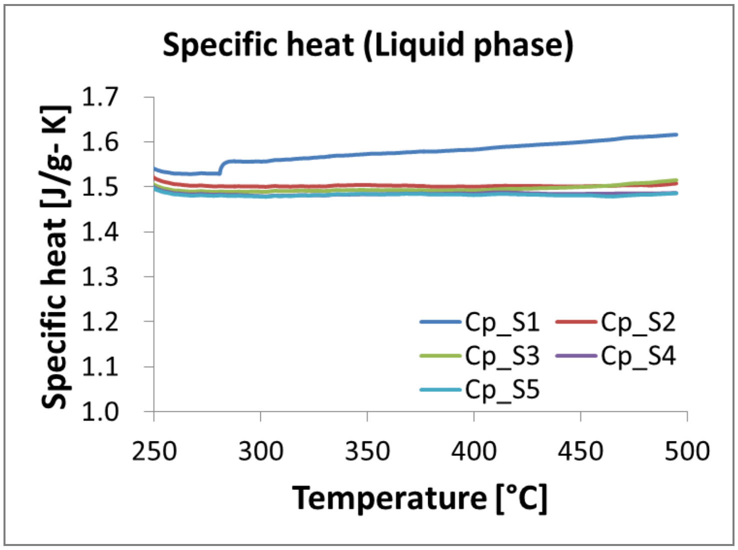

(b)

Fig. 18. Specific heat capacity values plotted as a function of temperature for each thermo-cycle. The samples alkali-nitrate salt-based nanomaterials with 1% mass concentration of mica nanoparticles. The measured property data were categorized into (a) solid phase, and (b) liquid phase.

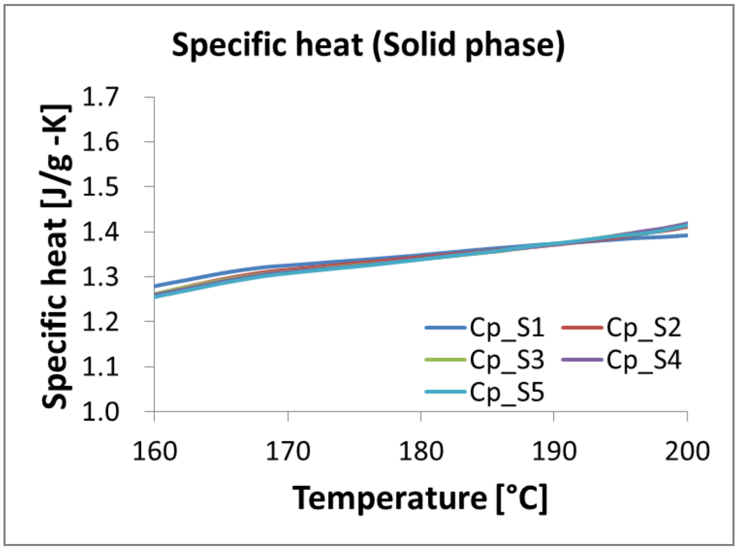

(a)

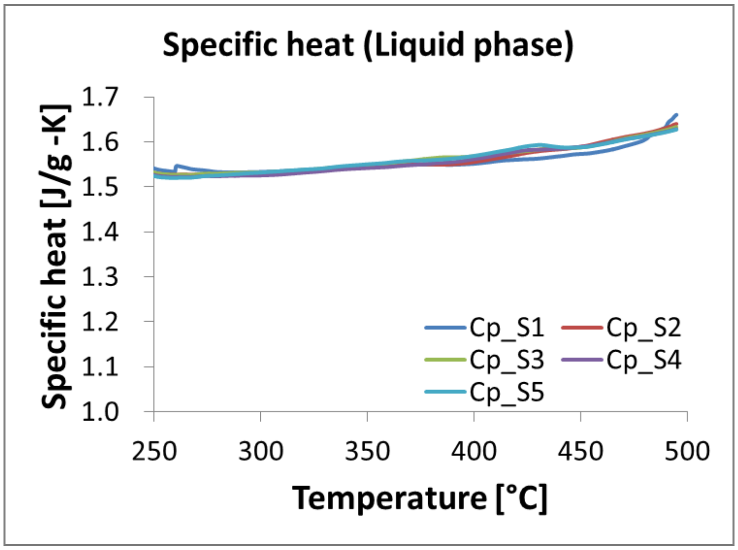

(b)

Fig. 19. Specific heat capacity values plotted as a function of temperature for each thermo-cycle. The samples alkali-nitrate salt-based nanomaterials with 2% mass concentration of mica nanoparticles. The measured property data were categorized into (a) solid phase, and (b) liquid phase.

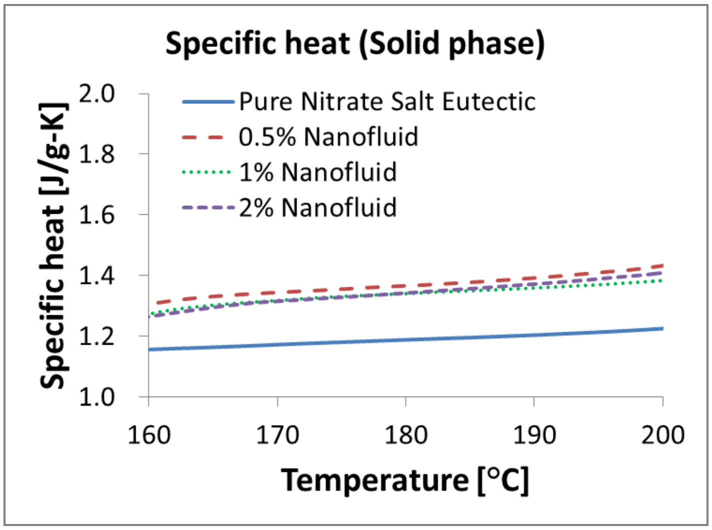

(a)

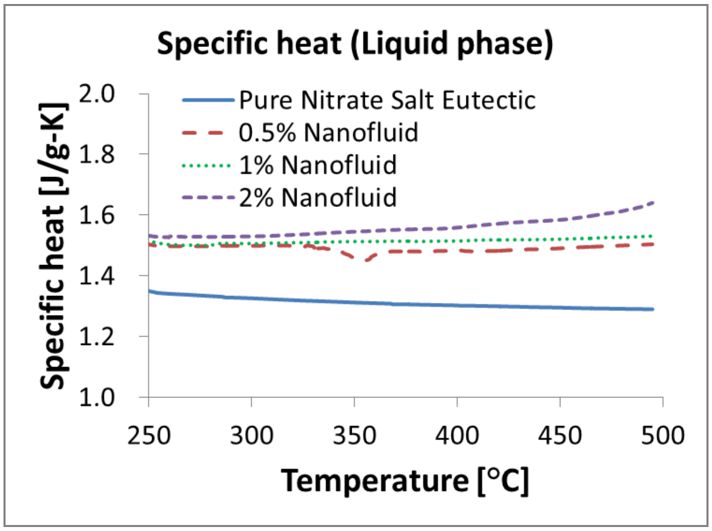

(b)

Fig. 20. Specific heat capacity values plotted as a function of temperature for various samples. The samples are pure mixture of alkali-nitrate salt and the corresponding nanomaterials that were synthesized by dispersing mica nanoparticles in a mixture of alkali nitrate salt. The measured property data were categorized into (a) solid phase, and (b) liquid phase [74].*

---

* Reprinted with permission from *Developments in Strategic Materials and Computational Design II: Ceramic Engineering and Science Proceedings, Volume 32*, by Jung, S. and Banerjee, D., 2011, John Wiley & Sons, Inc., Hoboken, NJ, USA.Copyright 2011 by John Wiley & Sons, Inc.

The results indicate that the specific heat capacity values of the nanomaterials were enhanced by 13-15% in the solid phase and 13-19% in the liquid phase (compared to that of the corresponding pure salt mixtures). In liquid phase, the specific heat capacity values were found to increase consistently with the mass concentration of the mica nanoparticles. In contrast, the corresponding enhancements in the property values in the solid phase were relatively insensitive to the mass concentration of the mica nanoparticles.

The mechanism of specific heat capacity enhancement in nitrate salt-based nanomaterials with mica nanoparticles can be explained by considering two different perspectives regarding the material properties of the constituents. First of all, specific heat capacity values of pure mica nanoparticles are higher than pure nitrate salt mixture for overall temperature range of 150℃-500℃. Fig. 21 shows the results of specific heat capacity of pure nitrate salt mixture and pure mica nanoparticles in solid and liquid phase. The specific heat capacity values of mica nanoparticles are ~10% and ~10% - 100% higher than that of the pure sample of the nitrate salt mixture, in the solid and liquid phase of the salt, respectively (mica nanoparticle samples are solid for the whole temperature range).

Another mechanism of specific heat capacity enhancement is the formation of the compressed phase by the solvent molecules at the solid-liquid interface between the nanoparticle and the solvent (as discussed before in Chapter II). The existence of the compressed phase was indirectly identified in this study.

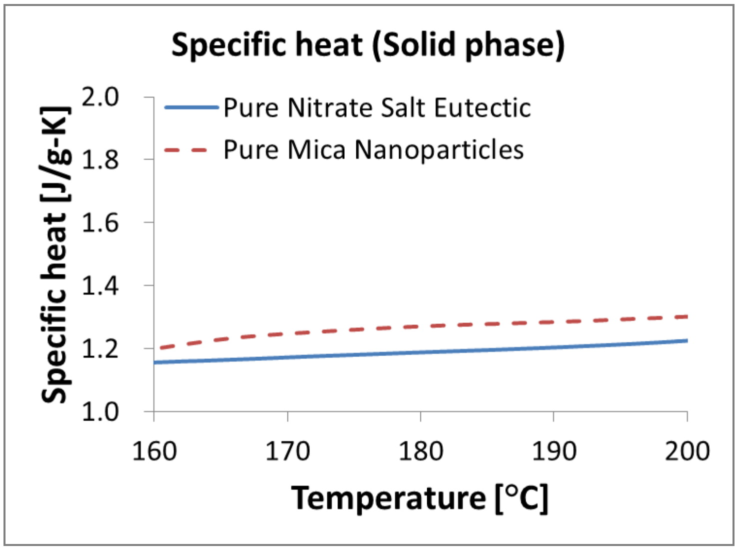

(a)

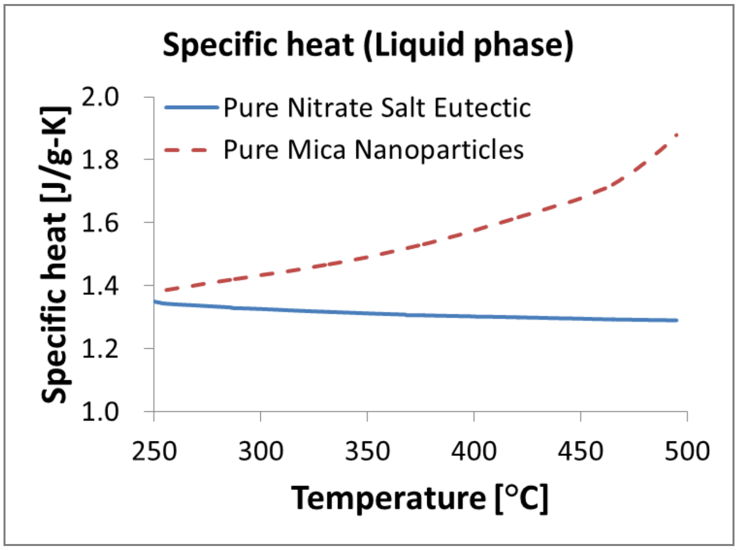

(b)

Fig. 21. Specific heat capacity values of pure nitrate salt mixture and pure mica nanoparticles: (a) in solid phase, (b) in liquid phase [74].*

---

* Reprinted with permission from *Developments in Strategic Materials and Computational Design II: Ceramic Engineering and Science Proceedings, Volume 32*, by Jung, S. and Banerjee, D., 2011, John Wiley & Sons, Inc., Hoboken, NJ, USA.Copyright 2011 by John Wiley & Sons, Inc.

The results from this study show that it is possible that the compressed phase is formed by molecular reorganization and it also exists in the solid phase of the nanocomposite. These conclusions were reached from the measurements of the specific heat capacity of nitrate salt nanomaterials in solid phase for samples that were subjected to phase change (melting followed by resolidification) and compared to that of samples which did not undergo melting in the thermo-cycling studies (the range of measurement temperatures were restricted to below the melting point after the synthesis of the nanomaterials). For the samples subjected to phase change, the specific heat capacity was measured for a temperature range of 150℃-500℃. As mentioned before - the melting point of nitrate salt mixture is ~230℃. Thus, phase change is obtained by repeated thermo-cycling.

For samples restricted from undergoing phase change, the specific heat capacity was measured for a temperature range of 150℃-200℃. Hence, the temperature range of measurement was below the melting point for these samples. The nanomaterials samples were synthesized by mixing the components (alkali-nitrate salt mixture and nanoparticles) in an aqueous solution, followed by ultrasonication and rapid evaporation of the water to obtain the dry powders of the desired nanomaterials with uniformly dispersed nanoparticles. Fig. 22 shows the results for the specific heat capacity values in solid phase for both types of samples. The results show that the specific heat capacity values of nanomaterials with phase change are enhanced by ~15% at a mass concentration of 0.5% and by ~10% for mass concentrations of 1% and 2% (compared to that of the samples not subjected to phase change).

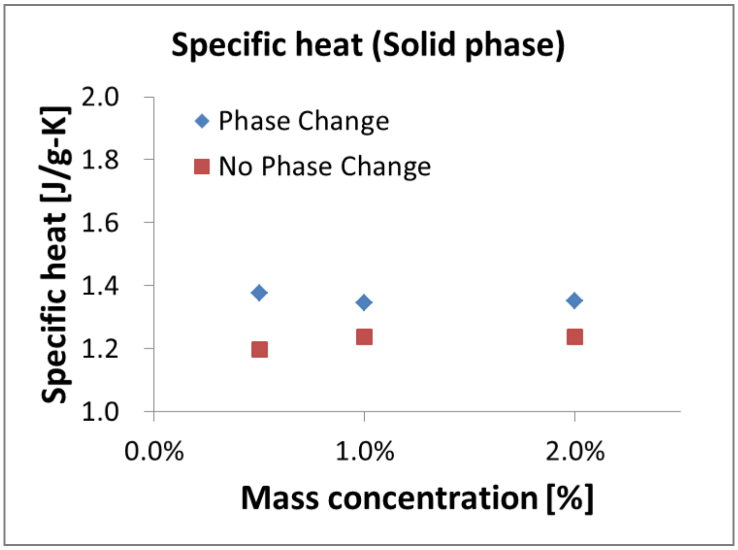

Fig. 22. Average specific heat capacity values of nanomaterials in the solid phase as a function of the mass concentration of the mica nanoparticles. While performing the thermo-cycling experiments - one set of samples was subjected to phase change (followed by re-solidification) while the temperature range for the other sample was restricted to below the melting point (hence the nanomaterial samples did not undergo phase change) [74].*

Based on these mechanisms, a simple analytical model for estimating specific heat capacity values of nanomaterials was developed and discussed in Chapter II. The same model was used to predict the property values of the nanomaterials in the experimental study. Table 13 lists the material property values (specific heat capacity and density) and the intermolecular interactions (thickness of compressed phase and void layer) for the component materials (mica, nitrate salt) that were used for calculating the resultant (or effective) specific heat capacity of the nanomaterials for liquid phase.

---

* Reprinted with permission from *Developments in Strategic Materials and Computational Design II: Ceramic Engineering and Science Proceedings, Volume 32*, by Jung, S. and Banerjee, D., 2011, John Wiley & Sons, Inc., Hoboken, NJ, USA.Copyright 2011 by John Wiley & Sons, Inc.

Table 14 lists the material property values and the intermolecular interactions for calculating the resultant (or effective) specific heat capacity for solid phase.

Table 13. List of material property values and molecular-interactions for pure nitrate salt mixture, the compressed phase, and the mica nanoparticles (for liquid phase) [74].*

Nanomaterial	ρ_n (kg/m^3)	ρ_s (kg/m^3)	C_n (J/g-K)	C_s (J/g-K)	C_l (J/g-K)	d_{sl} (nm)	δ (nm)
Mica/Nitrate	986	2770.5	1.55	131.5	1.315	0.3	1

Table 14. List of material property values and molecular-interactions for pure nitrate salt mixture, the compressed phase, and the mica nanoparticles (for solid phase).

Nanomaterial	ρ_n (kg/m^3)	ρ_s (kg/m^3)	C_n (J/g-K)	C_s (J/g-K)	C_l (J/g-K)	d_{sl} (nm)	δ (nm)
Mica/Nitrate	986	1800	1.26	118.9	1.189	0.3	1

The molecules in the compressed phase surrounding the nanoparticle surface are reported to behave like a solid phase [39-40]. Currently there is no available experimental or numerical data for estimating the thermo-physical properties of the compressed phase. In this study, density of compressed phase is assumed to be enhanced by 50% compared to pure nitrate salt mixture in liquid phase (based on the results from the MD simulations in Chapter II). The specific heat capacity of compressed phase is assumed to be 100 times the specific heat capacity of the pure nitrate salt mixture. In a

---

[*] Reprinted with permission from *Developments in Strategic Materials and Computational Design II: Ceramic Engineering and Science Proceedings, Volume 32*, by Jung, S. and Banerjee, D., 2011, John Wiley & Sons, Inc., Hoboken, NJ, USA.Copyright 2011 by John Wiley & Sons, Inc.

number of molecular dynamics (MD) simulations [14, 40, 48, 51], the liquid molecules were found to represent a disordered structure observed in the liquid phase at a distance greater than ~1nm from the nanoparticle surface. Based on the results, the thickness of the compressed phase was assumed to be 1nm. The void layer between the nanoparticle surface and the molecules in the solvent phase is estimated to be 0.3nm (based on the results from the MD simulations [14, 40, 48, 51]). The nominal size of the nanoparticles is assumed to be 100nm. The results from the predictions of the analytical model are compared with that of the experiments, as shown in Fig. 23.

The results from the simple analytical model for the specific heat capacity values of nitrate salt nanomaterials containing mica nanoparticles are found to be in close agreement with the experimental results at a mass concentration of 0.5% and 1%. In the case of nanomaterial with 2.0% mass concentration, predicted values are much higher than that of the experimental result. Based on the analytical model, it is apparent that the specific heat capacity values of nanomaterial samples containing well-dispersed nanoparticles will be much higher than that of a sample with agglomerated nanoparticles. It is possible that at higher mass concentrations the interactions between the nanoparticles caused rapid agglomeration and thus lower values of the specific heat capacity (than the values expected from the analytical predictions). Thus, the synthesis method needs to be refined so that better dispersion of the nanoparticles is obtained at higher mass concentrations.

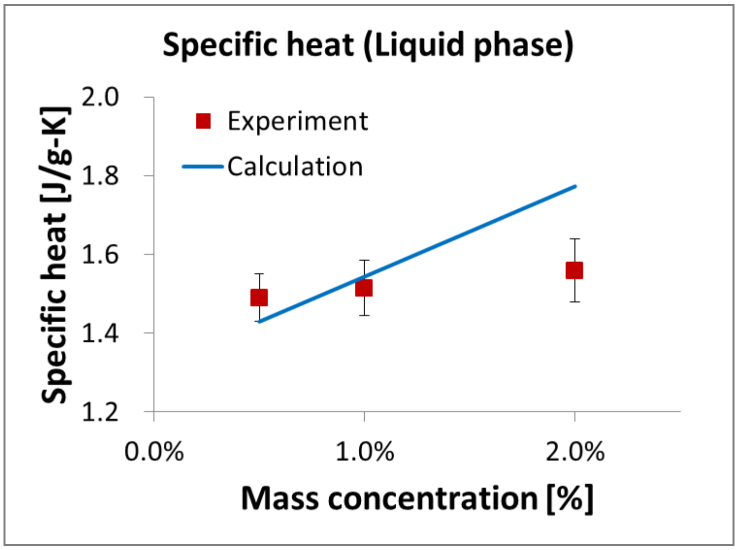

(a)

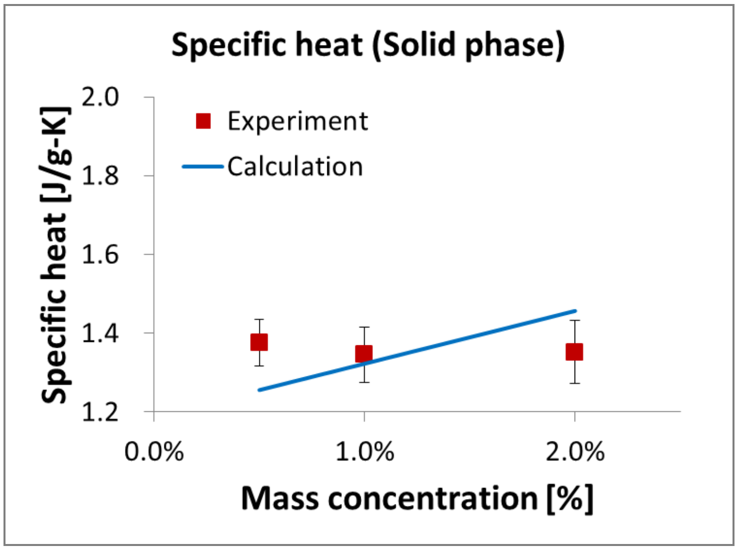

(b)

Fig. 23. Calculation results of specific heat capacity values and the experimental results (a) liquid phase (b) solid phase.

4. Summary and Conclusions

Experimental results show that the specific heat capacity values of nitrate salt mixtures (KNO_3:$NaNO_3$ = 60:40 in molar ratio) are enhanced on mixing with mica nanoparticles. The level of enhancement is 13-15% in the solid phase and 13-19% in the liquid phase. The enhancement in the specific heat capacity values in the liquid phase increases with the increase of mass concentration. However, the specific heat capacity values in the solid phase were found to be insensitive to the variation in mass concentration for mass concentrations of 0.5%, 1% and 2%. The dominant reason for the specific heat capacity enhancement in the liquid phase is assumed to be due to the formation of a "compressed phase" of the solvent molecules at the solid-liquid interface on the nanoparticle surface. The experiments showed that the specific heat capacity values in solid phase of the samples subjected to repeated phase change (and re-solidification) are significantly higher than that of the samples without phase change. Furthermore, the specific heat capacity of the mica nanoparticles is higher than that of the pure nitrate salt mixture, for the temperature range of 150℃ – 500℃.

Based on these observations, the analytical model proposed in Chapter II was used to predict the specific heat capacity values of the nanomaterial samples. The predictions were consistent with the experimental data at lower mass concentrations (i.e., 0.5% and 1%) – while the predictions deviated significantly from the experimental data at a mass concentration of 2%. This is possibly due to higher levels of agglomeration of the nanoparticles at higher mass concentration leading to reduction in the specific surface area (surface area per unit volume) of the agglomerated nanoparticles. The analytical model predicts that nanomaterial samples with well-dispersed nanoparticles can enable higher levels of enhancement of the specific heat capacity values compared to that of samples with significant amount of agglomerated nanoparticles.

To reiterate, the specific heat capacity of the nanocomposites (nanomaterials in the solid phase) was found to be enhanced by as much as 13-15% on addition of the mica nanoparticles. Furthermore, the specific heat capacity values of the nanofluids (nanomaterials in the liquid phase) were observed to be enhanced by 13-19%. These results are especially significant from a commercial viewpoint – since it was discussed previously that such levels of enhancement can result in cost of the solar thermal power to be reduced by as much as 20%. TES costs dominate the cost-benefit formulations for the total cost of solar thermal power. Hence, application of these mica nanoparticles to nitrate salt can be quite effective in reducing the cost of solar thermal power since nitrate salt is typically used as conventional materials for solar thermal energy storage.

C. Specific Heat Capacity of Nanomaterials: Alumina (Al_2O_3) and Nitrate Salt Mixture

The specific heat capacity of nitrate salt mixture (KNO_3: $NaNO_3$ in 60:40 molar ratio) was measured after mixing with alumina (Al_2O_3) nanoparticles at a mass concentration of 1%. The measurements were performed using a differential scanning calorimeter (DSC). The specific heat capacity measurements were performed for a temperature range of 150℃–500℃. As mentioned before, the melting point of the nitrate salt mixture is 230℃. Hence, the specific heat capacity of the nanomaterials and the pure nitrate salt mixture was measured in both the solid phase and the liquid phase. The measurements of the specific heat capacity values were conducted for two different samples of nanomaterials. In one of the samples, the nanoparticles were well dispersed and in the other sample the nanoparticles were agglomerated.

The solid phase specific heat capacity of nanomaterials (with well dispersed nanoparticles) was found to be enhanced by as much as ~11% on addition of alumina (Al_2O_3) nanoparticles. Furthermore, the liquid phase specific heat capacity values were observed to be enhanced by ~19%. For nanomaterial samples with agglomerated nanoparticles, no significant enhancement in the specific heat capacity values was observed in the experimental data.

Based on the analytical model for prediction of specific heat capacity values of nanofluids (as discussed in Chapter II), calculations for the specific heat capacity values of the two nanofluid samples were performed. The predictions from the analytical model were compared with the experimental data.

1. Synthesis Protocol, Experimental Apparatus and Measurement Procedure

In this study, potassium nitrate (KNO_3) and sodium nitrate ($NaNO_3$) mixture (KNO_3:$NaNO_3$ = 60:40 in molar ratio) was used as the base fluid (neat solvent). Nanomaterial samples were obtained by the mixing the pure nitrate salt mixture with alumina (Al_2O_3) nanoparticles. The specific heat capacity of the pure salt mixtures and the nanomaterials were measured using a differential scanning calorimeter (DSC). The specific heat capacity measurements were performed by subjecting the samples to repeated thermo-cycling over a temperature range of 150℃-500℃.

Potassium nitrate (KNO_3) and sodium nitrate ($NaNO_3$) were procured from Spectrum Inc. Alumina (Al_2O_3) nanoparticles were procured from Alfa Aesar. The nominal size of alumina (Al_2O_3) nanoparticles was ~50nm according to manufacturer's specification. However, in the nanomaterial samples the nanoparticle size was found to deviate significantly from the nominal size specified by the supplier. Scanning electron microscopy (SEM) images of the nanomaterial samples used in this study showed that alumina (Al_2O_3) nanoparticles were dispersed within the matrix (nitrate salt), as shown in Fig. 24 (a). From energy dispersive X-ray spectroscopy (EDS) analysis, shown in Fig. 25 (a), the existence of alumina (Al_2O_3) nanoparticles was confirmed in these nanomaterial samples. Hence, the nanoparticles were observed to be well dispersed in the matrix (nitrate salt mixture). However, Fig. 24 (b) shows that the alumina (Al_2O_3) nanoparticles were fairly agglomerated. The presence of the alumina (Al_2O_3) nanoparticles were verified in these samples also – by performing EDS analyses of the samples, as shown Fig. 25 (b).

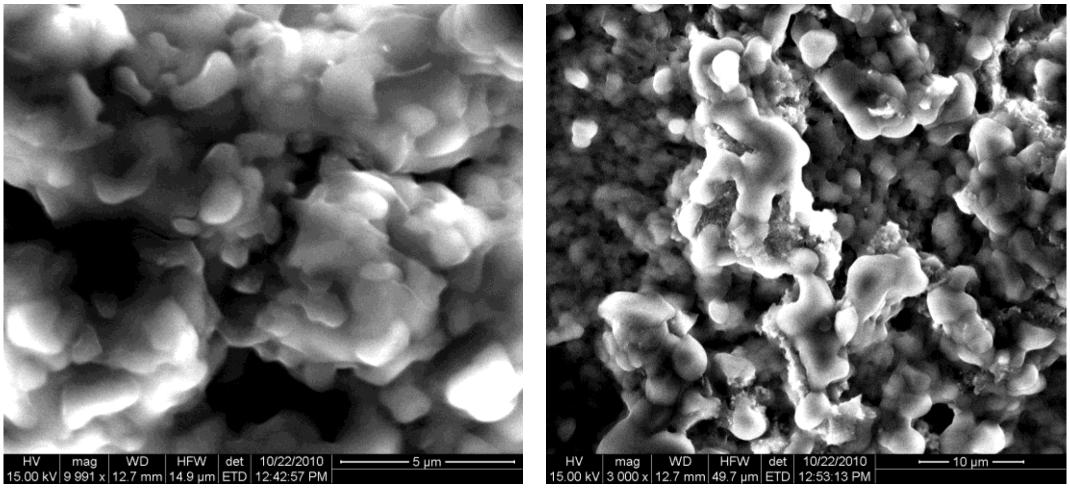

(a) (b)

Fig. 24. SEM images of the nanomaterial samples that were synthesized by dispersing alumina (Al_2O_3) nanoparticles in mixture of nitrate salt. The SEM images show nanomaterial samples with: (a) well-dispersed nanoparticles, and (b) agglomerated nanoparticles.

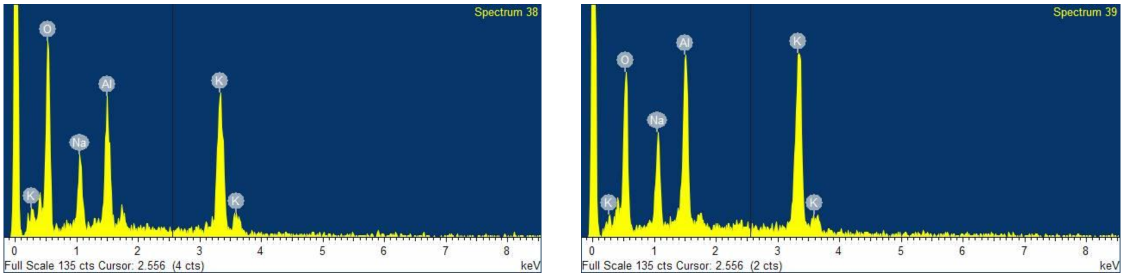

(a) (b)

Fig. 25. EDS analysis of nanomaterial samples that were shown in Fig. 24. EDS analyses for samples with (a) well-dispersed nanoparticles, and (b) agglomerated nanoparticles.

The synthesis protocol for the nitrate salt-based nanomaterials is described next. Initially, potassium nitrate and sodium nitrate mixture (KNO_3:$NaNO_3$ = 60:40 in molar ratio) and alumina (Al_2O_3) nanoparticles were dispensed into a glass vial of 25ml volume. The total mass of the mixture was 200mg. The vial was then filled with 20ml of distilled water. To ensure homogenous dispersion of the nanoparticles, the suspension was placed in an ultrasonication bath for 3 hours. The aqueous solution was poured into a glass petri dish for fast evaporation and then the glass petri dish was placed on a hot plate at 100℃ to evaporate the water from the solution. After the evaporation step, the nanomaterial sample (nitrate salt mixture containing the alumina nanoparticles) was scraped off. Using this protocol, nitrate salt-based nanomaterials were synthesized with 1% mass concentration of alumina (Al_2O_3) nanoparticles.

For performing the comparisons involving nanomaterial samples with agglomerated nanoparticles, another sample was synthesized where the aqueous solution was not ultrasonicated. Rather, the aqueous sample was manually shaken for a few minutes to obtain a homogeneous solution. Fig. 26 shows a schematic for the synthesis protocol used in this study. The measurement of the specific heat capacity of nanomaterials with alumina (Al_2O_3) nanoparticles is performed following the same procedure, as outlined in Chapter III-B.

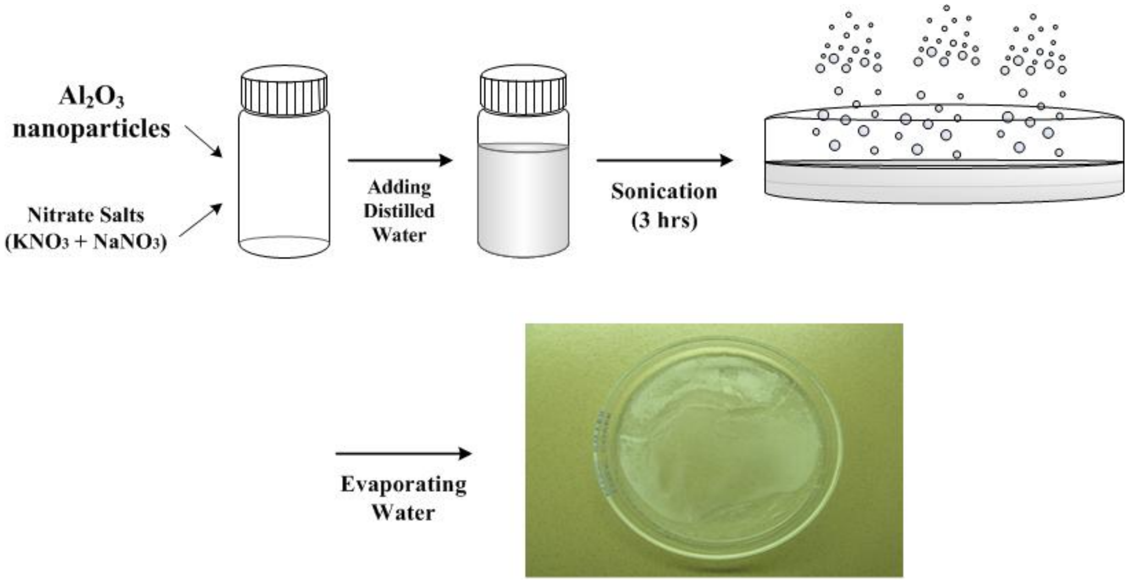

Fig. 26. Synthesis procedure of nitrate salt-based nanomaterials with alumina (Al_2O_3) nanoparticles.

2. Predictions from the Analytical Model

Considering a nanomaterial sample with a total mass (M) with a mass fraction (x) of the nanoparticles, the total mass of the nanoparticles in the sample is then (Mx). In these samples, the size distribution of the nanoparticles can be measured using TEM or SEM. In typical SEM and TEM images for these nanomaterial samples it is observed that there is sufficient variation in the size distribution of the nanoparticles and may not be consistent with the nominal size specified by the manufacturer (or supplier) of the nanoparticles. The analytical model used in this study assumes a narrow size distribution (or a fixed size) of the nanoparticles in the nanomaterials. The total number of nanoparticles is then expected to be ($Mx / \sum_i (m_n)_i A_i$) where $(m_n)_i$ is the mass of an individual spherical nanoparticle of diameter $(D_{np})_i$ and (A_i) is the fraction of the number of nanoparticles of diameter $(D_{np})_i$. The mass fraction of nanoparticles in the nanomaterial with respect to diameter $(D_{np})_i$ is ($B_i = (m_n)_i A_i / \sum_i (m_n)_i A_i$). The mass of the compressed phase with nanoparticles of diameter $(D_{np})_i$ is then expected to be ($MxB_i (m_s)_i / (m_n)_i$) where $(m_s)_i$ is the mass of the compressed phase that envelopes an individual nanoparticle of diameter $(D_{np})_i$. Hence, the total specific heat capacity (C_{total}) of nanomaterial is expressed as:

$$C_{total} = \frac{\left[MxC_n\right] + \left[\sum_i \frac{MxB_i}{(m_n)_i}(m_s)_i C_s\right] + \left[\left(M - Mx - \sum_i \frac{MxB_i}{(m_n)_i}(m_s)_i\right) C_l\right]}{M} \qquad \text{(III-3)}$$

where C_n, C_s and C_l are the specific heat capacity values of nanoparticle, compressed phase, and the bulk liquid phase (solvent), respectively. The mass of a spherical nanoparticle of diameter $(D_{np})_i$ can be expressed as:

$$(m_n)_i = \rho_n V_n = \rho_n \left(\frac{\pi (D_{np})_i^3}{6} \right) \tag{III-4}$$

where ρ_n and V_n are the density and volume of nanoparticle, respectively. The mass of compressed phase enveloping a single nanoparticle of diameter $(D_{np})_i$ can be expressed as:

$$(m_s)_i = \rho_s V_s = \rho_s \frac{4}{3} \pi \left[\left(\frac{(D_{np})_i}{2} + \delta + d_{sl} \right)^3 - \left(\frac{(D_{np})_i}{2} + d_{sl} \right)^3 \right] \tag{III-5}$$

where ρ_s and V_s are the density and volume of compressed phase, respectively.

3. Model Implementation

In this study, the specific heat capacity values are calculated using an analytical model for nanomaterials composed of alumina (Al_2O_3) nanoparticles dispersed in nitrate salt mixtures. The thermo-physical properties of the pure nitrate salt, the compressed phase, and alumina (Al_2O_3) nanoparticles are summarized in Table 15 and Table 16. These parameters were used to predict the specific heat capacity of the nanomaterials.

Table 15. The thermo-physical property values of the pure nitrate salt, the compressed phase, and the Al_2O_3 nanoparticles as well as the thickness of the compressed phase and the void layer for calculating specific heat capacity in liquid phase.

Nanofluid	ρ_n (g/m^3)	ρ_s (g/m^3)	C_n (J/g-K)	C_s (J/g-K)	C_l (J/g-K)	d_{sl} (nm)	δ (nm)
Al_2O_3/ nitrate salt	4.0	2.3	1.8	131.5	1.315	0.3	1.2

Table 16. The thermo-physical property values of the pure nitrate salt, the compressed phase, and the Al_2O_3 nanoparticles as well as the thickness of the compressed phase and the void layer for calculating specific heat capacity in solid phase.

Nanofluid	ρ_n (g/m^3)	ρ_s (g/m^3)	C_n (J/g-K)	C_s (J/g-K)	C_l (J/g-K)	d_{sl} (nm)	δ (nm)
Al_2O_3/ nitrate salt	4.0	1.6	1.4	118.9	1.189	0.3	1.2

In previous studies reported in the literature, the molar heat capacity of nanostructured alumina (Al_2O_3) in the temperature range from 78K to 370K was measured and compared with that of the coarse-grained alumina (Al_2O_3) [44]. Based on the literature reports, the specific heat capacity values of alumina (Al_2O_3) nanoparticles used in this study are estimated for temperatures up to 500℃. Hence, specific heat capacity value of alumina (Al_2O_3) nanoparticle for these calculations is assumed to be 1.8J/g-K which is the average value in the temperature range from 250℃ to 500℃ and 1.4J/g-K which is the average value in the temperature range from 160℃ to 200℃. The density value of alumina (Al_2O_3) nanoparticle is assumed to be the same as that of the bulk materials. The specific heat capacity value of pure nitrate salt mixture (KNO_3:$NaNO_3$ 60:40 in molar ratio) is 1.315J/g-K in liquid phase and 1.189J/g-K in solid phase (obtained from experimental measurements presented in Chapter III-B). The molecules in the compressed phase surrounding a nanoparticle surface are reported to behave like a solid phase [39-40]. Currently there is no available experimental or numerical data for predicting the thermo-physical properties of the compressed phase. In this study, density of the compressed phase is assumed to be 30% higher than that of the pure nitrate salt mixture in liquid phase. Specific heat capacity value of the compressed phase is assumed to be 100 times the specific heat capacity value of the pure nitrate salt mixture (KNO_3:$NaNO_3$ 60:40 in molar ratio) as shown in Chapter III-B. In a number of molecular dynamics (MD) simulations, the liquid molecules were found to represent a disordered structure observed in the liquid phase at a distance greater than ~1.2nm from the nanoparticle surface [14, 40, 48, 51]. Based on the results, the thickness of the compressed phase is assumed to be 1.2nm. Furthermore, the void layer between the nanoparticle surface and the first molecule in the compressed phase is estimated to be 0.3nm. The mass fraction of nanoparticles in the nanomaterial with respect to diameter $(D_{np})_i$ is shown in Fig. 27 based on SEM images and specification of the alumina (Al_2O_3) nanoparticle from manufacturer.

It is assumed that the nanomaterial samples with well-dispersed nanoparticles, the nominal size of the nanoparticles is 30nm, along with a normal distribution for the size of the nanoparticles (based on manufacturer specification) as shown in Fig. 27 (a). The size of the agglomerated nanoparticles is assumed to be 6μm, where the size distribution is assumed to follow a normal distribution, based on the SEM images, as shown in Fig. 27 (b).

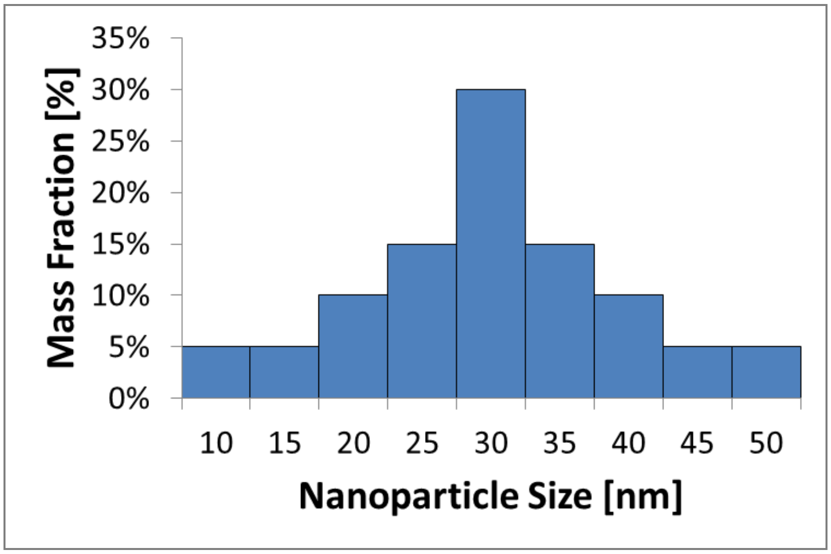

(a)

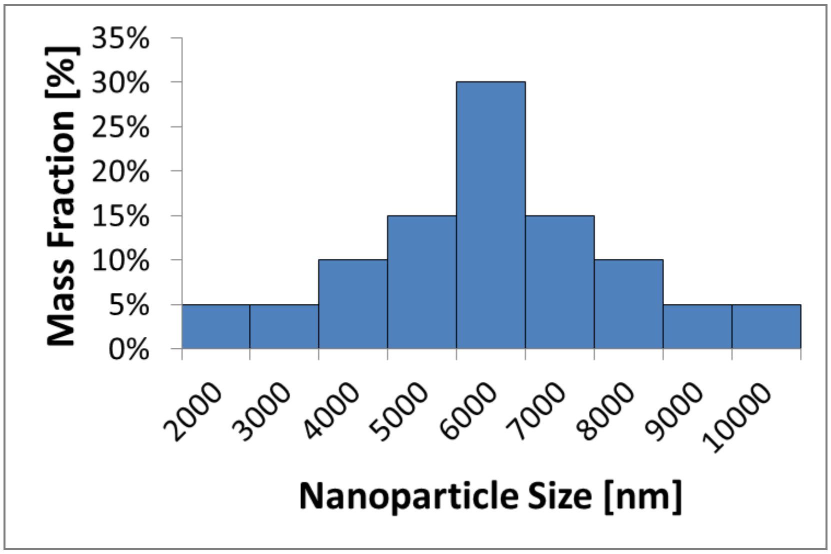

(b)

Fig. 27. Mass fraction distribution of nanoparticles: (a) well-dispersed nanomaterial, (b) agglomerated nanomaterial.

4. Results and Discussions

The measurement of the specific heat capacity of the nitrate salt-based nanomaterials were performed for each sample with 1% mass concentrations of alumina (Al_2O_3) nanoparticles. The average specific heat capacity values for each thermo-cycle obtained from the DSC measurements for the each sample of nanomaterials are shown in Table 17 and Table 18. These results are also plotted in Fig. 28 where the specific heat capacity is plotted as a function of temperature by averaging the measurement results from each thermo-cycle. The results show that the specific heat capacity values of nitrate salt-based nanomaterials with alumina (Al_2O_3) nanoparticles are enhanced compared to pure nitrate salt for enhancement of 11% in solid phase and 19% in liquid phase for well dispersed nanomaterial. In the case of agglomerated nanomaterial, however, the result shows no significant enhancement in both solid and liquid phase.

Table 17. Measurement results of specific heat capacity of nitrate salt-based nanomaterial with 1% mass concentration of well dispersed alumina (Al_2O_3) nanoparticles.

Thermo-cycle	Specific Heat (J/g-K) in solid phase	Specific Heat (J/g-K) in liquid phase
1st run	1.303	1.544
2nd run	1.319	1.561
3rd run	1.323	1.580
4th run	1.329	1.572
5th run	1.345	1.570
Average	1.324	1.566
Enhancement	11%	19%
STD	0.015	0.014

Table 18. Measurement results of specific heat capacity of nitrate salt-based nanomaterial with 1% mass concentration of agglomerated alumina (Al_2O_3) nanoparticles.

Thermo-cycle	Specific Heat (J/g-K) in solid phase	Specific Heat (J/g-K) in liquid phase
1st run	1.220	1.303
2nd run	1.206	1.331
3rd run	1.207	1.332
4th run	1.216	1.342
5th run	1.225	1.342
Average	1.215	1.330
Enhancement	2%	1%
STD	0.008	0.016

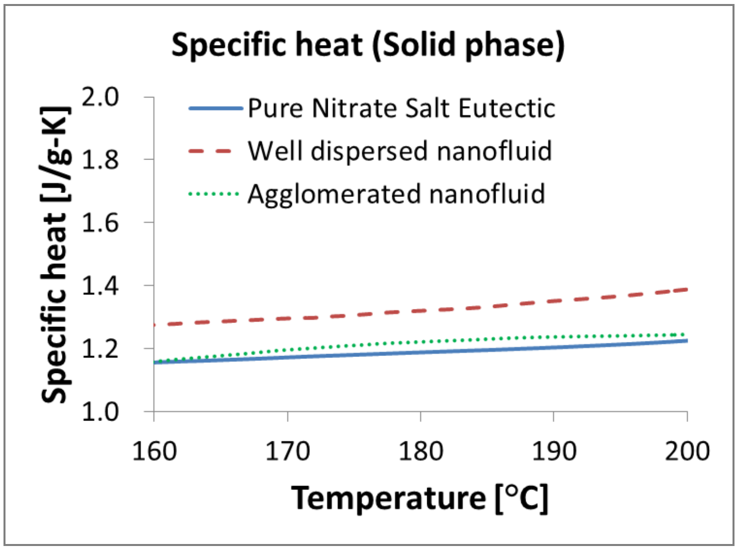

(a)

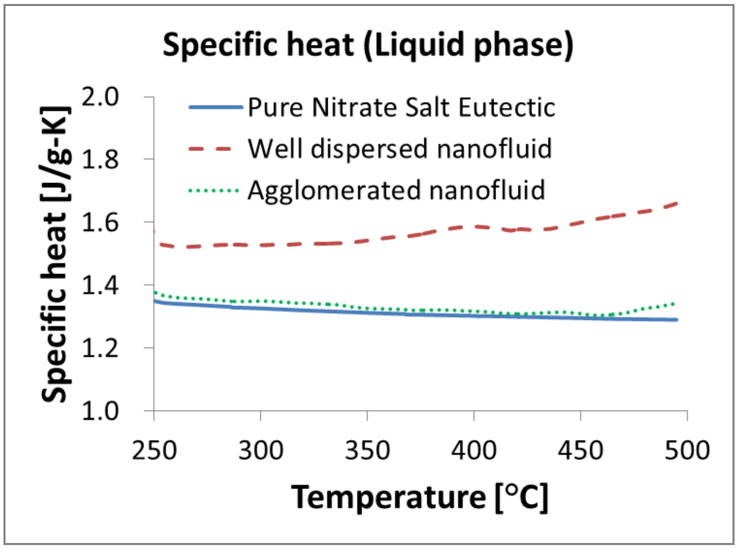

(b)

Fig. 28. Specific heat capacity values of nitrate salt-based nanomaterial with alumina (Al_2O_3) nanoparticles as a function of temperature: (a) specific heat capacity values in solid phase, (b) specific heat capacity values in liquid phase.

Using the analytical mode (based on assumed size distributions), the specific heat capacity values of nitrate salt-based nanomaterials in liquid phase and solid phase are calculated and compared to the experimental measurement results (as shown in Table 19). The results show that the measurement values are good agreement with the calculation values.

The implication of the analytical model is that the samples with well-dispersed nanoparticles have higher levels of enhancement of specific heat capacity values compared to samples with significant agglomerations of the nanoparticles. According to the analytical model, for samples with well dispersed nanoparticles, the specific heat capacity increases significantly with increase in mass concentration of the nanoparticles. On the other hand, for samples with agglomerated nanoparticles the specific heat capacity is relatively insensitive to the mass concentration of the nanoparticles – for the range of parameters used in this study, as shown in Fig. 29.

The implication of the analytical model is that the total specific heat capacity of nanomaterial increases with the decrease in the nominal size of nanoparticles, particularly due to increasingly significant contribution from the compressed phase for smaller size of the nanoparticles. In addition, the specific heat capacity values of nanomaterials increases more significantly with the increase in mass concentration of nanoparticles, especially at smaller nanoparticle sizes. If mass concentration of nanoparticle is increased, enhancement of specific heat capacity will be increased as shown in Fig. 29. However, at higher mass concentrations the propensity for agglomeration of nanoparticles increases, causing any anticipated enhancements to disappear.

Table 19. Predictions from the analytical model compared with experimental measurements for the specific heat capacity of the nanomaterial samples containing well dispersed nanoparticles and agglomerated nanoparticles. The nanomaterials contain alumina (Al_2O_3) nanoparticles.

Samples	Calculation (J/g-K)		Measurement (J/g-K)	
	liquid phase	solid phase	liquid phase	solid phase
Well dispersed nanomaterial	1.566	1.340	1.566	1.324
Agglomerated nanomaterial	1.321	1.191	1.330	1.215

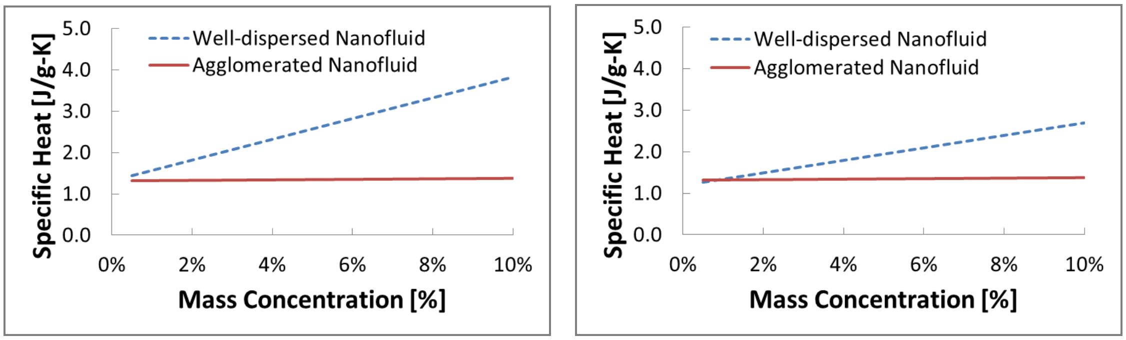

(a) (b)

Fig. 29. Specific heat capacity values of nitrate salt-based nanomaterial with alumina (Al_2O_3) nanoparticles as a function of mass concentration of nanoparticles. The predictions are calculated for well-dispersed nanoparticles (nominal diameter of ~ 30 nm) and agglomerated nanoparticles (nominal diameter of ~6 microns): (a) nanofluid (liquid phase), (b) nanocomposite (solid phase).

5. Summary and Conclusions

Experimental results show that the specific heat capacity values of nitrate salt-based nanomaterials with alumina (Al_2O_3) nanoparticles were enhanced by 11% in the solid phase and 19% in the liquid phase - compared to that of the pure nitrate salt mixture (KNO_3:$NaNO_3$ in 60:40 molar ratio). However, for the samples with agglomerated nanoparticles no enhancement in the specific heat capacity was observed. The main reason for the specific heat capacity enhancement is expected to be the formation of the compressed phase of solvent molecules on the surface of the nanoparticles. For agglomerated nanoparticles (with smaller specific surface area) the contribution from the compressed phase to the total specific heat capacity of the mixture is marginal. The predictions from the assumed analytical model were found to be consistent with the experimental data.

D. Specific Heat Capacity of Nanomaterials Containing Oxide Nanoparticles

The specific heat capacity of nitrate salt mixture (KNO_3:$NaNO_3$ = 60:40 in molar ratio) was measured after dispersing minute concentration of oxide nanoparticles. The oxide nanoparticles used in this study are: silica (SiO_2) and titania (TiO_2). The experiments were performed for mass concentrations of oxide nanoparticles fixed at 1% and 2%. The specific heat capacity of the nitrate salt in the solid phase was observed to be enhanced by as much as ~8-18% on addition of the nanoparticles. Furthermore, the specific heat capacity values in liquid phase were observed to be enhanced by ~9-25%. Hence, the application of these oxide nanoparticles: silica (SiO_2) and titania (TiO_2) to nitrate salt can be quite effective in reducing the cost of solar thermal energy.

1. Synthesis Protocol, Experimental Apparatus and Measurement Procedure

In this study, potassium nitrate and sodium nitrate mixture (60:40 in molar ratio) was used as the base fluid (neat solvent). Silica (SiO_2) nanoparticles or titania (TiO_2) nanoparticles were dispersed in the pure salt mixture. The measurements were performed using a differential scanning calorimeter (DSC). Measurements were performed over a temperature range of 150℃-500℃. Potassium nitrate (KNO_3) and sodium nitrate ($NaNO_3$) were procured from Spectrum Inc. The silica (SiO_2) and titania (TiO_2) nanoparticles were procured from Meliorum Technologies, Inc. The nominal size of the silica (SiO_2) nanoparticles was ~10nm according to manufacturer's specification. The nominal size of the titania (TiO_2) nanoparticles was also ~10nm according to manufacturer's specification.

The synthesis protocol for the nitrate salt-based nanomaterials containing silica (SiO_2) or titania (TiO_2) nanoparticles is the same as described in Chapter III-C, i.e., by evaporation method using a glass petri dish. Using this protocol, the nitrate salt-based nanomaterials were synthesized with mass concentration of nanoparticles fixed at 1% and 2%. The measurement of the specific heat capacity of nanomaterials with silica (SiO_2) or titania (TiO_2) nanoparticles was performed using the same thermo-cycling protocol (discussed in Chapter III-B and III-C). The nanomaterial samples were characterized using scanning electron microscopy (SEM) and the representative SEM images are shown in Fig. 30. SEM images show that the nanoparticles were enveloped with nitrate salt. From energy dispersive X-ray spectroscopy (EDS) analysis, the existence of silica (SiO_2) and titania (TiO_2) nanoparticle was confirmed as shown in Fig. 31.

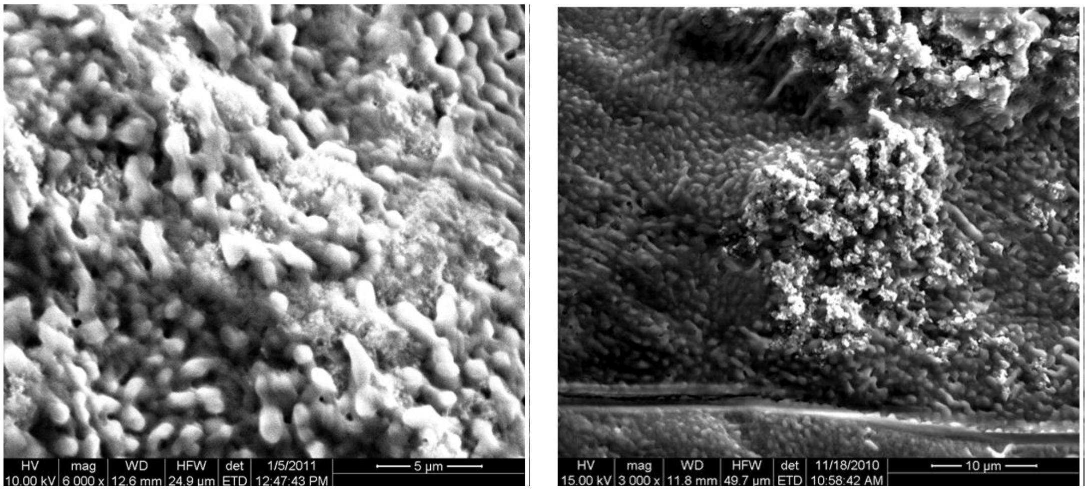

(a) (b)

Fig. 30. SEM images of the nanomaterial samples that were synthesized by dispersing nanoparticles in mixture of nitrate salt. The SEM images show nanomaterial samples with: (a) silica (SiO_2) nanoparticles, and (b) titania (TiO_2) nanoparticles.

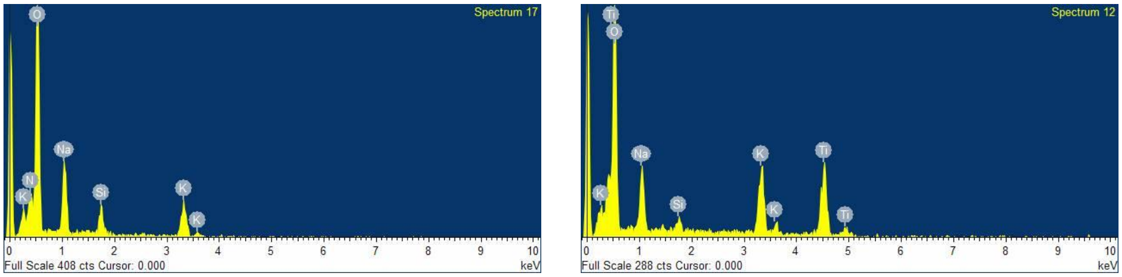

(a) (b)

Fig. 31. EDS analysis of nanomaterial samples that were shown in Fig. 30. EDS analyses for samples with (a) silica (SiO_2) nanoparticles, and (b) titania (TiO_2) nanoparticles.

2. Results and Discussions

The measurement of specific heat capacity values of the pure salt mixture samples and the nanomaterial samples using the DSC protocol are listed in Table 20, Table 21, Table 22, and Table 23. These results were also plotted in Fig. 32 and Fig. 33 where the specific heat capacity values are plotted as a function of temperature by taking the average of the individual measurements at a particular temperature for all the thermo-cycling measurements performed in a single experiment for a given sample.

The results show that the specific heat capacity values of the nitrate salt mixture is enhanced significantly when silica (SiO_2) and titania (TiO_2) nanoparticles are dispersed. The enhancements obtained by dispersing silica (SiO_2) nanoparticles range from 11-18% in the solid phase and 11-23% in the liquid phase. The enhancements obtained by dispersing titania (TiO_2) nanoparticles range from 8-18% in the solid phase and 9-25% in the liquid phase.

3. Summary and Conclusions

The level of enhancement in the specific heat capacity values increases with the increase in mass concentration for the range of experimental parameters used in this study.

Table 20. Specific heat capacity of pure nitrate salt mixture and corresponding nanomaterials synthesized using silica (SiO_2) nanoparticles at a mass concentration of 1%.

Thermo-cycle	Specific Heat (J/g-K) in solid phase	Specific Heat (J/g-K) in liquid phase
1st run	1.300	1.440
2nd run	1.323	1.460
3rd run	1.329	1.463
4th run	1.326	1.469
5th run	1.330	1.490
Average	1.322	1.464
Enhancement	11%	11.3%
STD	0.013	0.018

Table 21. Specific heat capacity of pure nitrate salt mixture and corresponding nanomaterials synthesized using silica (SiO_2) nanoparticles at a mass concentration of 2%.

Thermo-cycle	Specific Heat (J/g-K) in solid phase	Specific Heat (J/g-K) in liquid phase
1st run	1.405	1.637
2nd run	1.414	1.630
3rd run	1.409	1.616
4th run	1.399	1.616
5th run	1.394	1.607
Average	1.404	1.621
Enhancement	17.9%	23.3%
STD	0.008	0.012

Table 22. Specific heat capacity of pure nitrate salt mixture and corresponding nanomaterials synthesized using titania (TiO_2) nanoparticles at a mass concentration of 1%.

Thermo-cycle	Specific Heat (J/g-K) in solid phase	Specific Heat (J/g-K) in liquid phase
1st run	1.303	1.424
2nd run	1.273	1.429
3rd run	1.284	1.435
4th run	1.260	1.441
5th run	1.305	1.458
Average	1.285	1.438
Enhancement	7.9%	9.3%
STD	0.019	0.013

Table 23. Specific heat capacity of pure nitrate salt mixture and corresponding nanomaterials synthesized using titania (TiO_2) nanoparticles at a mass concentration of 2%.

Thermo-cycle	Specific Heat (J/g-K) in solid phase	Specific Heat (J/g-K) in liquid phase
1st run	1.429	1.682
2nd run	1.420	1.658
3rd run	1.409	1.633
4th run	1.398	1.625
5th run	1.388	1.608
Average	1.409	1.641
Enhancement	18.3%	24.8%
STD	0.017	0.029

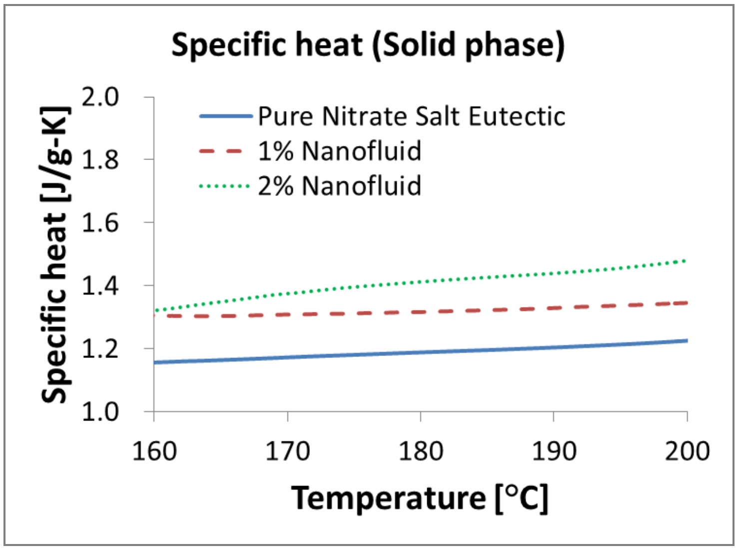

(a)

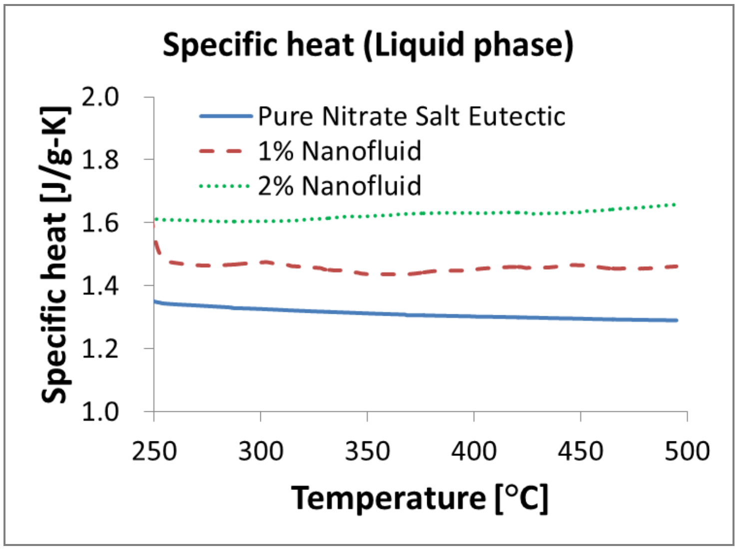

(b)

Fig. 32. Specific heat capacity as a function of temperature measured for samples of pure nitrate salt mixture (KNO_3:$NaNO_3$ = 60:40 in molar ratio) and the corresponding nanomaterial samples synthesized by dispersing silica (SiO_2) nanoparticles at a mass fraction of 1% and 2%; for: (a) solid phase, and (b) liquid phase.

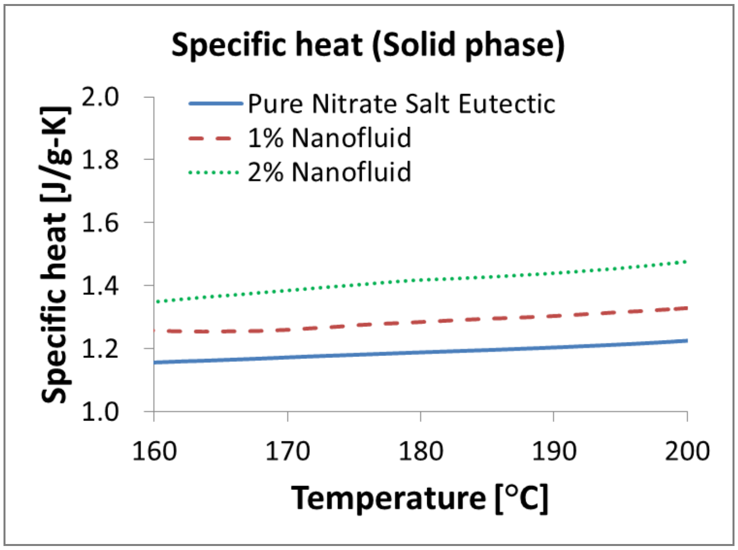

(a)

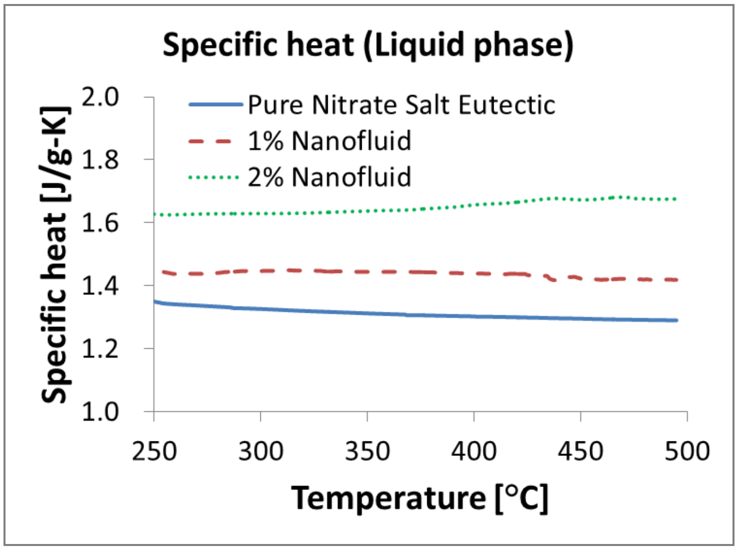

(b)

Fig. 33. Specific heat capacity as a function of temperature measured for samples of pure nitrate salt mixture (KNO_3:$NaNO_3$ = 60:40 in molar ratio) and the corresponding nanomaterial samples synthesized by dispersing titania (TiO_2) nanoparticles at a mass fraction of 1% and 2%; for: (a) solid phase, and (b) liquid phase.

E. Effect of Composition of Solvent Material for Silica (SiO_2) Nanomaterials

The specific heat capacity of nanomaterials was explored for silica (SiO_2) nanomaterials by varying the composition of the solvent material. The mass concentration of the silica (SiO_2) nanoparticles was fixed at 1% in these experiments. In this study, three different samples for the pure salt mixtures were used. The composition of the pure salt mixtures (used as the solvent phase) is listed as follows:

(a) Potassium nitrate: lithium nitrate (KNO_3:$LiNO_3$ = 58.8 : 41.2 in molar ratio).
(b) Lithium nitrate: sodium nitrate ($LiNO_3$: $NaNO_3$ = 45:55 in molar ratio).
(c) Lithium chloride: lithium nitrate (LiCl : $LiNO_3$ = 12.5:87.5 in molar ratio).

1. Potassium Nitrate: Lithium Nitrate Mixture (KNO_3:$LiNO_3$=58.8:41.2 in molar ratio)

The melting point of the potassium nitrate and lithium nitrate mixture (KNO_3:$LiNO_3$=58.8:41.2 in molar ratio), which was used as the solvent, is 130℃. The specific heat capacity measurements, of the pure salt mixtures and nanomaterials containing SiO_2 nanoparticles, was performed using thermo-cycling in DSC and ASTM-E1269 protocol; and are presented in Table 24. The measurements were performed over a temperature range of 55℃–400℃. The samples were characterized using scanning electron microscopy (SEM), and the representative images are shown in Fig. 34. The average specific heat capacity values in solid phase are for the temperature range of 75℃-100℃ and for the liquid phase are for the temperature range of 170℃-390℃.

The average value of the specific heat capacity of the pure salt mixture was measured to be 1.297J/g-K in the solid phase and 1.592J/g-K in the liquid phase. These results are listed in Table 25 and also plotted in Fig. 35 (where the specific heat capacity values are plotted as a function of temperature by taking the average of the measurements from each thermo-cycle for a particular temperature). The results show that the average values of the specific heat capacity of the nanomaterial samples are enhanced by ~7% in the liquid phase (which is marginally higher than the measurement uncertainty) – while no significant enhancement is observed for the solid phase.

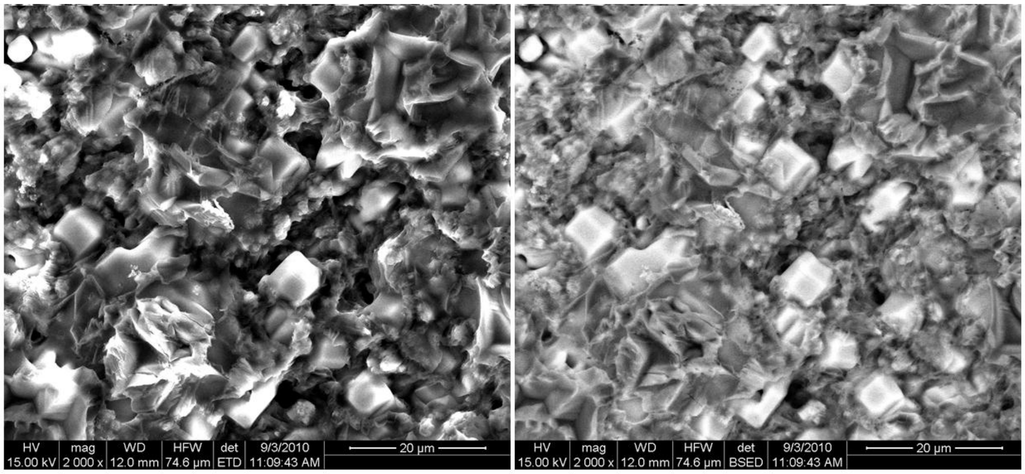

Fig. 34. SEM images of the potassium nitrate and lithium nitrate mixture (KNO_3:$LiNO_3$ = 58.8:41.2 in molar ratio) nanomaterials using silica (SiO_2) nanoparticles with 1% mass concentration: (a) secondary electron image, (b) backscattered electron image.

Table 24. Specific heat capacity of pure salt mixture (KNO_3:$LiNO_3$=58.8:41.2 molar ratio).

Sample No.	Specific Heat (J/g-K) in solid phase	Specific Heat (J/g-K) in liquid phase
1	1.325	1.592
2	1.268	1.570
Average	1.297	1.581
STD	0.040	0.016

Table 25. Average specific heat capacity of nanomaterial containing SiO_2 nanoparticles at mass concentration of 1% and solvent composed of binary salt mixture (KNO_3:$LiNO_3$ = 58.8 : 41.2 in molar ratio).

Thermo-cycle	Specific Heat (J/g-K) in solid phase	Specific Heat (J/g-K) in liquid phase
1st run	1.306	1.674
2nd run	1.325	1.666
3rd run	1.334	1.698
4th run	1.330	1.698
5th run	1.330	1.707
Average	1.325	1.689
Enhancement	1.9%	6.9%
STD	0.011	0.018

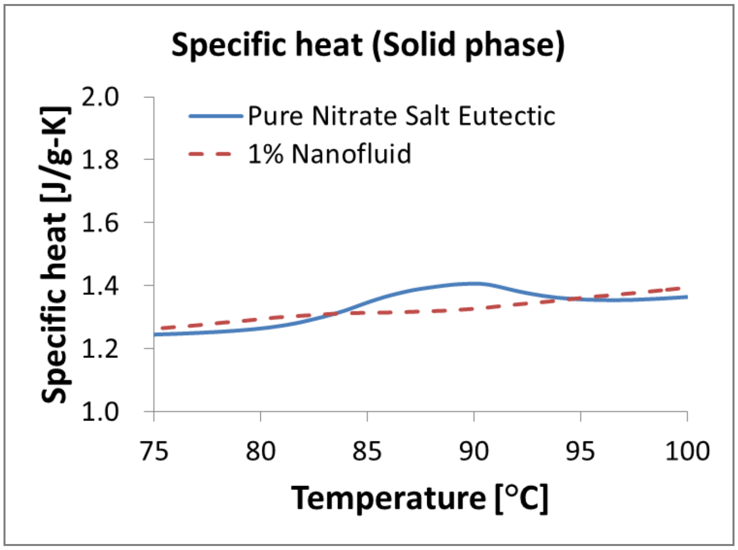

(a)

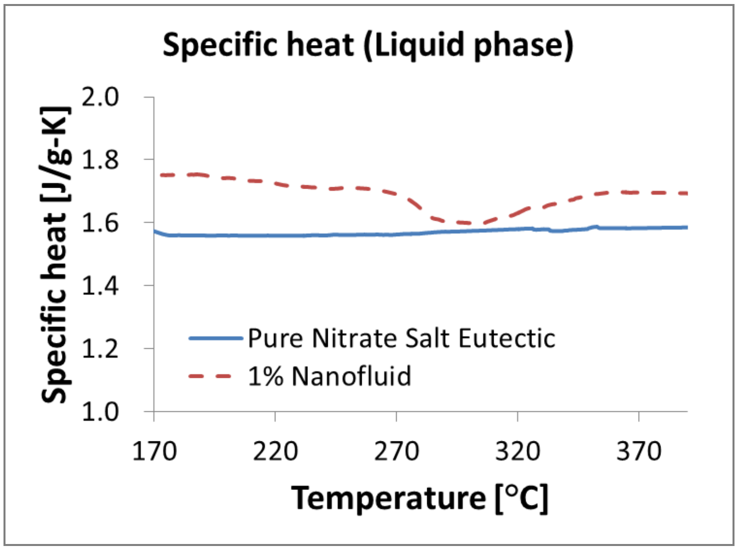

(b)

Fig. 35. Specific heat capacity of nanomaterial containing SiO_2 nanoparticles at mass concentration of 1% and solvent composed of binary salt mixture (KNO_3:$LiNO_3$ = 58.8 : 41.2 molar ratio). (a) solid phase. (b) liquid phase.

2. Lithium Nitrate: Sodium Nitrate Mixture ($LiNO_3$:$NaNO_3$=45:55 in molar ratio)

In this study, Lithium nitrate and sodium nitrate mixture ($LiNO_3$:$NaNO_3$=45:55 in molar ratio) was used as the base fluid (or neat solvent) and the corresponding nanomaterial samples were synthesized by dispersing SiO_2 nanoparticles at a mass fraction of 1%. The melting point of this solvent composition is 192℃. The specific heat capacity measurements were performed using a differential scanning calorimeter (DSC) and by implementing the ASTM-E1269 protocol. The measurements were performed for a temperature range of 155℃–400℃. The nanomaterials were characterized using scanning electron microscopy (SEM), and the representative images are shown in Fig. 36.

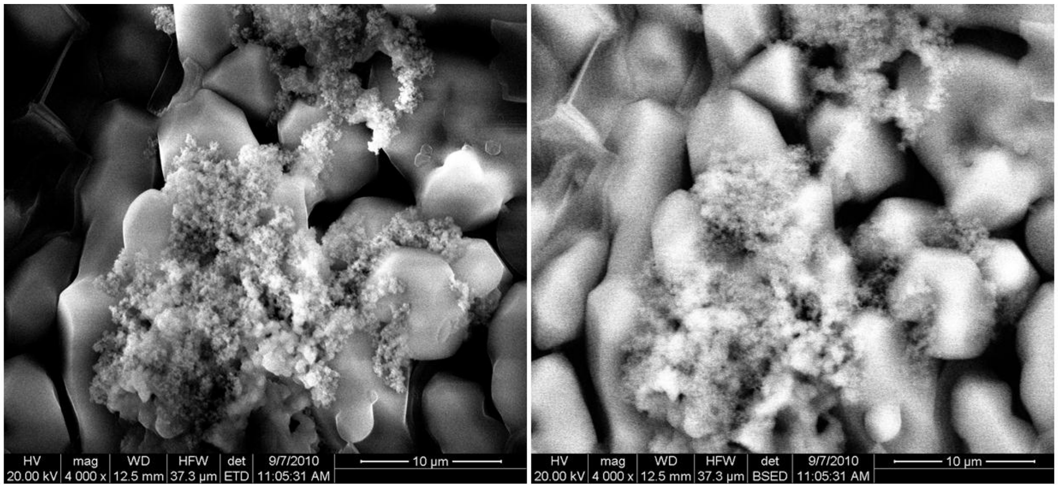

Fig. 36. SEM images of the lithium nitrate and sodium nitrate mixture ($LiNO_3$:$NaNO_3$ = 45:55 in molar ratio) nanomaterials using silica (SiO_2) nanoparticles with 1% mass concentration: (a) secondary electron image, (b) backscattered electron image.

Table 26 lists the measured values of specific heat capacity for the pure salt mixture. The average value of the specific heat capacity in the solid phase is obtained for a temperature range of 160℃–180℃ and in the liquid phase is obtained for a temperature range of 240℃–390℃. The average value of the specific heat capacity of the pure salt mixture was measured to be 1.418J/g-K in the solid phase and 1.740J/g-K in the liquid phase. Table 27 lists the measured values of specific heat capacity for the nanomaterial samples. These results are also plotted in Fig. 37 where the specific heat capacity values are plotted as a function of temperature. The results show that the specific heat capacity values of the nanomaterials with SiO_2 nanoparticles were enhanced c by 9.2% in liquid phase (which is significantly higher than the measurement uncertainty) while no significant enhancement was observed in the solid phase of the nanomaterial samples.

Table 26. Specific heat capacity of pure salt mixture ($LiNO_3$:$NaNO_3$=45:55 molar ratio).

Sample No.	Specific Heat (J/g-K) in solid phase	Specific Heat (J/g-K) in liquid phase
1	1.423	1.693
2	1.412	1.787
Average	1.418	1.740
STD	0.008	0.066

Table 27. Average specific heat capacity of nanomaterial containing SiO_2 nanoparticles at mass concentration of 1% and solvent composed of binary salt mixture ($LiNO_3$:$NaNO_3$=45:55 molar ratio).

Thermo-cycle	Specific Heat (J/g-K) in solid phase	Specific Heat (J/g-K) in liquid phase
1st run	1.440	1.874
2nd run	1.455	1.898
3rd run	1.461	1.905
4th run	1.467	1.910
5th run	1.471	1.915
Average	1.459	1.900
Enhancement	2.7%	9.2%
STD	0.012	0.016

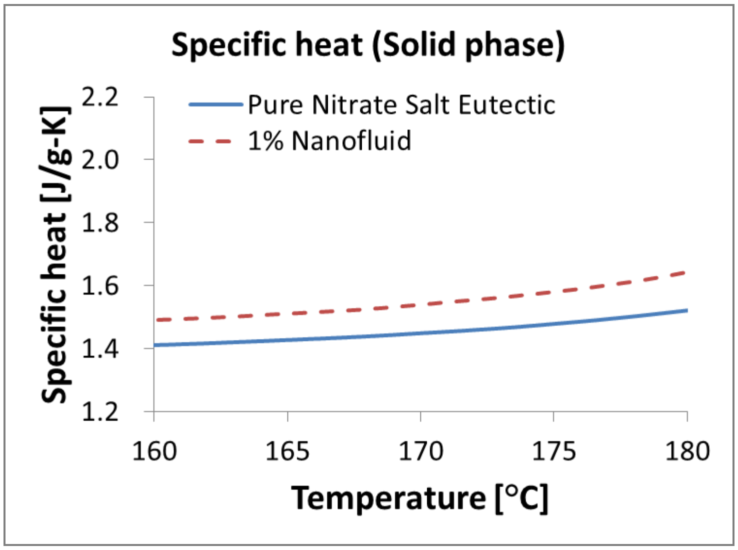

(a)

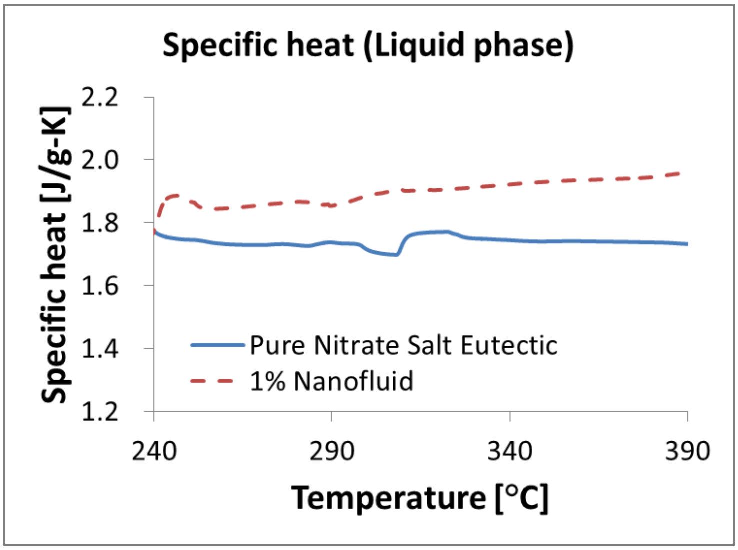

(b)

Fig. 37. Specific heat capacity of nanomaterial containing SiO_2 nanoparticles at mass concentration of 1% and solvent composed of binary salt mixture ($LiNO_3$:$NaNO_3$=45:55 molar ratio). (a) solid phase. (b) liquid phase.

3. Lithium Chloride: Lithium Nitrate Mixture ($LiCl:LiNO_3$=12.5:87.5 in molar ratio)

In this study, lithium chloride and lithium nitrate mixture ($LiCl:LiNO_3$=12.5:87.5 in molar ratio) was used as the base fluid (or neat solvent) and the corresponding nanomaterial samples were synthesized by dispersing SiO_2 nanoparticles at a mass fraction of 1%. The melting point of this solvent composition is 244℃. The specific heat capacity measurements were performed using a differential scanning calorimeter (DSC) and by implementing the ASTM-E1269 protocol. Measurements were performed for a temperature range of 155℃–345℃. The nanomaterials were characterized using scanning electron microscopy (SEM), and the representative images are shown in Fig. 38.

Table 28 lists the measured values of the average specific heat capacity of the samples of the pure salt mixture. The average value of the specific heat capacity in the solid phase is obtained for the temperature range of 160℃-220℃ and in the liquid phase is obtained for the temperature range of 280℃-345℃. The average value of the specific heat capacity of the pure salt mixture was measured to be 1.493J/g-K in the solid phase and 1.928J/g-K in the liquid phase. The average values of the specific heat capacity for the nanomaterial samples are listed in Table 29. These results are also plotted in Fig. 39 where the specific heat capacity values are plotted as a function of temperature. The results show that the specific heat capacity values of the nanomaterials samples are enhanced by 14.8% in the solid phase and 10.5% in the liquid phase.

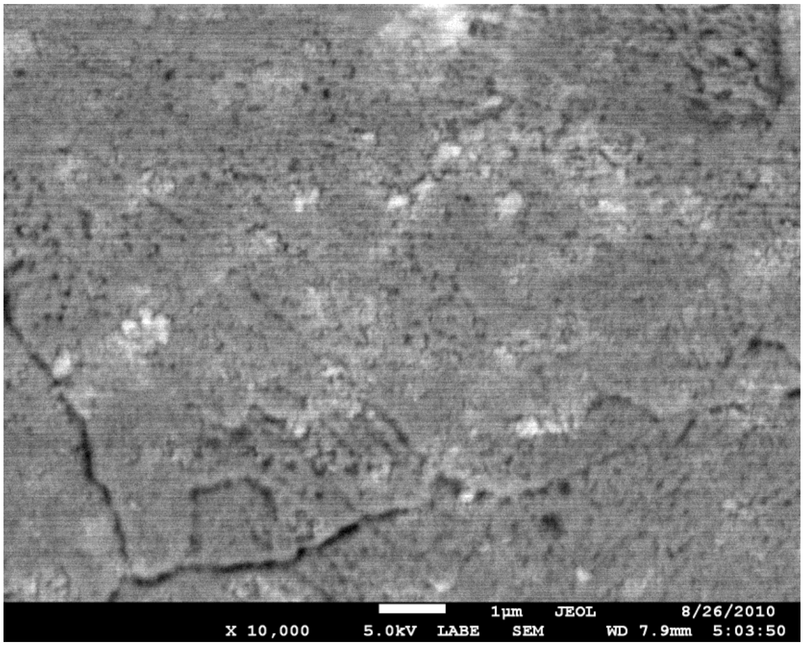

Fig. 38. SEM images of the lithium chloride and lithium nitrate mixture (LiCl:$LiNO_3$ = 12.5:87.5 in molar ratio) nanomaterials using silica (SiO_2) nanoparticles with 1% mass concentration.

Table 28. Specific heat capacity of pure salt mixture ($LiCl:LiNO_3$=12.5:87.5 molar ratio).

Sample No.	Specific Heat (J/g-K) in solid phase	Specific Heat (J/g-K) in liquid phase
1	1.486	1.920
2	1.499	1.936
Average	1.493	1.928
STD	0.009	0.011

Table 29. Average specific heat capacity of nanomaterial containing SiO_2 nanoparticles at mass concentration of 1% and solvent composed of binary salt mixture ($LiCl:LiNO_3$=12.5:87.5 molar ratio).

Thermo-cycle	Specific Heat (J/g-K) in solid phase	Specific Heat (J/g-K) in liquid phase
1st run	1.708	2.109
2nd run	1.717	2.128
3rd run	1.703	2.138
4th run	1.710	2.144
5th run	1.718	2.145
Average	1.711	2.133
Enhancement	14.8%	10.5%
STD	0.006	0.015

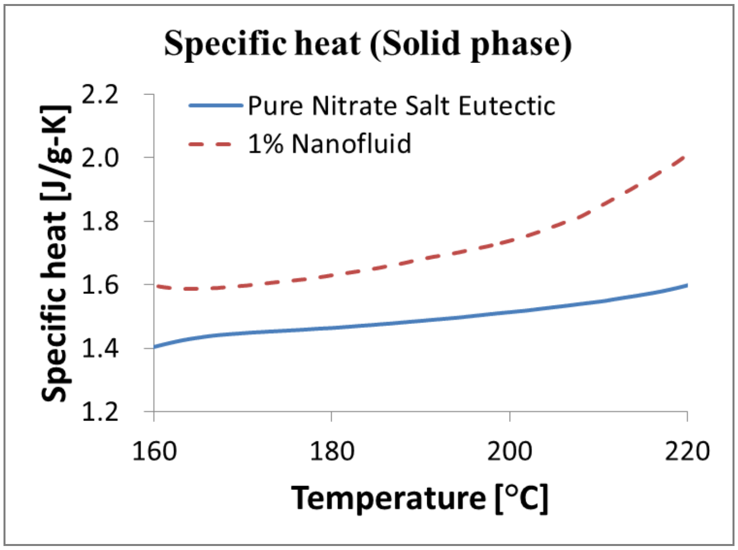

(a)

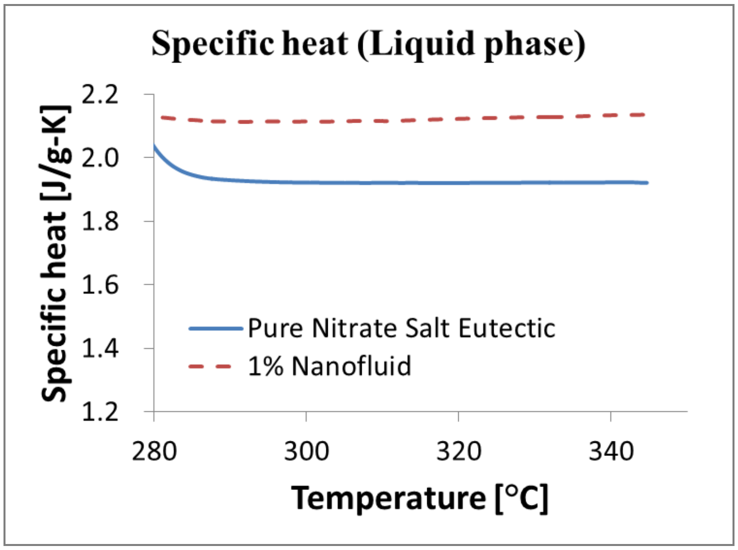

(b)

Fig. 39. Specific heat capacity of nanomaterial containing SiO_2 nanoparticles at mass concentration of 1% and solvent composed of binary salt mixture ($LiCl:LiNO_3$=12.5:87.5 molar ratio). (a) solid phase. (b) liquid phase.

F. The Effects of Solvent Material and Nanoparticle Using MD Simulation

In this study, MD simulations were performed to explore the effects of solvent material on the properties of the nanomaterial. As mentioned in Chapter II-A, compressed phase at solid-liquid interface affects the specific heat capacity enhancement of nanomaterials. From the MD simulation results, a density plot is generated to visualize the spatial variation of density within the simulation domain. In addition, the spatial variation of concentration of each species is obtained from the simulation.

To explore the effect of the solvent material, the simulation domains are prepared by placing a nanoparticle (SiO_2) of 6Å diameter at the center of the simulation box. The solvent molecules are placed within the simulation domain and surrounding the nanoparticle. The solvent material is composed of (a) potassium nitrate and lithium nitrate mixture (KNO_3:$LiNO_3$ = 58.8:41.2 in molar ratio) as well as (b) lithium nitrate and sodium nitrate mixture ($LiNO_3$:$NaNO_3$ = 45:55 in molar ratio). As mentioned in Chapter II-B, MD simulations are implemented for each simulation domain. Fig. 40 shows the molar ratio distribution for each solvent material. Red “dash” line indicates molar ratio of pure solvent material. The results indicate that the molar ratio of the components of the solvent material approaches that of the pure solvent at distances away far from the nanoparticle surface. From the results, compressed phase thickness of the case of lithium nitrate and sodium nitrate mixture ($LiNO_3$:$NaNO_3$ = 45:55 in molar ratio) is larger than potassium nitrate and lithium nitrate mixture (KNO_3:$LiNO_3$ = 58.8:41.2 in molar ratio). Sodium atoms form the compressed phase with larger thickness compared to potassium atoms due to greater adhesion forces between sodium and the silica (SiO_2)

nanoparticle than those between potassium and the silica (SiO_2) nanoparticle. As shown in previous sections, the enhancement of specific heat capacity of nanomaterial using the lithium nitrate and sodium nitrate mixture ($LiNO_3$:$NaNO_3$ = 45:55 in molar ratio) as a base material is larger than that using potassium nitrate and lithium nitrate mixture (KNO_3:$LiNO_3$ = 58.8:41.2 in molar ratio). This is possibly because of the greater adhesion forces between sodium and the silica (SiO_2) nanoparticle resulting in the formation of thicker compressed phase.

To explore the effect of nanoparticle, the simulation domains are prepared by placing different nanoparticles (SiO_2 and Al_2O_3) of 5Å diameter at the center of the simulation box. The solvent material is potassium nitrate and sodium nitrate mixture (KNO_3:$NaNO_3$ = 60:40 in molar ratio). Fig. 41 shows molar ratio distribution for each nanomaterial. From the MD simulation results, compressed phase thickness of nanomaterial using alumina (Al_2O_3) nanoparticle is larger than that using silica (SiO_2) nanoparticle. Sodium atoms form the compressed phase with larger thickness due to greater adhesion forces between sodium and the alumina (Al_2O_3) nanoparticle compared to those between sodium and the silica (SiO_2) nanoparticle. In experimental results, the enhancement of specific heat capacity of nanomaterial using alumina (Al_2O_3) is larger than that using silica (SiO_2) nanoparticle. This is because greater adhesion forces between sodium and the alumina (Al_2O_3) nanoparticle form larger compressed phase compared to those between sodium and the silica (SiO_2) nanoparticle. Fig. 42 and Fig. 43 present density plots and spatial distributions of atomic concentration of nanofluids.

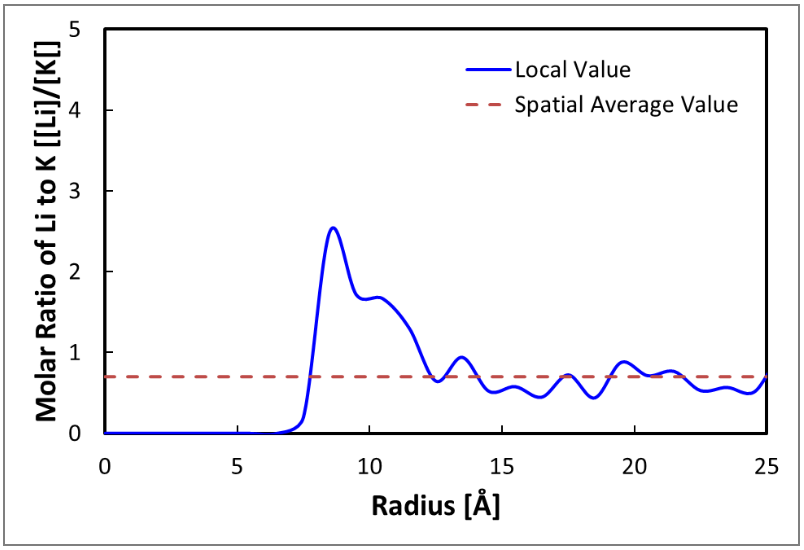

(a)

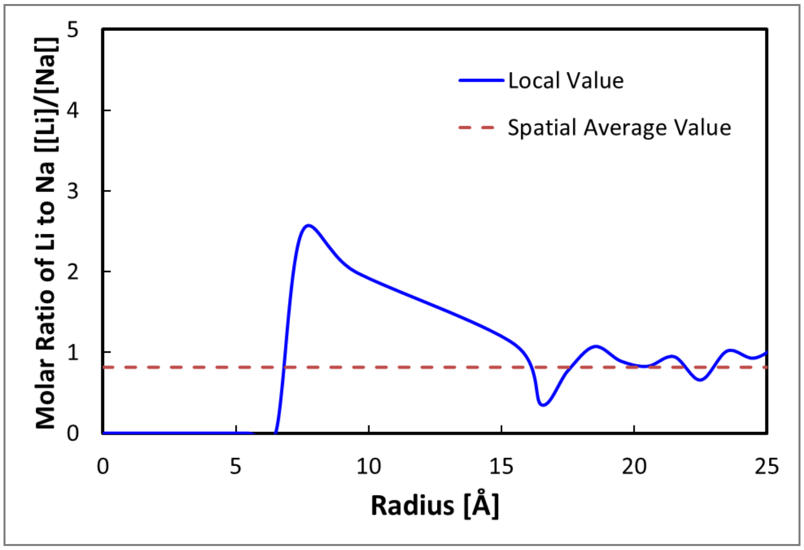

(b)

Fig. 40. Molar ratio distribution along the distance from the center of nanoparticle: (a) potassium nitrate and lithium nitrate mixture (KNO_3:$LiNO_3$ = 58.8:41.2 in molar ratio) (b) lithium nitrate and sodium nitrate mixture ($LiNO_3$:$NaNO_3$ = 45:55 in molar ratio).

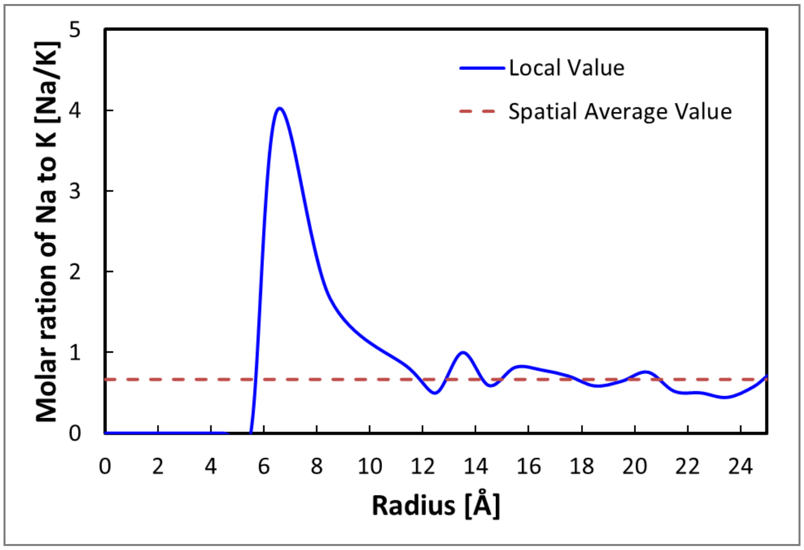

(a)

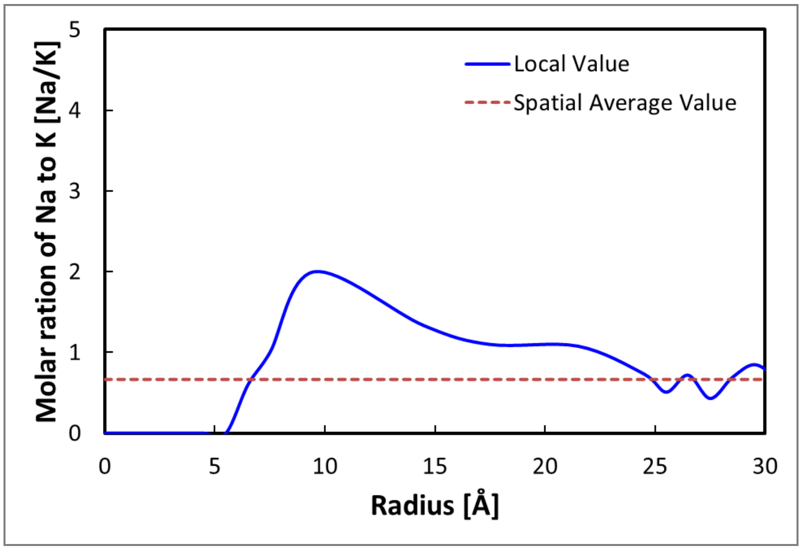

(b)

Fig. 41. Molar ratio distribution along the distance from the center of nanoparticle: (a) SiO_2 nanoparticle (b) Al_2O_3 nanoparticle.

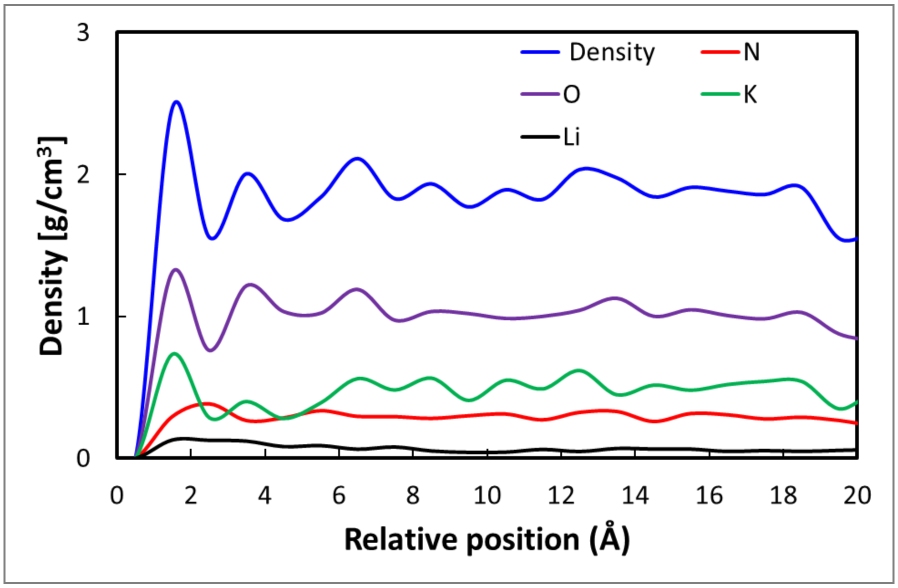

(a)

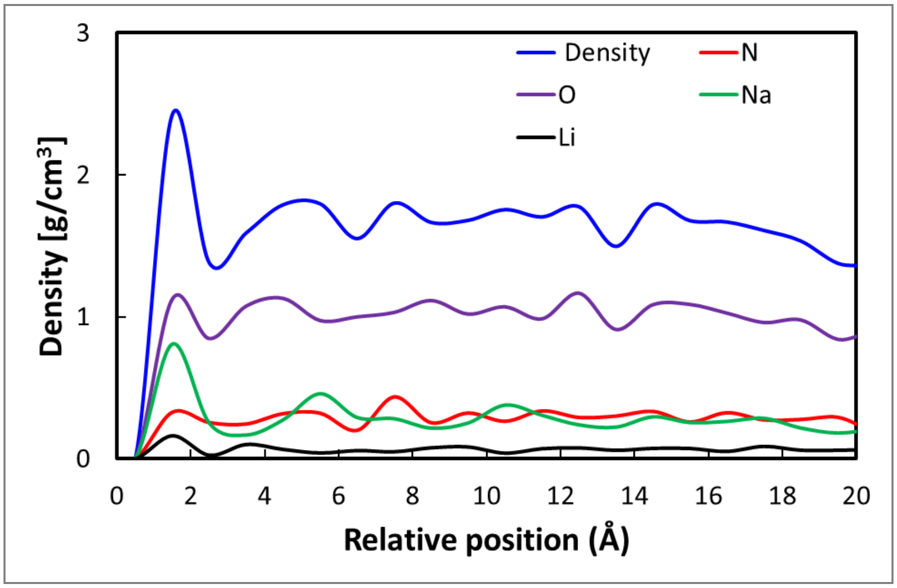

(b)

Fig. 42. Density plots and spatial distributions of atomic concentration of different elements of SiO_2 / nitrate salt mixture nanofluids: (a) potassium nitrate and lithium nitrate mixture (KNO_3:$LiNO_3$ = 58.8:41.2 in molar ratio) (b) lithium nitrate and sodium nitrate mixture ($LiNO_3$:$NaNO_3$ = 45:55 in molar ratio).

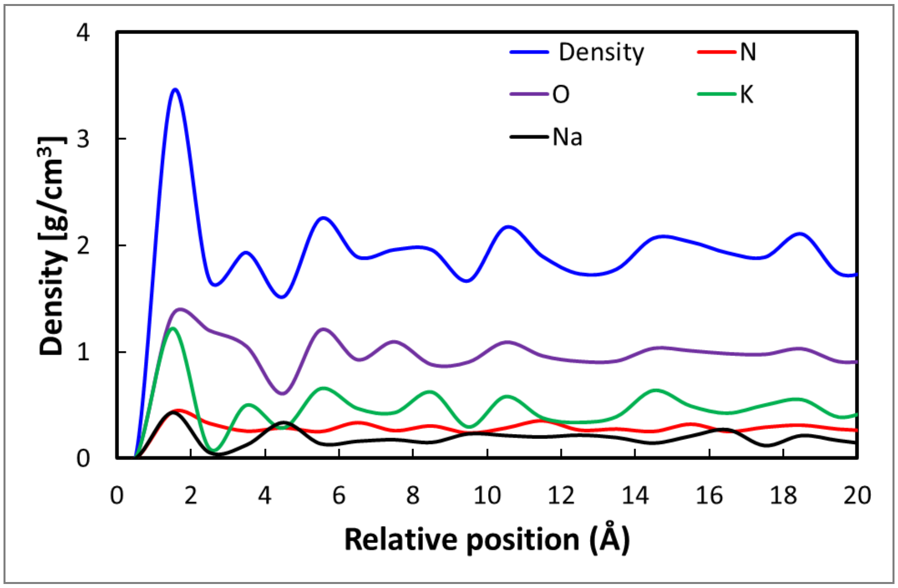

(a)

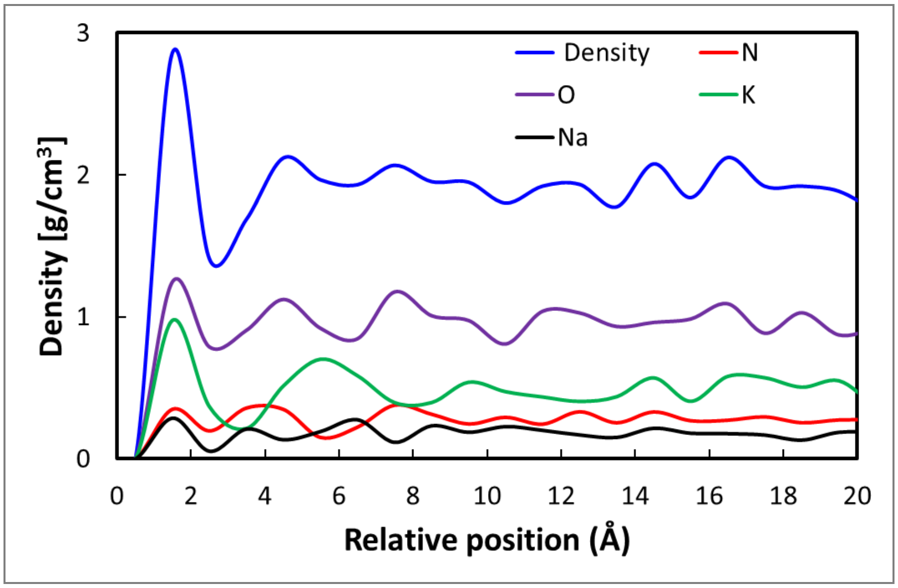

(b)

Fig. 43. Density plots and spatial distributions of atomic concentration of different elements of nitrate salt mixture (KNO_3:$NaNO_3$ = 60:40 in molar ratio) nanofluids: (a) SiO_2 nanoparticle (b) Al_2O_3 nanoparticle.

G. Viscosity Measurements of Silica (SiO_2)/Nitrate Nanofluids

For the calculation of the forced heat transfer coefficients for fluids from standard correlations in the literature - four basic thermo-physical properties of the test fluid are required: (1) viscosity, (2) density, (3) specific heat capacity, and (4) thermal conductivity. Dispersing nanoparticles in a liquid solvent has been reported to cause anomalous enhancements in the effective thermal conductivity as well as specific heat capacity (while density values are expected to remain unchanged for low mass concentrations of the nanoparticles). However, such property enhancements are accompanied by significant increase in viscosity [77]. This is often undesirable and can lead to degradation in the operational efficiencies of the thermal management platform or thermal energy storage (TES) device, depending on the mode of operation of such platforms/ devices. Any gain in heat transfer (coefficient) and hence reduction in component sizes (and weights) could be compromised by the requirements for dramatic increase in pumping power.

Therefore, development of a heat transfer fluid (HTF) or TES material requires a complex approach that accounts for the changes in all of the important thermo-physical properties (that are caused by the introduction of nanoparticles in to the fluid). Considering only the enhancement in the values of thermal conductivity, in isolation, do not convey the nuances and complexities of the interaction between different thermo-physical parameters. A global perspective that accounts for the changes in all the thermo-physical parameters for a test fluid is important for determining the efficacy (and changes in system thermodynamic efficiencies) for applications as novel HTF or TES materials. Thus, the challenge of nanofluid development is in understanding the complex (micro/ nano-scale and macro-scale) interactions between nanoparticles and fluid molecules as well as the resultant effect on the thermo-physical (as well as chemical) properties of the suspension (test fluid). It is obvious that these correlations depend on many factors, i.e., material properties of nanoparticles (which can be different compared to the bulk material properties), concentration, size and shape, properties of the base fluid (or neat solvent), and the presence of other materials (or contaminants at low concentrations) such as surfactants – which can affect the properties such as electrolyte strength, hydrogen bonding and pH of the solution (or the ionic liquid).

In this study, the effect of mass concentration of nanoparticles, temperature, and the imposed shear rate - on the rheological properties of a nanofluid was studied. The test fluids used in this study consisted of the liquid phase of the pure alkali-nitrate salt mixture and the liquid phase of the corresponding nanomaterial. The nanomaterial samples were synthesized by dispersing silica (SiO_2) nanoparticles.

1. Measurement Setup and Procedure

Silica (SiO_2) nanoparticles were procured from Alfa Aesar, as an aqueous stock solution with a mass concentration of 30%. The nominal size of the nanoparticles was ~10nm (according to manufacturer specification). The manufacturer reported that nitric acid was used to stabilize the colloidal solution.

Pure salt mixture composed of potassium nitrate and sodium nitrate (40:60 in molar ratio) was used as the solvent. The aqueous solution of the nanoparticle and the pure salt mixture were poured (or dispensed) into a glass bottle of 100mL volume. Distilled water was added to the solution in the bottle. For ensuring the stability of the dispersed nanoparticles, the pH value of the aqueous solution was fixed at pH 10 by titrating with NH_4OH solution. The solution was sonicated for 3 hours. The aqueous solution was then poured into a glass petri dish for fast evaporation. The petri dish was mounted on a hot plate set at 100℃ for evaporating the water – to obtain the powder samples of the synthesized nanomaterial. By following this synthesis protocol, samples of pure nitrate salt mixture and nanomaterial samples containing silica (SiO_2) nanoparticles at mass concentration of 0.5% and 1% were obtained. Fig. 44 shows the schematic for the synthesis protocol developed in this study. The nanomaterials were characterized using scanning electron microscopy (SEM), and the representative images are shown in Fig. 45.

The rheological properties of the nanofluids was measured using a rheometer (Model: AR2000, Manufacturer: TA Instruments), for imposed shear rates that was varied from $1s^{-1}$ to $1000s^{-1}$. The viscosity measurements were performed at reference temperatures of 300℃, 350℃, and 400℃. The measurements were repeated 3 times for each sample. The average values for these 3 measurements are reported in this study.

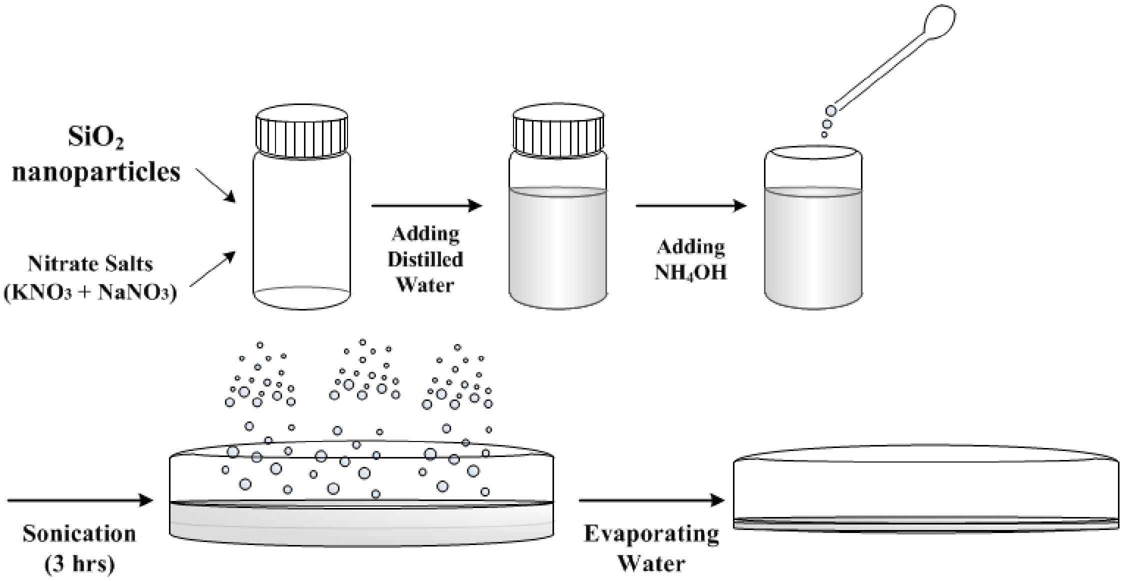

Fig. 44. Synthesis procedure of nitrate salt-based nanofluids with silica (SiO_2) nanoparticles.

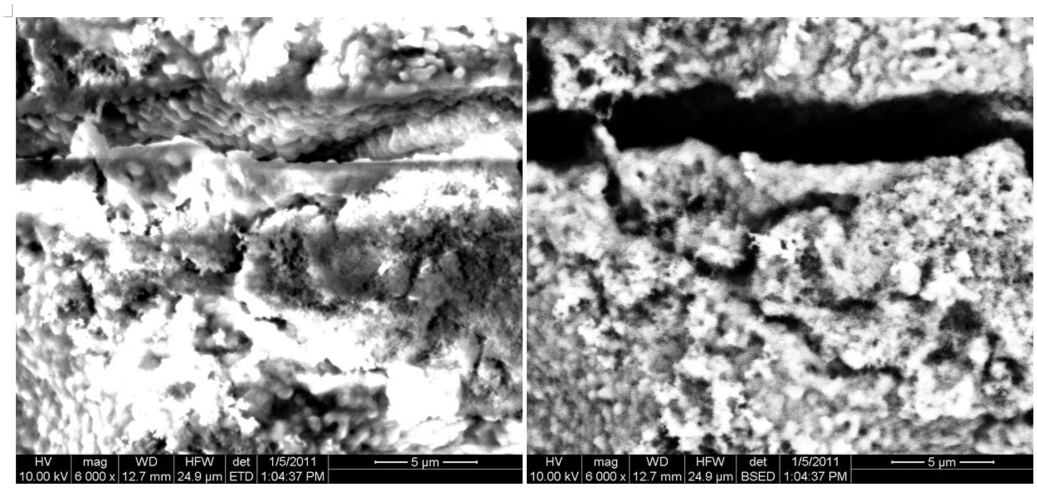

Fig. 45. SEM images of the potassium nitrate and sodium nitrate mixture (KNO_3:$NaNO_3$ = 40:60 in molar ratio) nanomaterials using silica (SiO_2) nanoparticles: (a) secondary electron image, (b) backscattered electron image.

2. Non-Newtonian Fluid Behavior

For an incompressible Newtonian fluid in laminar flow, the shear stress is equal to the product of the shear rate and the viscosity of the fluid. Pure molten salt are Newtonian fluids [78] because the viscosity (the ratio of shear stress to shear rate) is constant. However, Non-Newtonian fluid shows that flow curves (shear stress vs. shear rate) are non-linear or do not pass through the origin. This implies that viscosity is not constant at a given temperature and pressure. Non-Newtonian fluids can be grouped into three general classes:

(a) fluids for which the shear rate is determined only by the shear stress. These fluids are known as time independent, purely viscous, inelastic or generalized Newtonian fluids [78].

(b) fluids for which the relation between shear stress and shear rate depends on the duration of shearing and their kinematic history. These fluids are known as time-dependent fluids [78].

(c) fluids exhibiting characteristics of both ideal fluids and elastic solids and showing partial elastic recovery after deformation. These fluids are known as visco-elastic fluids [78].

The most common type of time independent non-Newtonian fluid behavior is shear-thinning. In this type, viscosity decreases with increasing shear rate. Mathematical model for shear-thinning behavior is typically described using the power-law model [78].

$$\tau_{yx} = m(\dot{\gamma}_{yx})^n \tag{III-6}$$

So the viscosity for the power-law fluid is given by:

$$\mu = \tau_{yx} / \dot{\gamma}_{yx} = m(\dot{\gamma}_{yx})^{n-1} \qquad \text{(III-7)}$$

For $n < 1$, the fluid exhibits shear-thinning properties

$n = 1$, the fluid shows Newtonian behavior

$n > 1$, the fluid shows shear-thickening behavior

In these equations, m and n are two empirical curve-fitting parameters.

Many materials exhibit visco-elastic behavior. They have some ability to store and recover shear energy. Generally, a fluid relaxation time (λ_f) is defined to quantify the visco-elastic behavior. When the rheological behavior of a material includes a transition from elastic to viscous as the time scale increases, one may define the relevant time scale as a relaxation time of the material. As the relaxation time of visco-elastic fluid increases, elastic behavior is increased. If the relaxation time is zero, the fluid shows perfectly viscous behavior without elastic behavior. It has been a common practice to describe visco-elastic fluid behavior in steady shear in terms of a shear stress (τ_{yx}) and the first normal stress difference (N_1); both of which are functions of shear rate. Leider and Bird (1972) [79] and Grimm (1978) [80] introduced definition of relaxation time (λ_f):

$$\lambda_f = \left(\frac{m_1}{2m} \right)^{1/(p_1 - n)} \qquad \text{(III-8)}$$

This definition is based on the assumption that both the first normal stress difference and shear rate can be approximated as power-law functions of shear rate in the range of condition of interest, that is,

$$N_1 = m_1 (\dot{\gamma}_{yx})^{p_1} \qquad \text{(III-9)}$$

and

$$\tau_{yx} = m(\dot{\gamma}_{yx})^n \tag{III-10}$$

3. Results and Discussions

Fig. 46 shows the rheological behavior of the pure molten salt and the nanofluids as a function of shear rate at 300 ℃, 350 ℃, and 400 ℃. It is observed that the pure molten salt demonstrates Newtonian behavior. A marginal enhancement in the viscosity values at higher shear rates was observed for the pure salt mixture – i.e., shear thickening behavior (non-Newtonian behavior) at higher shear rates, for all three temperatures selected in this study. The nanofluid samples demonstrate markedly shear thinning behavior (non-Newtonian behavior) for all three temperatures selected in this study. The viscosity values are more sensitive to the mass concentration of the nanoparticles at higher temperature (400℃) and lower shear rates, whereas at the lower temperatures the viscosity values are marginally enhanced with increase in mass concentration, especially at higher shear rates. Fig. 47 shows the rheological properties of the samples at different temperatures for a fixed value of mass concentration. For shear rates below 100s^{-1}, the effective viscosity increases with increasing temperature, while the trend is reversed when the shear rate exceeds 100s^{-1}. In Fig. 48 the viscosity values for the nanofluids are plotted as a function of temperature and mass concentration of the nanoparticles - for the shear rate of 1000s^{-1}. The figure shows dramatic enhancement in the viscosity values for lower mass concentrations with marginal enhancements in the viscosity as the mass fraction is increased. The viscosity values are enhanced linearly when plotted against the inverse of the temperature, showing dramatic decrease in viscosity with increase in temperature.

The viscosity values can be predicted using a correlation listed below [81]:

$$\ln\eta = A + B\times 1000/(T + C) \tag{III-11}$$

where η is the viscosity (mPa-s), T is the absolute temperature (K), while A, B and C are empirical constants. The empirical constants derived from the viscosity measurements in this study are listed in Table 30. If the measured viscosity values are normalized with respect to that of the neat solvent (for the same shear rates), the enhancement for the relative viscosity can be studied as a function of the mass fraction of the nanoparticles. For nanofluids containing nanoparticles at mass fraction of 0.5% and 1.0% the maximum enhancements in the viscosity values are 64.8% and 55.9% (at 673K), 51.6% and 67.7% (at 623K), 38.9% and 56% (at 573 K), respectively. Hence, the levels of enhancements are increased both with mass concentration and temperature.

The nanoparticle agglomeration can lead to significantly increase the viscosity of the nanofluids. The modified Krieger-Dougherty equation [82] suggested the prediction of viscosity of nanofluids including the effect of nanoparticle agglomeration. The relative viscosity of nanofluids (η_r) is expressed as:

$$\eta_r = \left[1 - \frac{\varphi_a}{\varphi_m}\right]^{-[\eta]\varphi_m} \tag{III-12}$$

The maximum concentration (φ_m) is assumed to be 0.605 at which the flow can occur. The effective volume concentration of aggregates (φ_a) is given by $\varphi_{a=}\ \varphi(a_a/a)^{3-D}$, with a_a and a, the effective radii of aggregates and nominal nanoparticles, respectively [83-84].

The term D is referred as the fractal index and a typical value is suggested to be 1.8 for nanofluids with spherical nanoparticles [81, 85]. The term φ indicates the actual volume concentration. In this study, the ratio of radii for the aggregates to that of the nominal nanoparticles (a_a/a) is assumed to be 20 and 32 for 1% and 0.5% mass concentration of nanoparticles, respectively. The intrinsic viscosity ($[\eta]$) is suggested to be 2.5 for monodisperse systems [85]. Fig. 49 shows the calculation results using the modified Krieger-Dougherty equation with experimental results. The results indicate that the nanoparticle agglomeration causes significant increase of viscosity of nanofluids. In addition, more nanoparticle agglomeration is observed at 0.5% mass concentration compared to 1% mass concentration due to the effective volume concentration of aggregates (φ_a).

From the experimental results of pure nitrate salt and nanomaterials, empirical parameters are acquired to apply to power law model and fluids are characterized whether these are Newtonian fluid or non-Newtonian fluid. Fig. 50 shows the shear stress as a function of shear rate with different temperature values. Empirical parameters indicate that pure molten salt is characterized as Newtonian fluid. However, Fig. 51 and Fig. 52 show the shear stress as a function of shear rate for each mass concentration. The results show that empirical parameters are less than 1. Hence, nanomaterials exhibit shear-thinning behavior. The smaller the value of n, the greater is the degree of shear-thinning.

To characterize the relaxation time for visco-elastic fluids, empirical parameters are acquired from the experimental results as shown in Fig. 53 and Fig. 54. Table 31 shows the empirical parameters and the relaxation time for each mass concentration with two temperature values. The results indicate that nanomaterials have the relaxation time of the order of micro-seconds (µsec). This implies that nanomaterial does not exhibit visco-elastic behavior. The results indicate that nanomaterial shows almost viscous response not elastic behavior.

4. Summary and Conclusions

The nanofluid samples are observed to demonstrate shear-thinning behavior. The rheological behavior of the nanofluids are more sensitive to temperature effects (than the effect of mass fraction) - with stronger shear thinning behavior being demonstrated at higher temperatures. For a given particle concentration, there exists a certain shear rate below which the viscosity increases with increasing temperature, whereas the reverse occurs above such a shear rate. The enhancement of viscosity at high shear rate ($1000s^{-1}$) ranges from 39% to 65% at 0.5% mass concentration and from 57% to 68% at 1% mass concentration. The SEM image of nanofluids shows significant agglomeration of the nanoparticles in the nitrate salt samples.

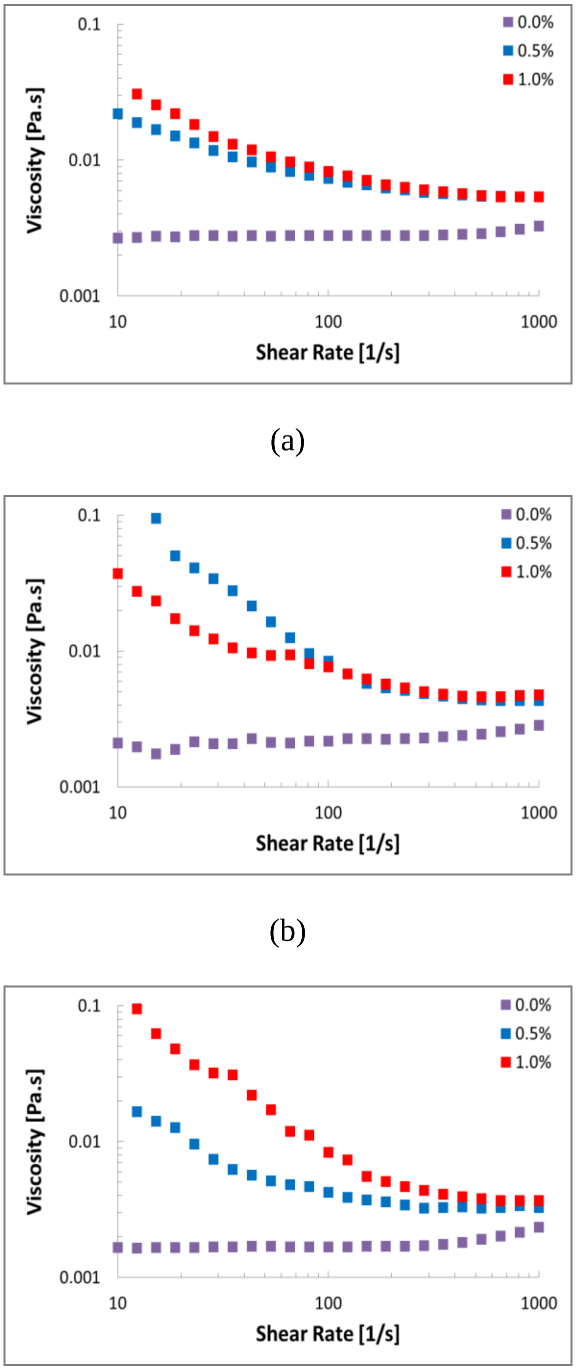

(a)

(b)

(c)

Fig. 46. Viscosity as a function of shear rate and mass concentration, for temperature of (a) 300℃, (b) 350℃, and (c) 400℃.

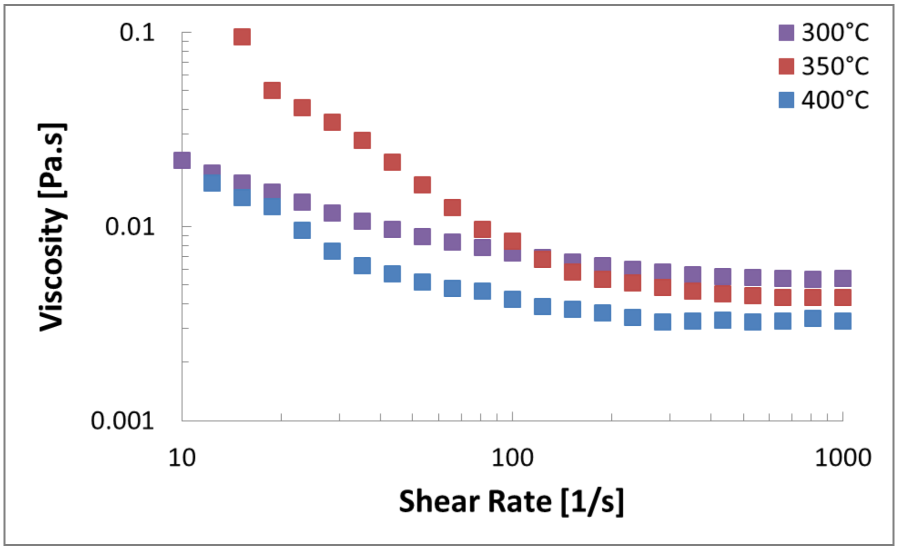

(a)

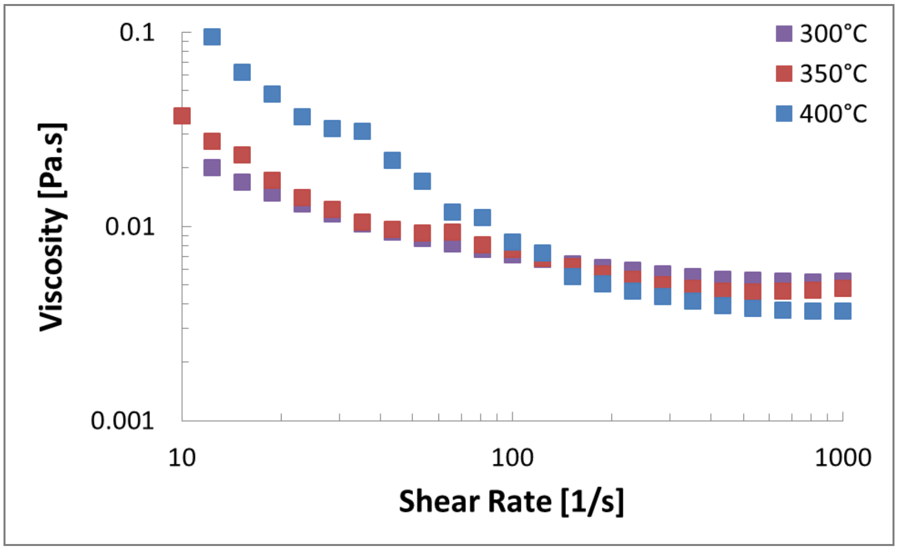

(b)

Fig. 47. Viscosity as a function of shear rate and temperature at mass concentration of (a) 0.5%, and (b) 1%.

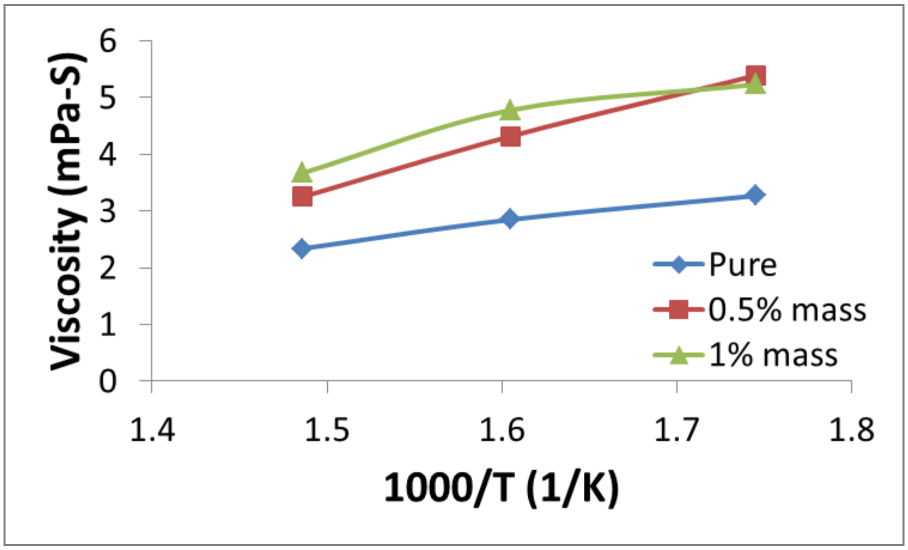

Fig. 48. Viscosity as a function of temperature and mass concentration of silica (SiO_2) nanoparticles for a shear rate of $1000 s^{-1}$.

Table 30. Empirical constants for Eq. (III-11).

Concentration (%)	A	B	C
0.0	1.957	0.255	-903.318
0.5	3.446	0.790	-1021.346
1.0	1.837	0.028	-724.665

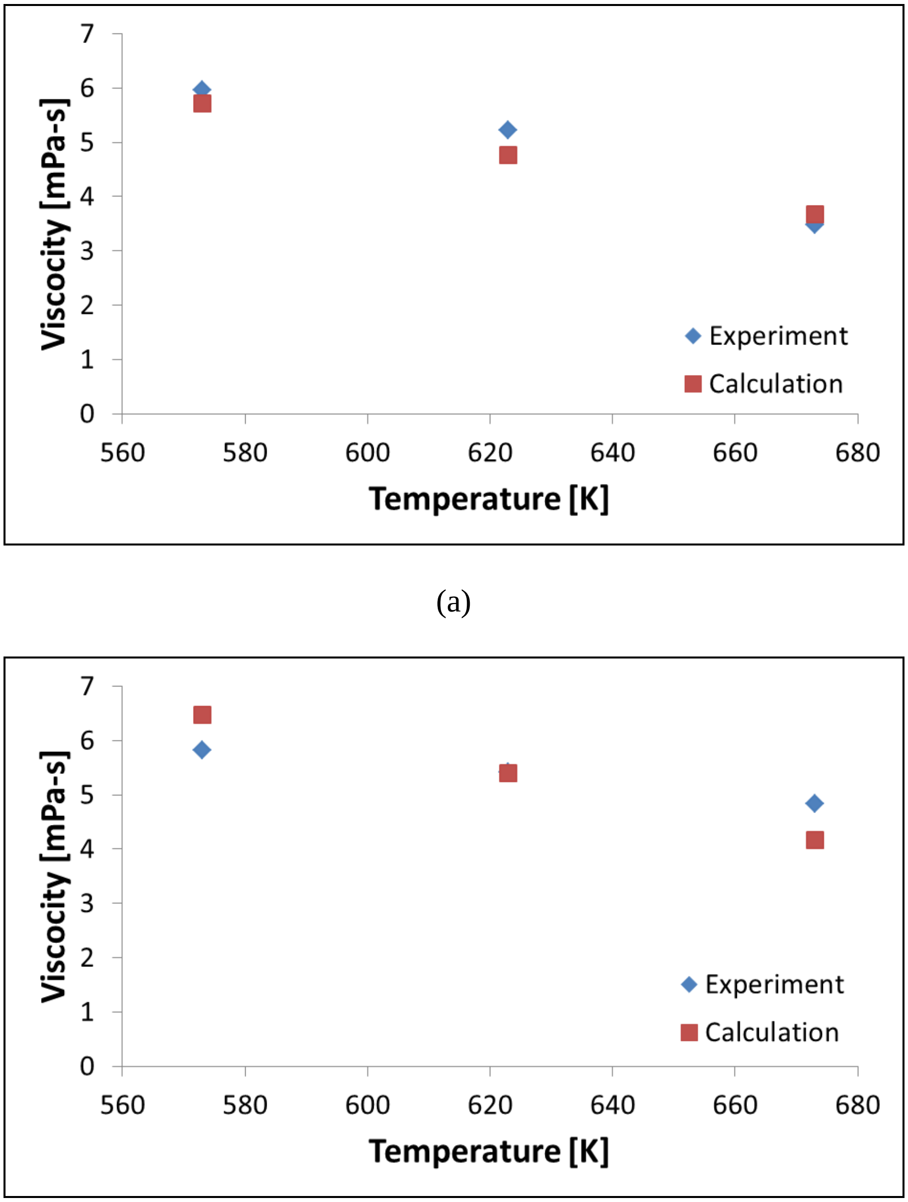

(a)

(b)

Fig. 49. Experimental and theoretical values of viscosity of the nanofluids at a shear rate of 1000 s^{-1} (a) 0.5% mass concentration (b) 1.0% mass concentration.

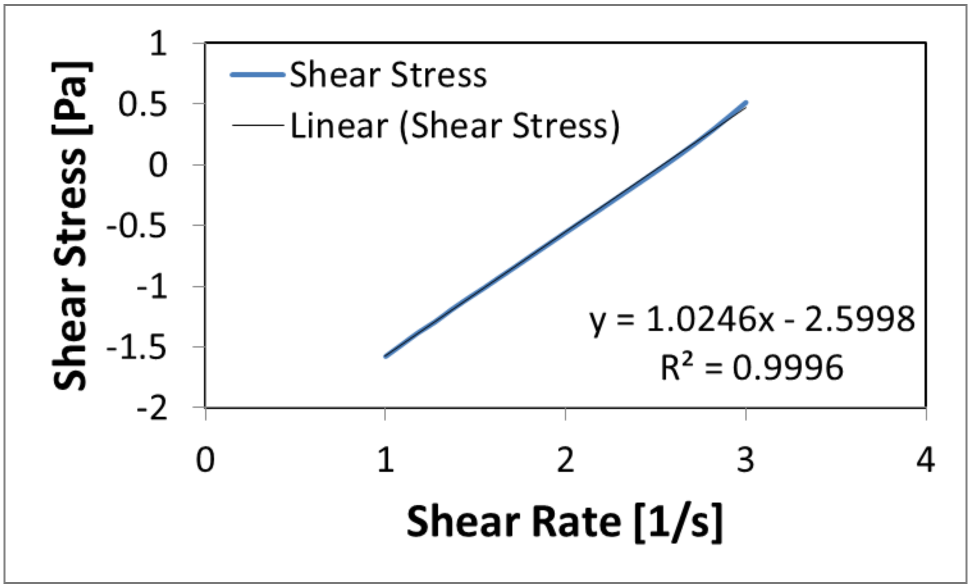

(a)

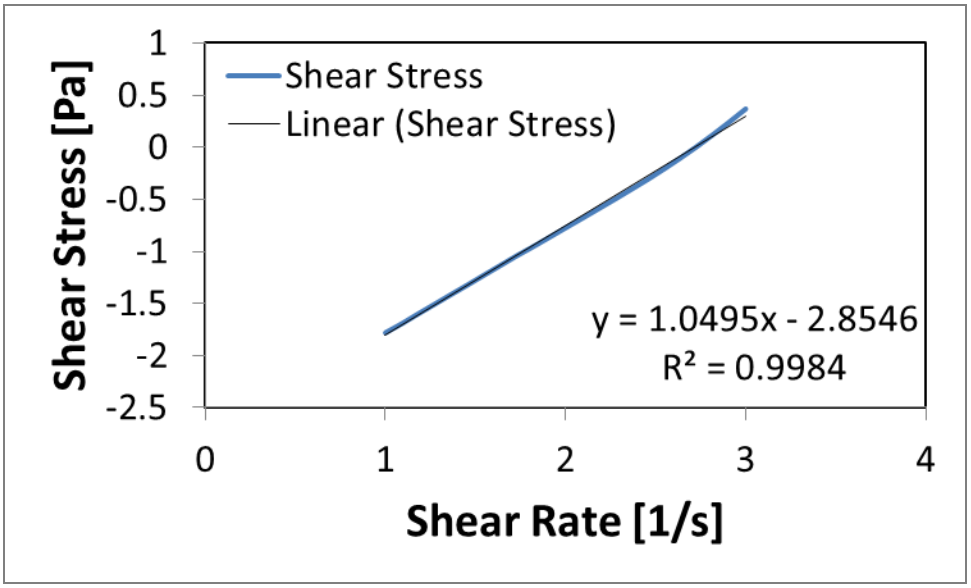

(b)

Fig. 50. Shear Stress for pure nitrate salt as a function of shear rate (log-log scale) (a) 300℃ and (b) 400℃.

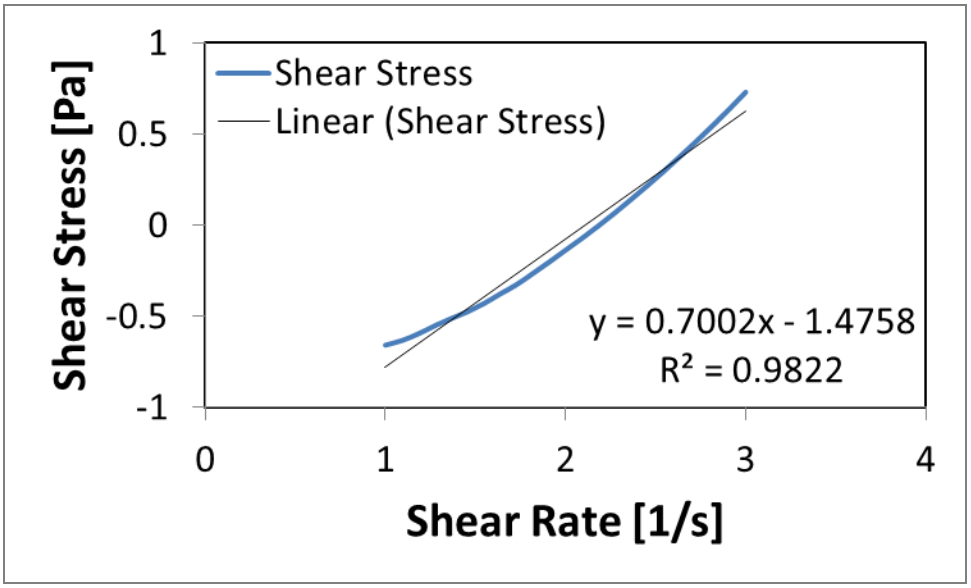

(a)

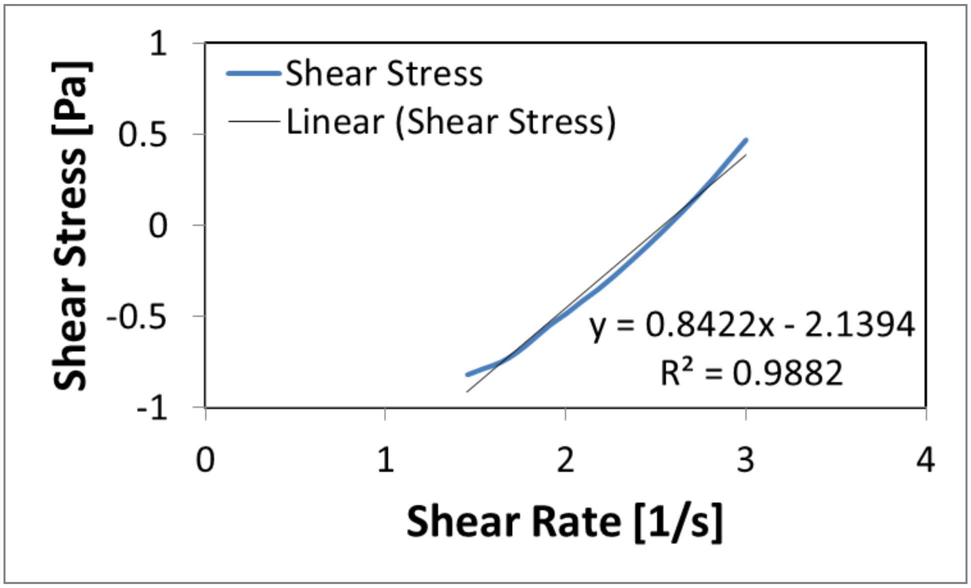

(b)

Fig. 51. Shear Stress for 0.5% mass concentration of nanomaterial as a function of shear rate (log-log scale) (a) 300℃ and (b) 400℃.

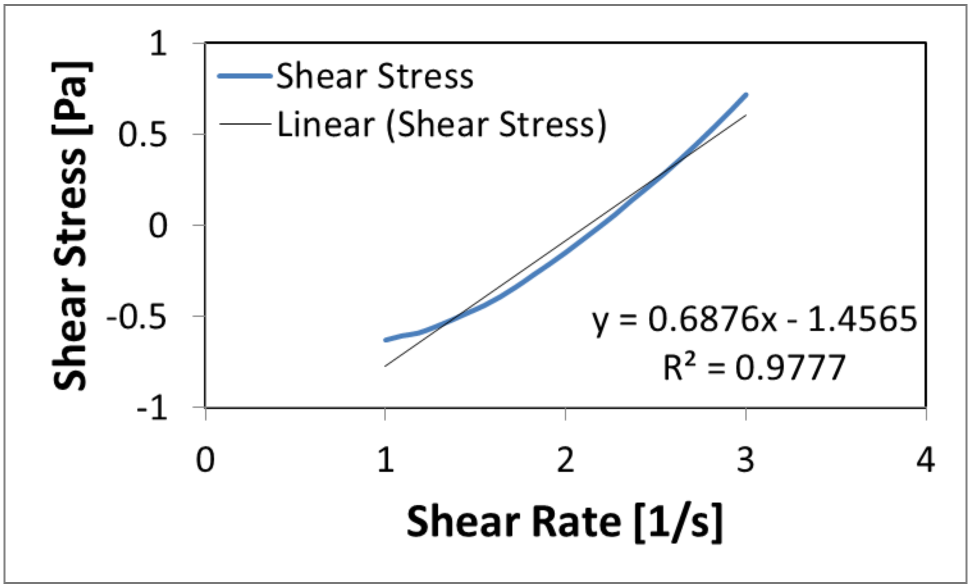

(a)

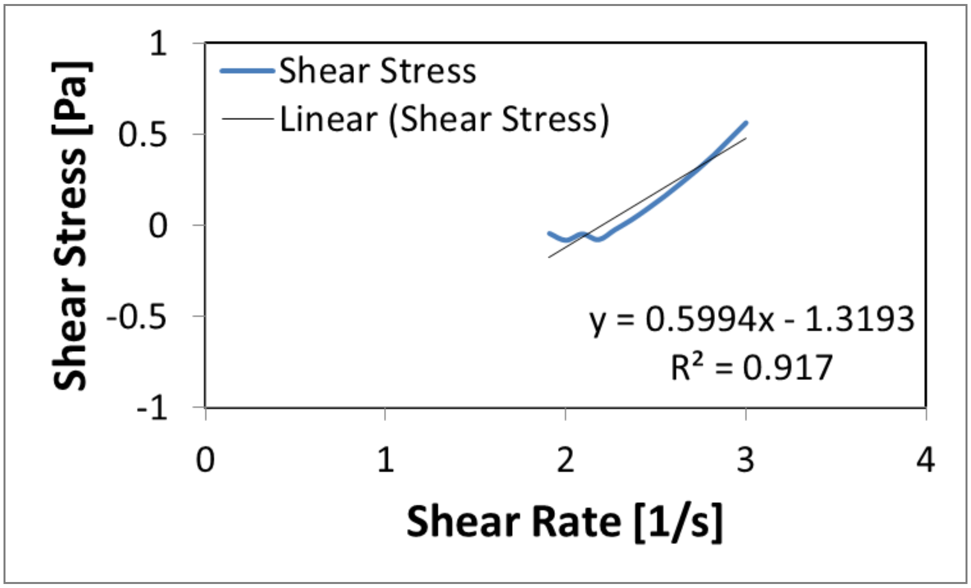

(b)

Fig. 52. Shear Stress for 1% mass concentration of nanomaterial as a function of shear rate (log-log scale) (a) 300℃ and (b) 400℃.

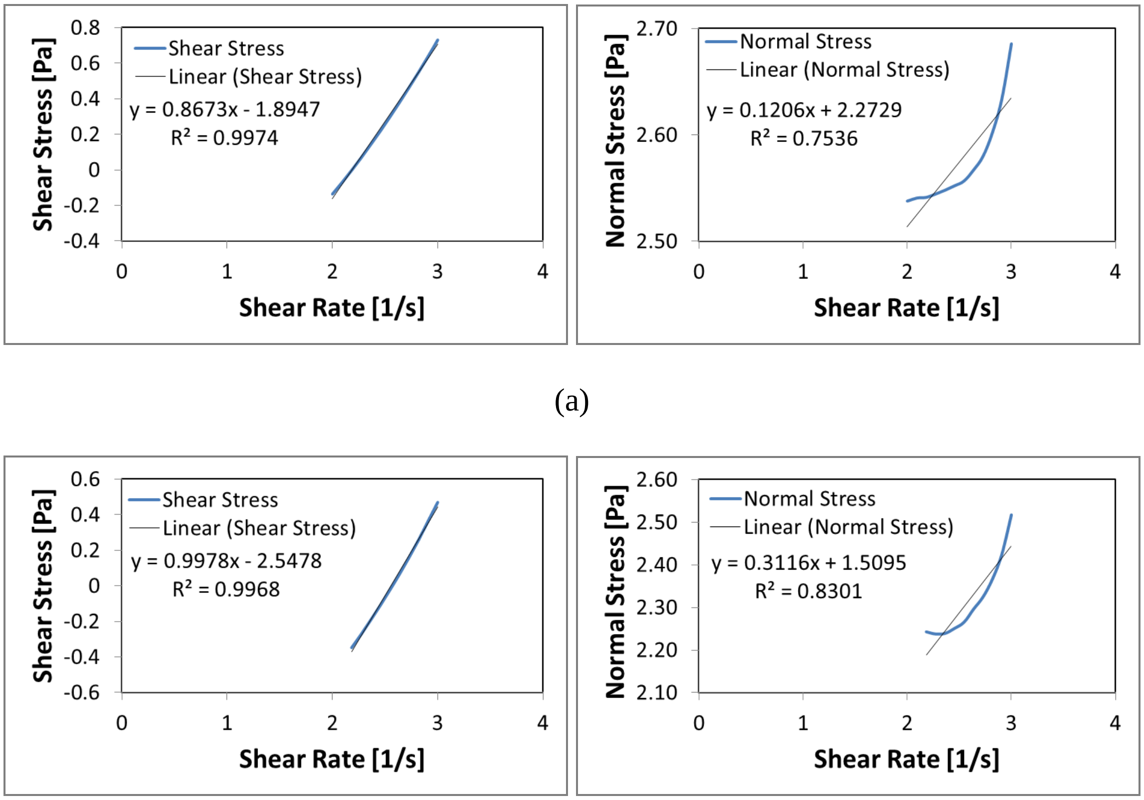

(a)

(b)

Fig. 53. Shear Stress and first normal stress difference for 0.5% mass concentration of nanomaterial as a function of shear rate (log-log scale) (a) 300℃ and (b) 400℃.

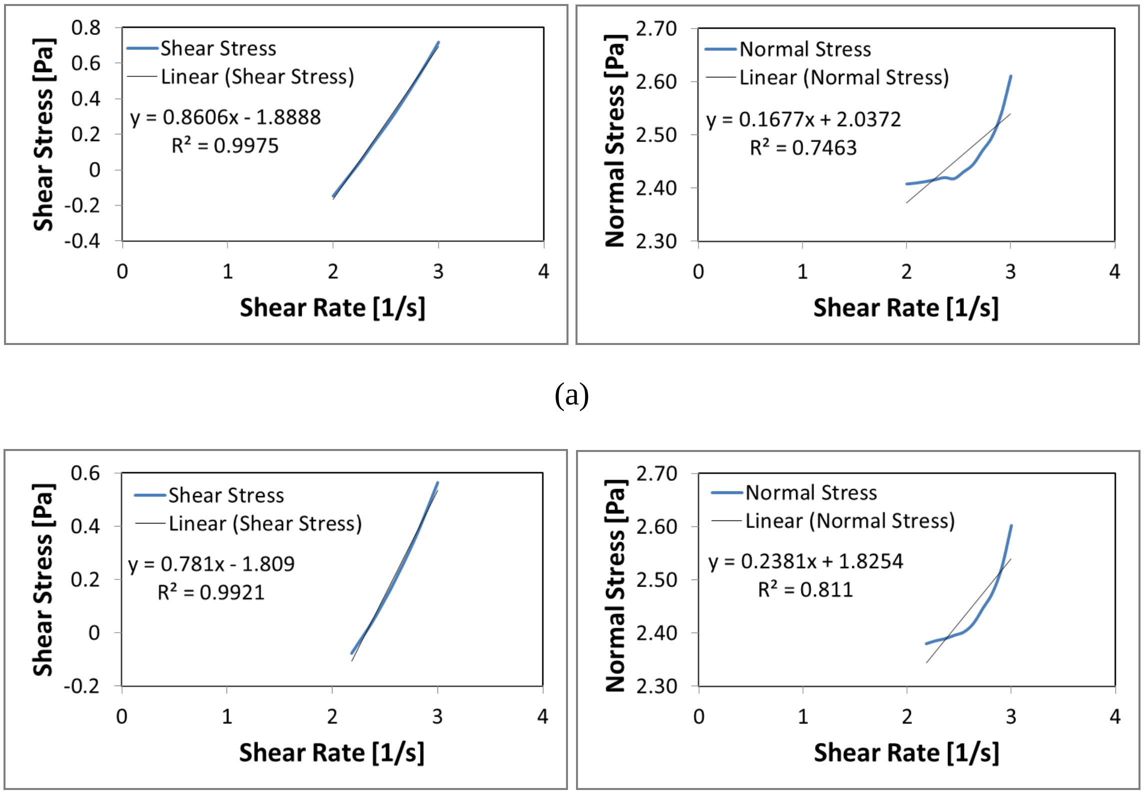

(a)

(b)

Fig. 54. Shear Stress and first normal stress difference for 1% mass concentration of nanomaterial as a function of shear rate (log-log scale) (a) 300℃ and (b) 400℃.

Table 31. Empirical parameters for power law and the relaxation time.

	0.5% 300℃	0.5% 400℃	1% 300℃	1% 400℃
p_1	0.1206	0.3116	0.1677	0.2381
m_1	187.4563	32.3221	108.9432	66.8960
n	0.8673	0.9978	0.8606	0.7810
m	0.0127	0.0028	0.0129	0.0155
λ_f [μsec]	6.63	3.36	5.87	0.73

CHAPTER IV

APPLICATIONS

In this chapter, some of the issues associated with the application of the nanomaterial samples for Thermal Energy Storage (TES) and Concentrating Solar Power (CSP) are explored. The contemporary commercial solar thermal systems are introduced and the advantages as well as disadvantages for each system are enumerated. As specific heat capacity of thermal energy storage (TES) material is enhanced, the “exergy” of the system is increased. Based on theories of thermodynamics, exergy of these systems are calculated. The increase of exergy can lead to reduction in the operating cost of CSP. However, when nanomaterials are used in Thermal Energy Storage (TES) and Concentrating Solar Power (CSP) systems, pumping cost is increased due to dramatic increase in viscosity. In addition, the stability of the nanoparticles in the thermal energy storage (TES) units should also be considered for operating their performance. These major barriers for applying these nanomaterials samples in practical applications are explored.

A. Commercial Solar Thermal Systems

The contemporary commercial solar thermal systems are categorized as: parabolic trough, central receiver (or solar tower), and parabolic dish [8]. Parabolic trough-shaped mirrors are used to focus solar thermal radiation on receiver tubes placed in the trough’s focal line. A heat transfer fluid, such as synthetic thermal oil, is circulated in these tubes. This fluid is then pumped through a series of heat exchangers to produce superheated steam. The steam is converted to electrical energy in a conventional steam turbine generator, which can either be part of a conventional steam cycle or integrated into a combined steam and gas turbine cycle. Highest single unit solar capacity of parabolic trough to date is 80MWe [8]. In solar tower systems (or central receiver), a circular array of heliostats (large individually tracking mirrors) is used to focus solar thermal radiation on a central receiver mounted at the top of a tower. A heat transfer fluid in this central receiver absorbs the highly concentrated solar thermal radiation reflected by the heliostats and converts it into thermal energy to be used for the subsequent generation of superheated steam for turbine operation. Highest single unit solar capacity of solar tower systems to date is 10MWe [8]. In parabolic dish systems, a parabolic dish-shaped reflector is used to focus solar thermal radiation on a receiver located at the focal point of the dish. The concentrated thermal radiation is absorbed into the receiver to heat a fluid or gas (air). This fluid or gas is then used to generate electricity in a small piston or Stirling engine or a micro turbine, attached to the receiver. Highest single unit solar capacity of parabolic dish systems to date is 25kWe [8].

Among these systems, parabolic dish systems have very high conversion efficiencies (peak solar to net electric conversion over 30%). However, the reliability of these systems needs to be improved.

Central receiver systems also provide high conversion efficiencies. However, projected annual performance values, investment and operating costs still need to be accounted properly to determine their viability in commercial operation.

Parabolic trough systems are commercially operational and have been operated over long-term durations - generating over 12billion kWh power. The average annual net plant efficiency of 14% has been demonstrated commercially while investment and operating costs have been accounted for – for the long-term deployment and operation in commercial systems [8]. In addition, parabolic trough power plants with hot and cold tanks for thermal energy storage (TES), provide a cheap and economical way to store the harvested solar thermal energy. Hence, parabolic trough is considered to be commercially the most optimized system to date.

If the thermo-physical properties of the materials utilized in these systems are enhanced, the potential for extracting work (which is known as "exergy") can be increased for a fixed amount of energy input (i.e., insolation) and the operating cost can be reduced. Normalized costs for thermal energy storage (TES) – which can be derived using the NREL Excelergy model (which was utilized in the study by Malik [19]) - was predicted to be decreased with enhancement of specific heat capacity of TES material. Based on thermodynamic analysis, the change in exergy due to incorporation of nanomaterials - is explored next.

B. Exery

When a new energy source (such as a wind, solar energy, geothermal, and biomass) is considered for commercial exploitation, the exergy of the system can be analyzed to obtain an estimate for the cost-benefit analyses [86].

In this study, exergy is estimated for nanomaterials that can be used in thermal energy storage (TES). For performing the thermodynamic analysis, the thermal energy storage unit is considered to be a closed system (since no mass crosses the system boundary). To estimate the maximum limit for the operating characteristics, the system is assumed to operate using reversible cycles. The reversible work is calculated by considering a series of imaginary reversible heat engines that can be assumed to operate between the source and the sink (as shown in Fig. 55).

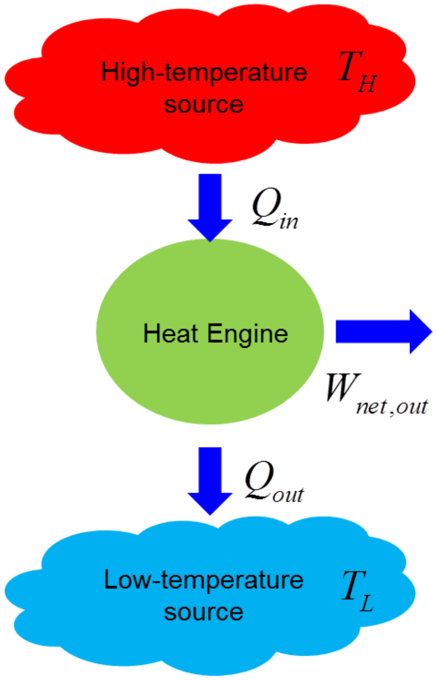

Fig. 55. For performing the thermodynamic analyses of TES - a series of imaginary reversible heat engines are assumed to operate between the source and the sink.

The work output is expressed as:

$$\mathrm{W}_{rev} = \eta_{th,rev} Q_{in} = \left(1 - \frac{T_{\mathrm{sink}}}{T_{Source}}\right) Q_{in} = \left(1 - \frac{T_0}{T}\right) Q_{in} \qquad \text{(IV-1)}$$

The source temperature (T_H) is assumed to change from T_0 to T_1 during the process. If the energy balance is applied on the thermal energy storage, the equation is expressed as:

$$\underbrace{E_{in} - E_{out}}_{\substack{\text{Net energy transfer} \\ \text{byheat,work,and mass}}} = \underbrace{\Delta E_{system}}_{\substack{\text{Change in internal, kinetic,} \\ \text{potential, etc., energies}}}$$

$$Q_{in,\text{heat engine}} = Q_{out,\text{system}} = -mc_{avg} \Delta T \qquad \text{(IV-2)}$$

$$-Q_{out} = \Delta U = mc_{avg} \Delta T$$

where, heat transfer from the thermal energy storage material to the heat engines is equal in magnitude and opposite in direction. Substituting and performing the integration, the reversible work is determined to be:

$$\mathrm{W}_{rev} = \left(1 - \frac{T_0}{T}\right)\left(mc_{avg} \Delta T\right)$$

$$\mathrm{W}_{rev} = \int_{T_0}^{T_1} \left(1 - \frac{T_0}{T}\right)\left(mc_{avg} dT\right) = mc_{avg} \left((T_1 - T_0) - T_0 \ln \frac{T_1}{T_0}\right) \qquad \text{(IV-3)}$$

The specific heat value is obtained from experimental measurements for the nanomaterial samples. Hence, work potential (exergy) due to incorporation of nanomaterials increases since the specific heat capacity is enhanced.

During a transient process for heat addition to the nanomaterials, the exergy of the system changes and is dependent on the rate of energy input as well as the rate of change of temperature of the system. Hence, differentiating Eq. (IV-3) with time (t), the following expression is obtained:

$$\frac{dW_{rev}(t)}{dt} = mc_{avg}\frac{dT_1(t)}{dt}\left(1 - \frac{T_0}{T_1(t)}\right) \qquad \text{(IV-4)}$$

For a fixed heating rate (or fixed rate of temperature change), nanomaterials provide higher rates of work output owing to the enhanced values of specific heat capacity for the molten salt nanofluids. On the other hand, if the rate of temperature increase ($dT_1(t)/dt$) into the nanomaterial is higher owing to their higher thermal conductivity values, concomitantly the rate of exergy gain is also higher. In addition, the term ($1-T_0/T_1(t)$) in eq. (IV-4) affects the rate of exergy increase. If the heating rate is faster, the fraction ($T_0/T_1(t)$) is smaller and the value of their terms within the brackets, i.e., ($1-T_0/T_1(t)$), is larger. Hence, the exergy in the transient processes are also enhanced due to incorporation of nanomaterials.

C. Major Barriers to Applications

Nanomaterials (nanofluids and nanocomposites) have been reported to cause anomalous enhancements in the effective thermal conductivity as well as specific heat capacity. However, nanofluids are accompanied by significant increase in viscosity. This is often undesirable and can lead to degradation in the operational efficiencies of concentrating solar power (CSP) plant or thermal energy storage (TES) device. Hence, to maximize the effect of nanoparticles in the solvent material (enhancing thermal properties and minimizing the increase of viscosity), viscosity of nanofluids should be thoroughly investigated for the whole operating temperature range, mass concentration of nanoparticles, and required mass flows of the heat transfer material in the system. In addition, suitable synthesis techniques should be explored in order to obtain stable nanomaterials that will ensure long-term operational reliability for these materials.

Hence, in order to apply these nanomaterials to commercial systems, the stability of the nanoparticles in solvent material should be considered. Additional equipment may be needed to ensure uniform dispersion of nanoparticles. For example, a stirring system (for mechanical dispersion) can be operated in the commercial thermal energy storage (TES) units.

CHAPTER V

SUMMARY, CONCLUSIONS AND FUTURE DIRECTIONS

In this study, theoretical analyses (analytical and computational) as well as experimental measurements were performed for exploring the effect of various parameters on the thermo-physical properties of inorganic nanomaterials. The motivation of this study was to explore the applicability of these nanomaterials for concentrating solar power (CSP) stations, especially for Thermal Energy Storage (TES) devices.

A simple analytical model was developed for calculating the total specific heat capacity of nanomaterials as a function of the nanoparticle mass concentration and nanoparticle diameter, as well as by considering the contribution from the compressed phase enveloping the nanoparticle. The analytical model enables the development of selection criteria for enhancing the effective specific heat capacity of the nanomaterials. For spherical nanoparticles smaller than 5-6nm diameter, the contribution from the compressed phase is more pronounced in augmenting or reducing the total specific heat capacity values for a given solvent material.

Molecular dynamics (MD) simulations were also performed for calculating the interfacial thermal resistance of various nanomaterials. The results indicate that the inorganic materials containing oxide nanoparticles have the lowest values for the interfacial thermal resistance. Carbonate-based nanomaterial with SWCNT has lower value of Kapitza resistance compared to that of nitrate-based nanomaterials containing

SWCNT. Based on the analytical model for the specific heat capacity of nanofluids and MD simulation results for interfacial thermal resistance of nitrate salt-based nanofluids, oxide nanoparticles are expected to provide the most optimal formulation for enhancing thermal conductivity as well as specific heat capacity of nitrate salt-based nanomaterials.

In the experimental investigations, the specific heat capacity values of nitrate salt-based nanomaterials with mica nanoparticles was enhanced by 13-15% in solid phase and 13-19% in liquid phase compared to that of the pure nitrate salt mixture (KNO_3:$NaNO_3$ = 60:40 in molar ratio), that was used as the solvent. The primary reason for the specific heat capacity enhancement is assumed to be due to the compressed phase of the solvent molecules at solid-liquid interface on the nanoparticles. The evidence for this hypothesis is that from the experimental results - the specific heat capacity values in solid phase of the samples undergoing phase change were observed to be enhanced by 10% compared to that of the samples that are not subjected to phase change. The predictions for the specific heat capacity of nanomaterials obtained from the simple analytical model (incorporating the effect of compressed phase) are in good agreement with the experimental results. The results from the analytical model also imply that the well-dispersed nanoparticles enable higher enhancement of the specific heat capacity values compared to nanomaterials containing agglomerated nanoparticle. This trend is also observed for measurements of nitrate salt-based nanomaterials with alumina (Al_2O_3) nanoparticles. The agglomerated nanomaterial samples did not show any enhancement of the specific heat capacity due to marginal contribution from the compressed phase at the solid-liquid interface. The specific heat capacity values of nitrate salt-based nanomaterials with silica (SiO_2) nanoparticles are enhanced by up to 18% in the solid phase and by up to 23% in the liquid phase at 2% mass concentration of the nanoparticles. In the case of nanomaterials with titania (TiO_2) nanoparticles, the specific heat capacity values are enhanced up to 18% in solid phase and up to 25% in liquid phase at 2% mass concentration.

The measurement of viscosity of nanofluids with silica (SiO_2) nanoparticles shows shear-thinning behavior. More pronounced shear thinning behavior is observed at higher operating temperatures. For a given particle concentration, there exists a certain threshold shear rate below which the viscosity increases with increasing temperature, whereas the behavior reverses at shear rates exceeding the threshold value. SEM image of nanofluids showed agglomerated nanoparticles in the nitrate salt. This can be a dominant factor for the anomalous rheological behavior observed in these experiments.

In conclusion, the compressed phase at solid-liquid interface in nanomaterials affects the thermo-fluidic properties of nanomaterials. To maximize the effect of the compressed phase, spherical nanoparticles smaller than 5-6nm diameter should be dispersed in liquid phase and these individual nanoparticles should be well dispersed in the liquid solvent. In addition, any enhancements in thermal properties (specific heat capacity or thermal conductivity) should be qualified by considering the associated enhancement in the rheological properties (e.g., anomalous increase in viscosity). The operational efficiencies for particular application (e.g., CSP/ TES, thermal management, etc.) depend on the mode of operation and the level of enhancement in the rheological properties. For example, in power tower configurations of the CSP stations the effect of viscosity enhancement is likely to be marginal compared to that of parabolic trough configurations in CSP stations.

The following tasks are suggested for future investigations (as an outcome from this study):

(a) Viscosity of nanofluids should be thoroughly investigated for the operating temperature range, mass concentration of nanoparticles, and required mass flow of the heat transfer material in the system.

(b) Stability and dispersion methods should be explored to obtain stable nanomaterials (to ensure long-term reliability for commercial applications as well as to enhance thermal properties and reduce viscosity).

Finally, the major contributions from this study and the pioneering approaches explored in this study are summarized below:

(a) A simple analytical model was developed for estimating the specific heat capacity of nanomaterials. Based on this model, a few criteria were identified for enhancing the specific heat capacity of the nanomaterial samples.

(b) Appropriate nanoparticle materials that can be doped in nitrate salt mixture were predicted using MD simulations (i.e., by utilizing the effect of interfacial thermal resistance) for enhancing thermal performance in heat transfer applications.

(c) The existence of the compressed phase was demonstrated conclusively in the thermo-cycling experiments - by the measurements of specific heat capacity enhancement in solid phase for nanomaterial samples that were subjected to phase change – in comparison to nanomaterial samples which did not undergo phase-change.

(d) The results of the experiments and computational studies show that for silica nanoparticles – the optimum size range of 5–10 nanometer diameter is conducive for enhancing both the specific heat capacity and thermal conductivity (i.e., by reducing the thermal interfacial resistance). For other materials, the optimal size range of nanoparticles for enhancing specific heat capacity (of the mixture) is smaller than the optimal size range of nanoparticles for enhancing the thermal conductivity of the mixture.

REFERENCES

[1] Wang, X. and Majumdar, A.S., 2007, “Heat Transfer Characteristics of Nanofluids: A Review,” Int. J. Thermal Sciences, **46**, pp. 1–19.

[2] Keblinski, P., Eastman, J.A., and Cahill, D.G., 2005, “Nanofluids for Thermal Transport,” Mater. Today, **8**, pp. 36-44.

[3] Eastman, J.A., Phillpot, S.R., Choi, S.U.S., and Keblinski, P., 2004, “Thermal Transport in Nanofluids,” Annu. Rev. Mater. Res., **34**, pp. 219–246.

[4] Das, S.K., Choi, S.U.S., and Patel, H.E., 2006, “Heat Transfer in Nanofluids – A Review,” Heat Transfer Eng., **27**, pp. 3–19.

[5] Yu, W., France, D.M., Routbort, J.L., and Choi, S.U.S., 2008, “Review and Comparison of Nanofluid Thermal Conductivity and Heat Transfer Enhancements,” Heat Transfer Eng., **29**(5), pp. 432–460.

[6] Ajayan, P.M., Schadler, L.S., and Braun, P.V., 2003, “Nanocomposite Science and Technology,” John Wiley & Sons, Inc., Hoboken, NJ, USA.

[7] Kearney, D., Herrmann, U., Nava, P., Kelly, B., Mahoney, R., and Pacheco, J., 2003, “Assessment of a Molten Salt Heat Transfer Fluid in a Parabolic Trough Solar Field,” J. Sol. Energy Eng., **125**(2), pp. 170-176.

[8] Brakmann, G., Aringhoff, R., Geyer, M., and Teske, S., 2005, “Concentrated Solar Thermal Power- Now,” Greenpeace International, Amsterdam, The Netherlands.

[9] Philibert, C., 2010, “Technology Roadmap: Concentrating Solar Power,” International Energy Agency, Paris Cedex, France.

[10] Betts, M., 2011, “The Effects of Nanoparticle Augmentation of Nitrate Thermal Storage Materials for Use in Concentrating Solar Power Applications,” MS Thesis, Texas A&M University, College Station, TX, USA.

[11] Buongiorno, J., 2006, “Convective Transport in Nanofluids,” J. Heat Transfer, **128**(3), pp. 240-250.

[12] Das, S.K., Choi, S.U.S., Yu, W., and Pradeep, T., 2010, “Nanofluids: Science and Technology,” John Wiley & Sons, Inc., Hoboken, NJ, USA.

[13] KaKac, S. and Pramuanjaroenkij, A., 2009, “Review of Convective Heat Transfer Enhancement with Nanofluids,” Int. J. Heat Mass Transfer, **52**, pp. 3187-3196.

[14] Li, L., Zhang, Y., Ma, H., and Yang, M., 2010, “Molecular Dynamics Simulation of Effect of Liquid Layering around the Nanoparticle on the Enhanced Thermal Conductivity of Nanofluids,” J. Nanopart. Res., **12**, pp. 811-821.

[15] Shin, D. and Banerjee, D., 2009, “Investigation of Nanofluids for Solar Thermal Energy Storage Applications,” ASME Energy Sustainability Conference, Paper No. ES2009-90465.

[16] Shin, D. and Banerjee, D., 2010, “Effects of Silica Nanoparticles on Enhancing the Specific Heat Capacity of Carbonate Salt Eutectic (work in progress),” Int. J. Structural Changes in Solids-Mechanics and Appl., **2**(2), pp. 25-31.

[17] Shin, D. and Banerjee, D., 2011, “Enhanced Specific Heat of Silica Nanofluid,” J. Heat Transfer, **133**(2), pp. 024501 (1-4).

[18] Shin, D. and Banerjee, D., 2011, "Enhancement of Specific Heat Capacity of High-temperature Silica-nanofluids Synthesized in Alkali Chloride Salt Eutectics for Solar Thermal-energy Storage Applications," Int. J. Heat Mass Transfer, **54**, pp. 1064-1070.

[19] Malik, D.R., 2010, "Evaluation of Composite Alumina Nanoparticle and Nitrate Eutectic Materials for Use in Concentrating Solar Power Plants," MS Thesis, Texas A&M University, College Station, TX, USA.

[20] Incropera, F.P., Dewitt, D.P., Bergman, T.L., and Lavine, D.S., 2006, "Fundamentals of Heat and Mass Transfer, 6th edition," John Wiley & Sons, Inc., Hoboken, NJ, USA.

[21] Wen, D., Lin, G., Vafaei, S., and Zhnag, K., 2009, "Review of Nanofluids for Heat Transfer Applications," Particuology, **7**, pp. 141-150.

[22] Buongiorno, J., Venerus, D.C., Prabhat, N., Mckrell, T., Townsend, J., and others, 2009, "A Benchmark Study on the Thermal Conductivity of Nanofluids," J. Appl. Phys., **106**, pp. 094312 (1-14).

[23] Vajjha, R.S. and Das, D.K., 2009, "Specific Heat Measurement of Three Nanofluids and Development of New Correlations," Int. J. Heat Mass Transfer, **131**, pp. 071601(1-7).

[24] Zhou, S. and Ni, R., 2008, "Measurement of Specific Heat Capacity of Water Based Al_2O_3 Nanofluid," Appl. Phys. Lett., **92**, pp. 093123 (1-3).

[25] Namburu, P.K., Kulkarni, D.P., Dandekar, A., and Das, D.K., 2007, “Experimental Investigation of Viscosity and Specific Heat of Silicon Dioxide Nanofluids,” Micro Nano Lett., **2**, pp. 67-71.

[26] Xuan, Y. and Roetzel, W., 2000, “Conceptions for Heat Transfer Correlation of Nanofluids,” Int. J. Heat Mass Transfer, **43**, pp. 3701-3707.

[27] Pak, B.C. and Cho, Y.I., 1998, “Hydrodynamic and Heat Transfer Study of Dispersed Fluids with Submicron Metallic Oxide Nanoparticles,” Exp. Heat Transfer, **11**, pp. 151-170.

[28] Nelson, I.C., Banerjee, D., and Ponnappan, R., 2009, “Flow Loop Experiments Using Polyalphaolefin Nanofluids,” J. Thermophys. Heat Transfer, **23**, pp. 752-761.

[29] Wang, B., Zhou, L., and Peng, X, 2006, “Surface and Size Effects on the Specific Heat of Nanoparticles,” Int. J. Thermophys, **27**, pp. 139–151.

[30] Wang, L., Tan, Z., Meng, S., Druzhinina, A., Varushchenko, R.A., and Li, G., 2001, “Heat Capacity Enhancement and Thermodynamic Properties of Nanostructured Amorphous SiO_2,” J. Non-Cryst. Solids, **296**, pp. 139-142.

[31] Prasher, R., Bhattacharya, P., and Phelan, P.E., 2006, “Brownian-Motion-based Convective-conductive Model for the Effective Thermal Conductivity of Nanofluids,” J. Heat Transfer, **128**, pp. 588-595.

[32] Oh, S.H., Kgoldffmann, Y., Scheu, C., Kaplan, W.D., and Rühle, M., 2005, “Ordered Liquid Aluminum at the Interface with Sapphire,” Sci., **310**, pp. 661-663.

[33] Gerardi, C., Cory, D., Buongiorno, J., Hu, L., and McKrell, T., 2009, “Nuclear Magnetic Resonance-based Study of Ordered Layering on the Surface of Alumina Nanoparticles in Water,” Appl. Phys. Lett., **95**, pp. 253104 (1-3).

[34] Ocko, B.M., Hlaing, H., Jepsen, P.N., Kewalramani, S., Tkachenko, A., Pontoni, D., Reichert, H., and Deutsch, M., 2011, “Unifying Interfacial Self-assembly and Surface Freezing,” Phys. Rev. Lett., **106**, pp. 137801 (1-4).

[35] Feibelman, P.J., 2010, “The First Wetting Layer on a Solid,” Phys. Today, **63**, pp. 34-39.

[36] Beskok, A., Karniadakis, G., and Aluru, N., 2005, “Microflows and Nanoflows: Fundamentals and Simulation (Interdisciplinary Applied Mathematics),” Springer, New York, NY, USA.

[37] Singh, N., 2010, “Computational Analysis of Thermo-fluidic Performance of a Nano-fin,” Ph.D Dissertation, Texas A&M University, College Station, TX, USA.

[38] Yu, W. and Choi, S.U.S., 2003, “The Role of Interfacial Layers in the Enhanced Thermal Conductivity of Nanofluids: A Renovated Maxwell Model,” J. Nanopart. Res., **5**, pp. 167-171.

[39] Xie, H., Fujii, M., and Zhang, X., 2005, “Effect of Interfacial Nanolayer on the Effective Thermal Conductivity of Nanoparticle-fluid Mixture,” Int. J. Heat Mass Transfer, **48**, pp. 2926–2932.

[40] Yu, C.J., Richter, A.G., Datta, A., Durbin, M.K., and Dutta, P., 2000, “Molecular Layering in a Liquid on a Solid Substrate: An X-ray Reflectivity Study,” Physica B, **283**, pp. 27–31.

[41] Xue, L., Keblinski, P., Phillpot, S.R., Choi, S.U.S., and Eastman, J.A., 2004, “Effect of Liquid Layering at the Liquid–solid Interface on Thermal Transport,” Int. J. Heat Mass Transfer, **47**, pp. 4277–4284.

[42] Yu, W. and Choi, S.U.S., 2004, “The Role of Interfacial Layers in the Enhanced Thermal Conductivity of Nanofluids: A Renovated Hamilton-Crosser Model,” J. Nanopart. Res., **6**, pp. 355-361.

[43] Lee, S., Choi, S.U.S., Li, S., and Eastman, J.A., 1999, “Measuring Thermal Conductivity of Fluids Containing Oxide Nanoparticles,” J. Heat Transfer, **121**, pp. 280–289.

[44] Tan, Z., Wang, L., and Shi, Q., 2009, “Study of Heat Capacity Enhancement in Some Nanostructured Materials,” Pure Appl. Chem., **81**, pp. 1871-1880.

[45] Ditmars, D.A., Ishihara, S., Chang, S.S., and Bernstein, G., 1982, “Enthalpy and Heat Capacity Standard Reference Material: Synthetic Sapphire (α-Al_2O_3) from 10 to 2250K,” J. Res. Natl. Bur. Stand., **87**, pp. 159-163.

[46] Buyco, E.H. and Davis, F.E., 1970, “Specific Heat of Aluminum from Zero to Its Melting Temperature and Beyond Equation for Representation of the Specific Heat of Solids,” J. Chem. Eng. Data, **15**, pp. 518-523.

[47] Araki, N., Matsuura, M., Makino, A., Hirata, T., and Kato, Y., 1988, “Measurement of Thermophysical Properties of Molten Salt: Mixtures of Alkaline Carbonate Salt,” Int. J. Thermophys., **9**, pp. 1071-1080.

[48] Chang, C., Lee, W., Young, T., Ju, S., Chang, C., Chen, H., and Chang, J., 2008, “Adsorption Mechanism of Water Molecules Surrounding Au Nanoparticles of Different Sizes,” J. Chem. Phys., **128**, pp. 154703(1-9).

[49] Sarkar, S. and Selvam, P.R., 2007, “Molecular Dynamics Simulation of Effective Thermal Conductivity and Study of Enhanced Thermal Transport Mechanism in Nanofluids,” J. Appl. Phys., **102**, pp. 074302(1-7).

[50] Assael, M.J., Kakosimos, K., Banish, M.R., Brillo, J., Egry, I., Brooks, R., Quested, P.N., Mills, K.C., Nagashima, A., Sato, Y., and Wakeham, W.A., 2006, “Reference Data for the Density and Viscosity of Liquid Aluminum and Liquid Iron,” J. Phys. Chem. Ref. Data, **35**, pp. 285-300.

[51] Swiler, T.P. and Loehman, R.E., 2000, “Molecular Dynamics Simulations of Reactive Wetting in Metal-ceramic Systems,” Acta. mater., **48**, pp. 4419-4424.

[52] Dobbs, E.R. and Jones, G.O., 1957, “Theory and Properties of Solid Argon,” Rep. Prog. Phys., **20**, pp. 516-565.

[53] Figgins, B.F., 1960, “The Specific Heat of Solid Argon and an Equimolar Argon-Krypton Mixture,” Proc. Phys. Soc., **76**, pp. 732-736.

[54] Bergman, T.L., 2009, “Effect of Reduced Specific Heats of Nanofluids on Single Phase, Laminar Internal Forced Convection,” Int. J. Heat Mass Transfer, **52**, pp. 1240-1244.

[55] Ahn, H.S., Sinha, N., Zhang, M., Banerjee, D., Fang, S., and Baughman, R.H., 2006, “Pool Boiling Experiments on Multiwalled Carbon Nanotube (MWCNT) Forests," J. Heat Transfer, **128**, pp. 1335(1-8).

[56] Sathyamurthi, V., Ahn, H.S., Banerjee, D., and Lau, S.C., 2009, “Subcooled Pool Boiling Experiments on Horizontal Heaters Coated with Carbon Nanotubes,” J. Heat Transfer, **131**, pp. 071501(1-10).

[57] Sriraman, S.R., 2007, “Pool Boiling on Nano-fined Surfaces," MS Thesis, Texas A&M University, College Station, TX, USA.

[58] Ding, Y., Alias, H., Wen, D., and Williams, R.A., 2006, “Heat Transfer of Aqueous Suspensions of Carbon Nanotubes (CNT nanofluids)," Int. J. Heat Mass Transfer, **49**, pp. 240-250.

[59] Kim, S.J., Bang, I.C., Buongiorno, J., and Hu, L.W., 2007, “Study of Pool Boiling and Critical Heat Flux Enhancement in Nanofluids," Bull. Pol. Acad. Sci., **55**, pp. 211-216.

[60] Jackson, J.E., Borgmeyer, B.V., Wilson, C.A., and Cheng, P., 2006, “Characteristics of Nucleate Boiling with Gold Nanoparticles in Water,” Proceedings of the IMECE2006, Paper No. IMECE2006-16020.

[61] Shanks, H.R., Maycock, P.D., Sidles, P.H., and Danielson, G.C., 1963, “Thermal Conductivity of Silicon from 300 to 1400K,” Phys. Rev., **130**, pp. 1743-1748.

[62] Kim, P., Shi, L., Majumdar, A., and McEuen, P.L., 2001, “Thermal Transport Measurements of Individual Multiwalled Nanotubes," Phys. Rev. Lett., **87**, pp. 215502(1-4).

[63] Berber, S., Kwon, Y., and Tomanek, D., 2000, “Unusually High Thermal Conductivity of Carbon Nanotubes," Phys. Rev. Lett., **84**, pp. 4613-4616.

[64] Turanov, A.N. and Tolmachev, Y.V., 2009, "Heat- and Mass-transport in Aqueous Silica Nanofluids," Heat Mass Transfer, **45**, pp. 1583-1588.

[65] Lu, G., Li, Y., Sun, W., and Li, C., 2007, "Molecular Dynamics Simulation of Hydration Structure of KNO_3 Electrolyte Solution," Chin. J. Chem. Phys., **20**, pp. 22-30.

[66] Megyes, T., Balint, S., Peter, E., Grosz, T., Bako, I., Krienke, H., and Bellissent-Funel, M.C., 2009, "Solution Structure of $NaNO_3$ in Water: Diffraction and Molecular Dynamics Simulation Study," J. Phys. Chem. B, **113**, pp. 4054–4064.

[67] Jayaraman, S., Thompson, A.P., Anatole von Lilienfeld, O., and Maginn, E.J., 2010, "Molecular Simulation of the Thermal and Transport Properties of Three Alkali Nitrate Salt," Ind. Eng. Chem. Res., **49**, pp. 559–571.

[68] Gutierrez, G., Belonoshko, A.B., Ahuja, R., and Johansson, B., 2000, "Structural Properties of Liquid Al_2O_3: A Molecular Dynamics Study," Phys. Rev. E, **61**, pp. 2723-2729.

[69] Walther, J.H., Jaffe, R., Halicioglu, T., and Koumoutsakos, P., 2000, "Molecular Dynamics Simulations of Carbon Nanotubes in Water," Proceedings of the Summer Program 2000 – Center for Turbulence Research, pp. 5-20.

[70] Huxtable, S.T., Cahill, D.G., Shenogin, S., Xue, L., Ozisik, R., Barone, P., Usrey, M., Strano, M.S., Siddons, G., Shim, M., and Keblinski, P., 2003, "Interfacial Heat Flow in Carbon Nanotube Suspensions," Nat. Mater., **2**, pp. 731-734.

[71] Hasselman, D.P.H. and Johnson, L.F., 1987, “Effective Thermal Conductivity of Composites with Interfacial Thermal Barrier Resistance,” J. Compos. Mater, **21**, pp. 508-515.

[72] Plimption, S., 1995, “Fast Parallel Algorithms for Short-range Molecular Dynamics,” J. Comp. Phys., **117**, pp. 1-19.

[73] Janz, G.J., Allen, C.B., and Bansal, N.P., 1979, “Physical Properties Data Complications Relevant to Energy Storage-2. Molten Salt: Data on Single and Multi-component Salt Systems,” National Bureau of Standards, National Standard Reference Data Series, **61**, pp. 396-411.

[74] Jung, S. and Banerjee, D., 2011, “Enhancement of Heat Capacity of Nitrate Salts Using Mica Nanoparticles, in Developments in Strategic Materials and Computational Design II: Ceramic Engineering and Science Proceedings, Volume 32,” John Wiley & Sons, Inc., Hoboken, NJ, USA.

[75] Jones, D.E.G., Brousseau, P., Fouchard, R.C., Turcotte, A.M., and Kwok, Q.S.M., 2000, “Thermal Characterization of Passivated Nanometer Size Aluminium Powders”, J. Therm. Anal. Calorim., **61**, pp. 805-818.

[76] Kline, S.J. and McClintock, F.A., 1953, “Describing Uncertainties in Single Sample Experiments,” Mech. Eng., **75**, pp. 3-8.

[77] Murshed, S.M.S., Leong, K, and Yang, C., 2008, “Investigations of Thermal Conductivity and Viscosity of Nanofluids,” Int. J. Therm. Sci., **47**, pp. 560-568.

[78] Chhabra, R.B. and Richardson, J.F., 2008, "Non-Newtonian Flow and Applied Rheology-engineering Applications, 2nd Edition," Butterworth-Heinemann, Burlington, MA, USA.

[79] Leider, P.J. and Bird, R.B., 1974, "Squeezing Flow between Parallel Disks. II. Experimental Results," Ind. Eng. Chem. Fund., **13**, pp. 342-346.

[80] Grimm, R.J., 1978, "Squeezing Flows of Polymeric Liquids," AlChE J., **24**, pp. 427-439.

[81] Chen, H., Ding, Y., Lapkin, A., and Fan, X., 2009, "Rheological Behaviour of Ethylene Glycol-titanate Nanotube Nanofluids," J. Nanopart. Res., **11**, pp. 1513–1520.

[82] Krieger, I.M. and Dougherty, T.J., 1959, "A Mechanism for Non-Newtonian Flow in Suspensions of Rigid Spheres," Trans. Soc. Rheol., **3**, pp. 137-152.

[83] Wang, B., Zhou, L., and Peng, X., 2003, "A Fractal Model for Predicting the Effective Thermal Conductivity of Liquid with Suspension of Nanoparticles," Int. J. Heat Mass Transfer, **46**, pp. 2665-2672.

[84] Hui, P.M. and Stroud, D., 1986, "Complex Dielectric Response of Metal-Particle Clusters," Phys. Rev. B, **33**, pp. 2163-2169.

[85] Chen, H., Ding, Y., and He, Y., Tan, C., 2007, "Rheological Behaviour of Ethylene Glycol Based Titania Nanofluids," Chem. Phys. Lett., **444**, pp. 333-337.

[86] Cengel, Y.A. and Boles, M.A., 2006, "Thermodynamics: An Engineering Approach, 5th Edition," McGrawHill, New York, NY, USA.

[87] Jung, S., Jo, B., Shin, D., and Banerjee, D., 2010, “Experimental Validation of a Simple Analytical Model for Specific Heat Capacity of Aqueous Nanofluids,” Proceedings of 2010 SAE Power Systems Conference, Paper No. 2010-01-1731.

[88] Jung, S. and Banerjee, D., 2011, “A Simple Analytical Model for Specific Heat of Nanofluid with Tube Shaped and Disc Shaped Nanoparticles,” Proceedings of The ASME/JSME 2011 8th Thermal Engineering Joint Conference, Paper No. AJTEC2011-44372.

[89] Laurent, Ch., Flahaut, E., and Peigney, A., 2010, “The Weight and Density of Carbon Nanotubes versus the Number of Walls and Diameter,” Carbon, **48**, pp. 2989-2999.

[90] Hepplestone, S.P., Ciavarella, A.M., Janke, C., and Srivastava, G.P., 2006, “Size and Temperature Dependence of the Specific Heat Capacity of Carbon Nanotubes,” Surf. Sci., **600**, pp. 3633-3636.

[91] Hone, J., Llaguno, M.C., Biercuk, M.J., Johnson, A.T., Batlogg, B., Benes, Z., and Fischer, J.E., 2002, “Thermal Properties of Carbon Nanotubes and Nanotube-based Materials,” Appl. Phys. A, **74**, pp. 339-343.

APPENDIX

A. Experimental Validation of a Simple Analytical Model for Specific Heat Capacity of Aqueous Nanofluids [87]

Table 32. The thermo-physical property values (of the pure water, the compressed phase, and the nanoparticles) as well as the thickness of the compressed phase and the void space [87].*

Nanofluids	ρ_n (g/cm^3)	ρ_s (g/cm^3)	C_n (J/g-K)	C_s (J/g-K)	C_l (J/g-K)	d_{sl} (nm)	δ (nm)
Alumina/Water	3.97	0.92	1.06	2.04	4.187	0.3	1
Titania/Water	4.157	0.92	0.75	2.04	4.187	0.3	1
Silica/ Water	2.65	0.92	1.35	2.04	4.187	0.3	1

---

[*] Adopted from “Experimental Validation of a Simple Analytical Model for Specific Heat Capacity of Aqueous Nanofluids” by Jung, S., Jo, B., Shin, D., and Banerjee, D., 2010, *SAE Power Systems Conference*, Page Number 2010-01-1731, Copyright 2010 by SAE Copyright Administrator.

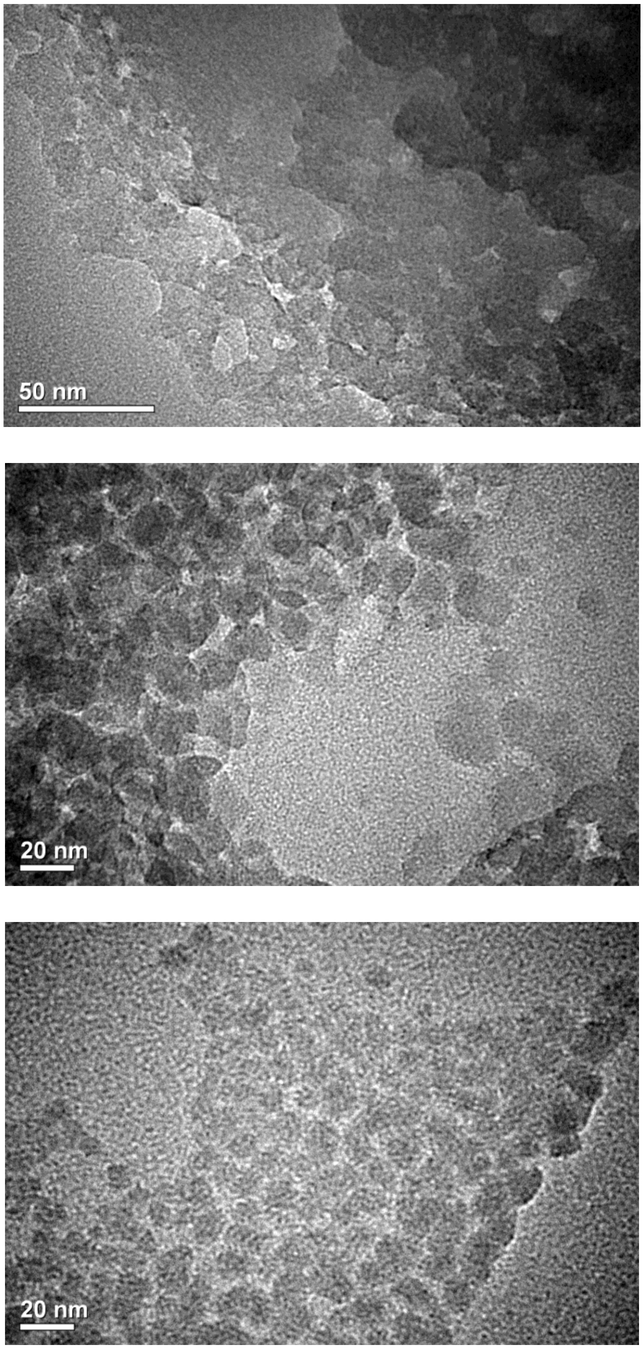

Fig. 56. Transmission Electron Microscopy (TEM) images of SiO_2 nanoparticles with a nominal diameter of 4 nm (top), 10 nm (middle), and 20 nm (bottom) [87].[*]

---

[*] Adopted from “Experimental Validation of a Simple Analytical Model for Specific Heat Capacity of Aqueous Nanofluids” by Jung, S., Jo, B., Shin, D., and Banerjee, D., 2010, *SAE Power Systems Conference*, Page Number 2010-01-1731, Copyright 2010 by SAE Copyright Administrator.

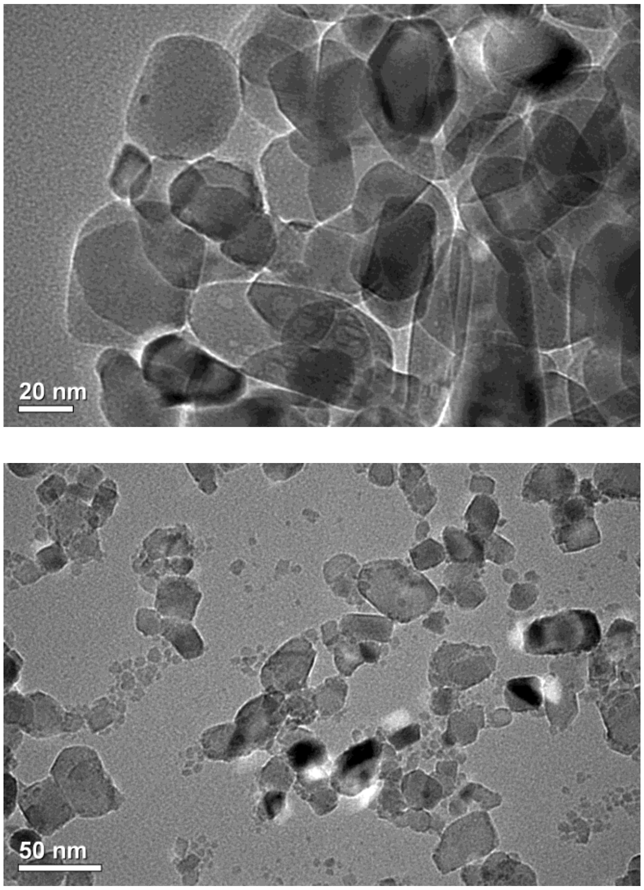

Fig. 57. Transmission Electron Microscopy (TEM) images of TiO_2 nanoparticles with a nominal diameter of 20 nm (top) and 50 nm (bottom) [87].[*]

---

[*] Adopted from “Experimental Validation of a Simple Analytical Model for Specific Heat Capacity of Aqueous Nanofluids” by Jung, S., Jo, B., Shin, D., and Banerjee, D., 2010, *SAE Power Systems Conference*, Page Number 2010-01-1731, Copyright 2010 by SAE Copyright Administrator.

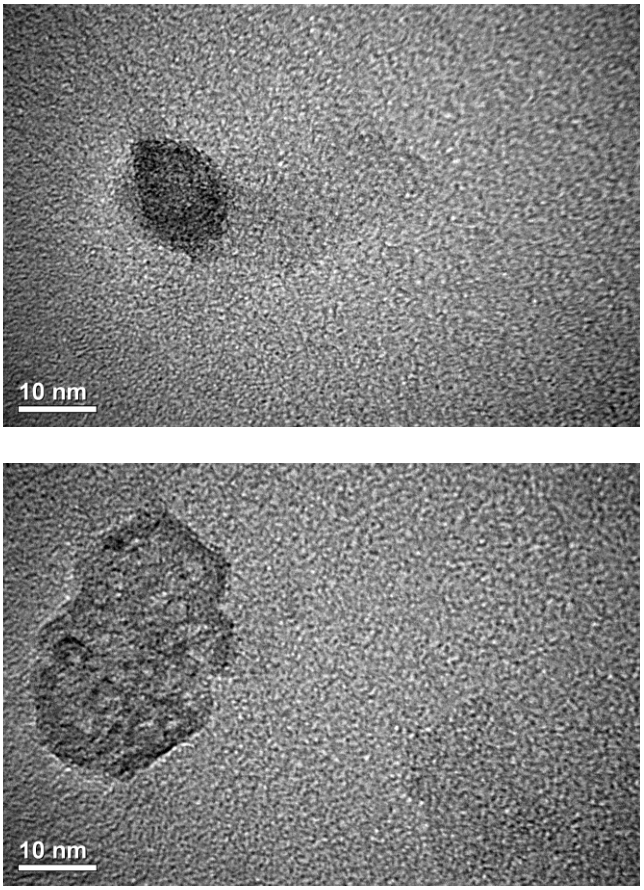

Fig. 58. Transmission Electron Microscopy (TEM) images of Al_2O_3 nanoparticles with a nominal diameter of 10 nm (top) and 50 nm (bottom) [87].*

---

* Adopted from "Experimental Validation of a Simple Analytical Model for Specific Heat Capacity of Aqueous Nanofluids" by Jung, S., Jo, B., Shin, D., and Banerjee, D., 2010, *SAE Power Systems Conference*, Page Number 2010-01-1731, Copyright 2010 by SAE Copyright Administrator.

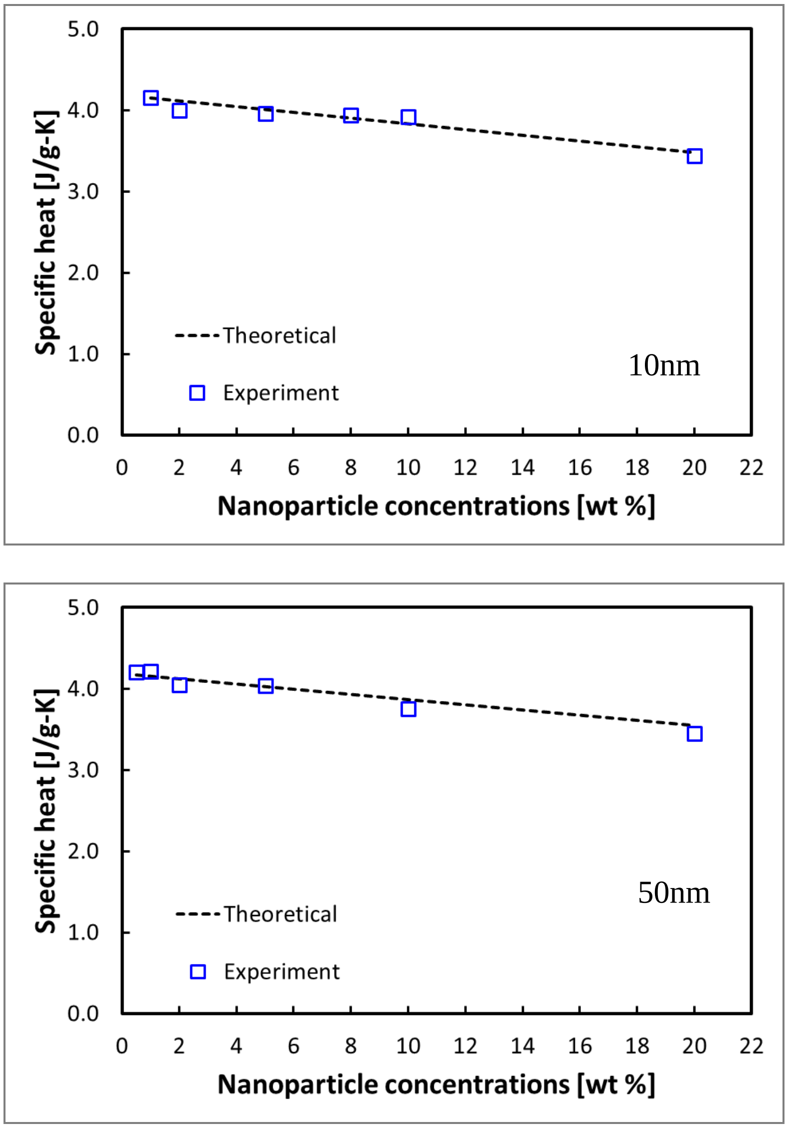

Fig. 59. Comparison of the experimental results with the simple analytical model for Alumina/Water nanofluids [87].*

---

* Adopted from "Experimental Validation of a Simple Analytical Model for Specific Heat Capacity of Aqueous Nanofluids" by Jung, S., Jo, B., Shin, D., and Banerjee, D., 2010, *SAE Power Systems Conference*, Page Number 2010-01-1731, Copyright 2010 by SAE Copyright Administrator.

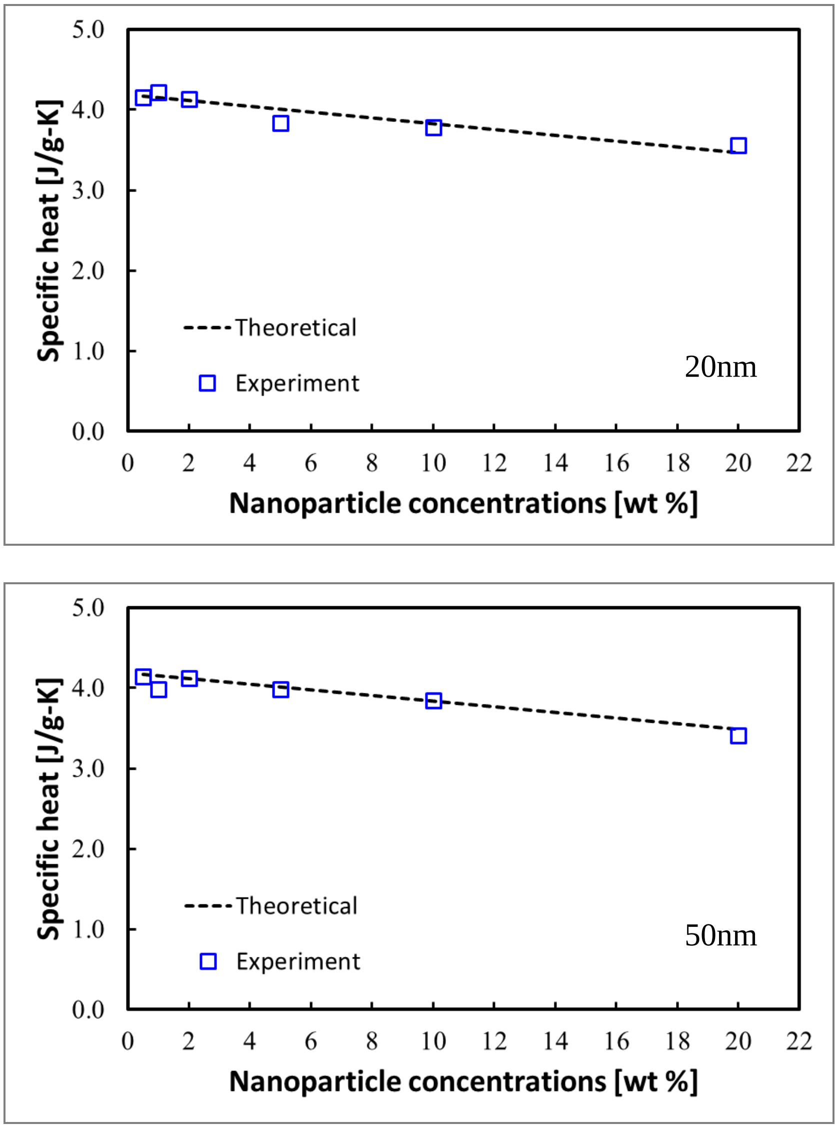

Fig. 60. Comparison of the experimental results with the simple analytical model for Titania/Water nanofluids [87].*

---

* Adopted from "Experimental Validation of a Simple Analytical Model for Specific Heat Capacity of Aqueous Nanofluids" by Jung, S., Jo, B., Shin, D., and Banerjee, D., 2010, *SAE Power Systems Conference*, Page Number 2010-01-1731, Copyright 2010 by SAE Copyright Administrator.

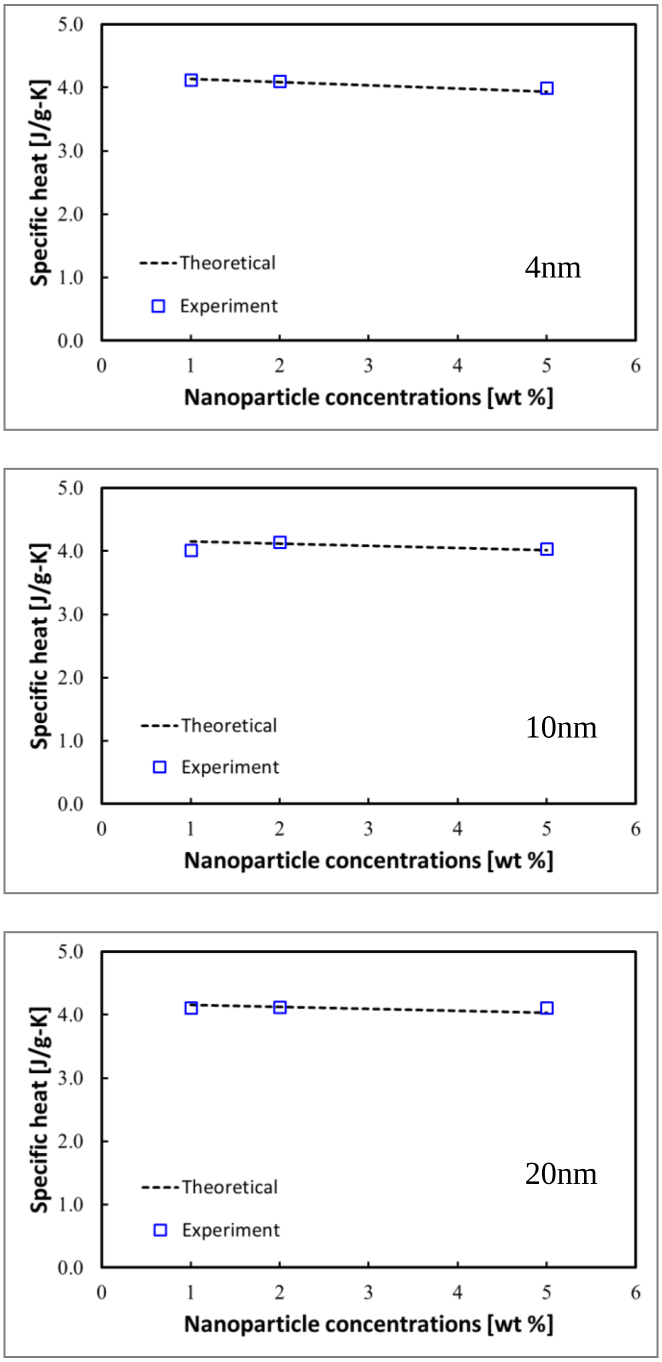

Fig. 61. Comparison of the experimental results with the simple analytical model for Silica/Water nanofluids [87].*

---

* Adopted from "Experimental Validation of a Simple Analytical Model for Specific Heat Capacity of Aqueous Nanofluids" by Jung, S., Jo, B., Shin, D., and Banerjee, D., 2010, *SAE Power Systems Conference*, Page Number 2010-01-1731, Copyright 2010 by SAE Copyright Administrator.

B. A Simple Analytical Model for Specific heat capacity of Nanofluid with Tube Shaped and Disc Shaped Nanoparticles [88]

In this section, a simple analytical model for estimating specific heat capacity of nanofluid containing tube or disc shaped nanoparticles is developed. The total specific heat capacity (C_{total}) of nanofluid is expressed as:

$$C_{total} = \frac{[MxC_{p,n}] + [\frac{Mx}{m_n} m_s C_{p,s}] + [(M - Mx - \frac{Mx}{m_n} m_s) C_{p,l}]}{M} \tag{B-1}$$

Eq. (B-1) is same as eq. (II-1) in Chapter II-A. Considering an individual nanoparticle of diameter (D_{np}) and length (L_{np}), the mass of a nanoparticle and the mass of compressed phase enveloping an individual nanoparticle can be expressed as:

$$m_n = \rho_n V_n = \rho_n \pi \left(\frac{D_{np}}{2} \right)^2 L_{np} \tag{B-2}$$

where ρ_n and V_n are the density and volume of nanoparticle, respectively.

$$m_s = \rho_s V_s = \rho_s \pi \left[\left(\frac{D_{np}}{2} + \delta + d_{sl} \right)^2 \left(L_{np} + \delta + d_{sl} \right) - \left(\frac{D_{np}}{2} + d_{sl} \right)^2 \left(L_{np} + d_{sl} \right) \right] \tag{B-3}$$

where ρ_s and V_s are the density and volume of compressed phase, respectively.

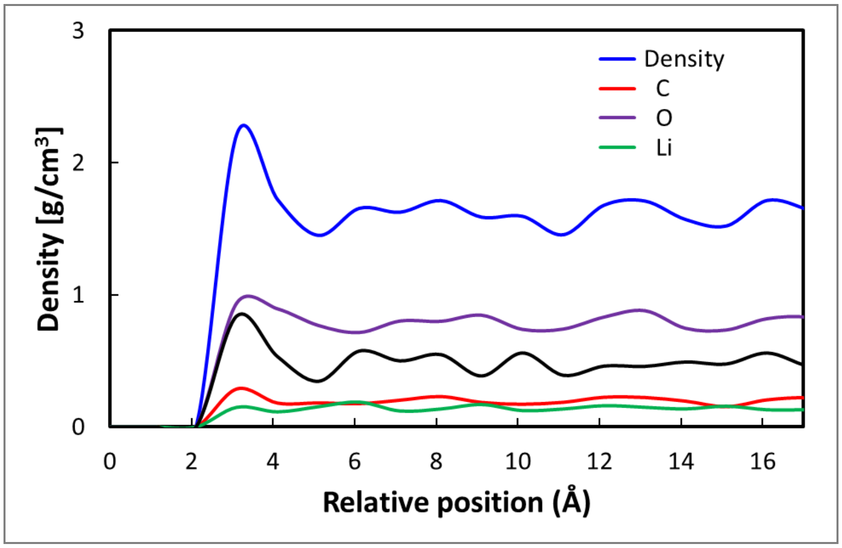

Fig. 62. Spatial density distribution of carbonate salt eutectic phase away from the surface of a carbon nanotube [88].*

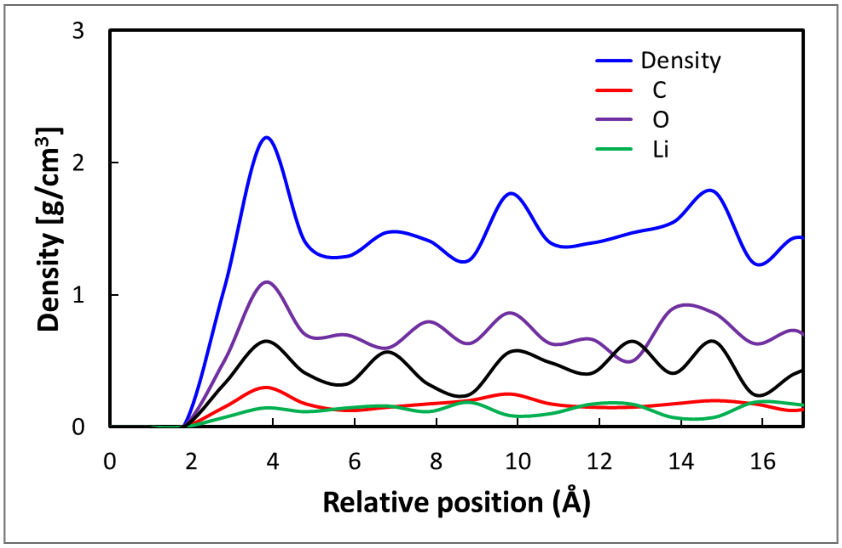

Fig. 63. Spatial density distributions of carbonate salt eutectic phase away from the surface of a graphite nanoparticle [88].*

---

[*] Reprinted with permission from “A Simple Analytical Model for Specific Heat of Nanofluid with Tube Shaped and Disc Shaped Nanoparticles” by Jung, S. and Banerjee, D., 2011, *ASME/JSME 8th Thermal Engineering Joint Conference*, Page Number: AJTEC2011-44372, Copyright 2011 by ASME Publications.

Table 33. The thermo-physical property values (of the solvent phase, the compressed phase, and the nanoparticles. the thickness of compressed phase and the void layer are also listed [88].*

Nanofluid	ρ_n (g/cm^3)	ρ_s (g/cm^3)	C_n (J/g-K)	C_s (J/k-K)	C_l (J/g-K)	d_{sl} (nm)	δ (nm)
CNT/ carbonate salt [a]	0.225 [b]	2.0 [c]	2.15 [d]	16.0 [f]	1.6 [f]	0.2 [c]	1 [c]
Graphite/ carbonate salt [a]	0.225 [b]	2.0 [c]	2.15 [e]	16.0 [f]	1.6 [f]	0.2 [c]	1 [c]

[a] Silica/ Liquid phase of alkaline metal carbonate salt eutectic mixture (Li_2CO_3 : K_2CO_3 in 62:38 molar ratio); [b] Laurent et al. (2010) [89]; [c] MD simulation; [d] Hepplestone et al. (2006) [90]; [e] Hone et al. (2002) [91]; [f] Araki et al. (1988) [47].

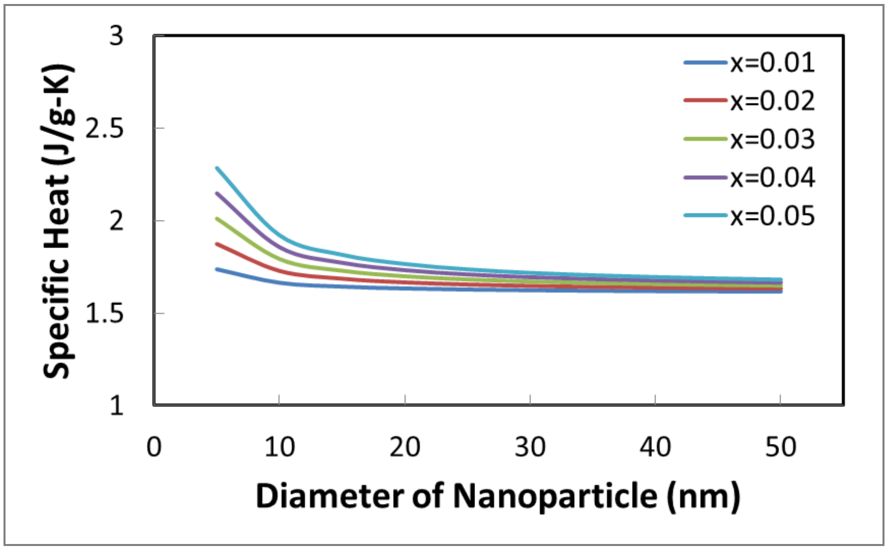

Fig. 64. Variation of the total specific heat capacity of CNT nanofluid with diameter of the nanoparticle and the mass concentration [88].*

---

* Reprinted with permission from “A Simple Analytical Model for Specific Heat of Nanofluid with Tube Shaped and Disc Shaped Nanoparticles” by Jung, S. and Banerjee, D., 2011, *ASME/JSME 8th Thermal Engineering Joint Conference*, Page Number: AJTEC2011-44372, Copyright 2011 by ASME Publications.

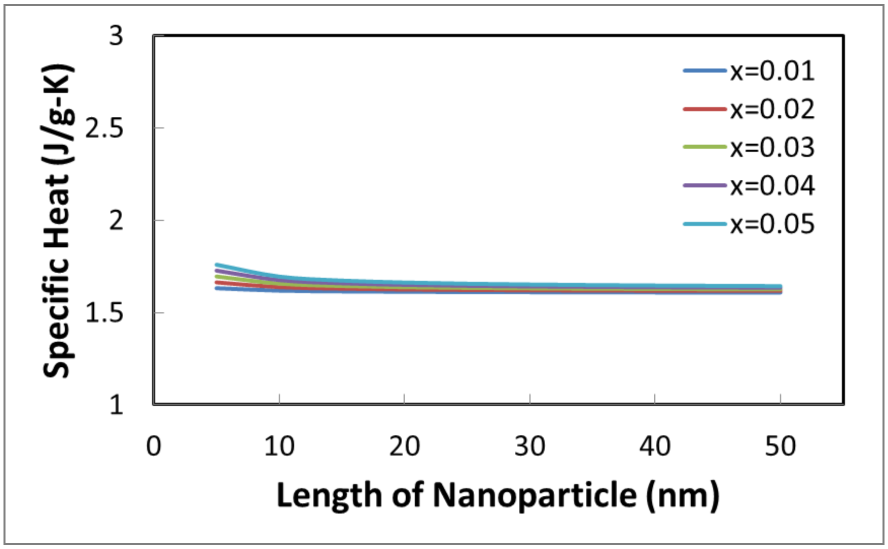

Fig. 65. Variation of the total specific heat capacity of graphite nanofluid with diameter of the nanoparticle and the mass concentration [88].*

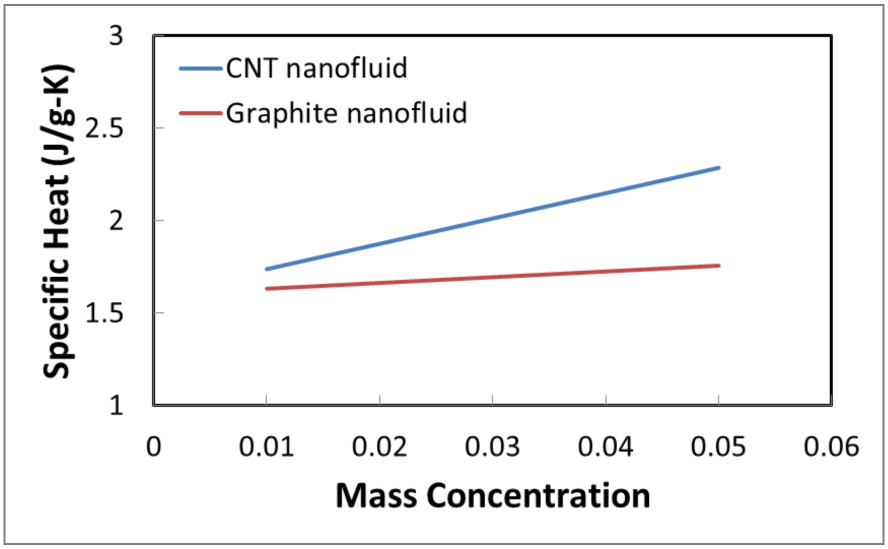

Fig. 66. Comparison of the total specific heat capacity of CNT nanofluid with graphite nanofluid with mass concentration [88].*

---

* Reprinted with permission from "A Simple Analytical Model for Specific Heat of Nanofluid with Tube Shaped and Disc Shaped Nanoparticles" by Jung, S. and Banerjee, D., 2011, *ASME/JSME 8th Thermal Engineering Joint Conference*, Page Number: AJTEC2011-44372, Copyright 2011 by ASME Publications.

After simplification of the various terms, the mass ratio of the compressed phase and the nanoparticle can be expressed as:

$$\frac{m_s}{m_n} = \left(\frac{\rho_s}{\rho_n}\right)\left[\frac{4\delta}{D_{np}}\left(1+\frac{2d_{sl}+\delta}{D_{np}}\right)\right] \tag{B-4}$$

for the nanofluid containing tube shaped nanoparticles. The mass ratio of the compressed phase and the nanoparticle can be also expressed as:

$$\frac{m_s}{m_n} = \left(\frac{\rho_s}{\rho_n}\right)\frac{\delta}{L_{np}} \tag{B-5}$$

for the nanofluid containing disc shaped nanoparticles.

The first terms of Eq. (B4-B5) indicate that the relative density ratio of the nanoparticle and the compressed phase affects the specific heat capacity enhancement of the nanofluid. The second terms of Eq. (B4-B5) indicate that the effect of compressed phase on the specific heat capacity of the nanofluid can be enhanced significantly for nanoparticles smaller than a certain size determined by the compressed phase thickness (δ). Examination of the void layer thickness (d_{sl}) and compressed phase thickness (δ) in Table 33 presents that typically d_{sl} is ~ 0.2nm, whereas typically δ is ~ 1nm. Hence, for the tube shaped nanoparticles that is smaller than ~4nm diameter (for the disc shaped nanoparticles that is smaller than ~1nm length) the contribution from the compressed phase is enhanced dramatically in the increase of specific heat capacity of the nanofluid.

C. Transmission Electron Microscopy (TEM) Image Processing

In this study, example of the modified simple analytical model formulated in Chapter III-B for specific heat capacity is shown using TEM image processing. The alkaline metal carbonate salt eutectic (Li_2CO_3:K_2CO_3=62:38 in molar ratio) was used as the base fluid (neat solvent). This study presents specific heat capacity value of nanofluids containing Al_2O_3 nanoparticles. The nanofluids were characterized using transmission electron microscopy (TEM) image as shown in Fig. 67. Image processing is performed to estimate the mass fraction of the nanoparticle for each size in original TEM image using MATLAB. Fig. 67 (b) shows binary TEM image through image processing. A histogram plot was obtained by calculating the number of pixel for each particle in the binary TEM image as shown in Fig. 68.

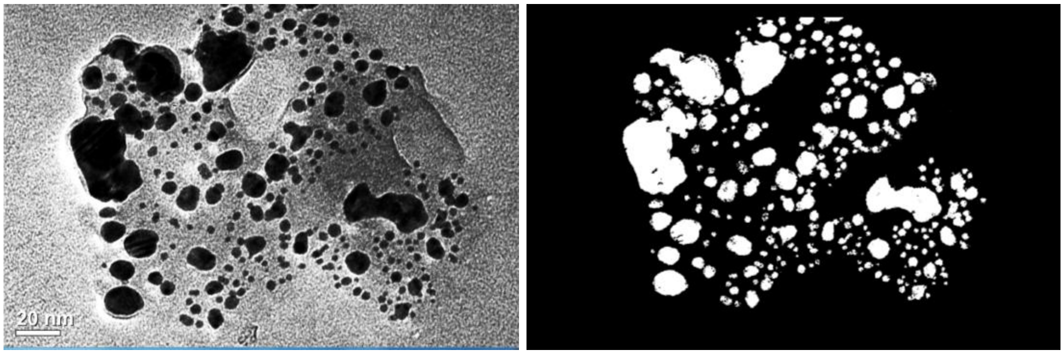

(a) (b)

Fig. 67. TEM image of Al_2O_3 / carbonate salt eutectic nanofluid: (a) original TEM image, (b) binary TEM image.

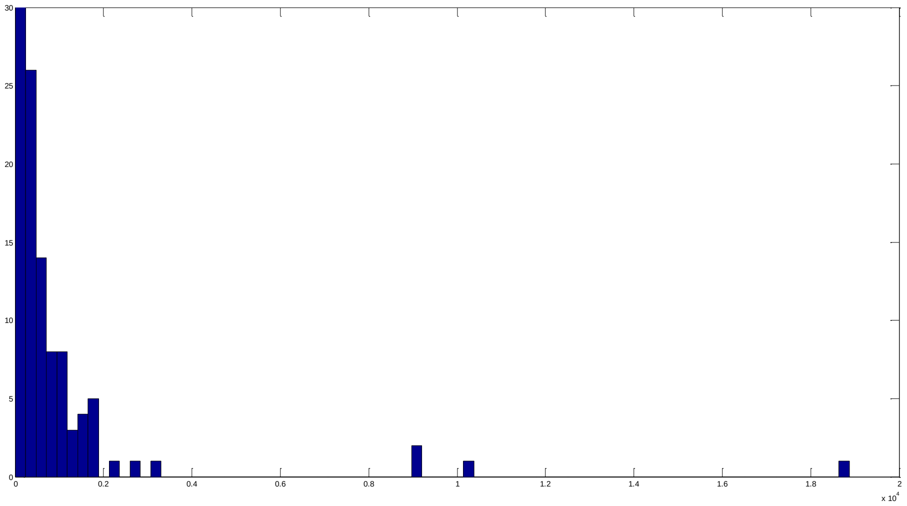

Fig. 68. Histogram: X-axis area (the number of pixels), Y-axis (the number of nanoparticles).

Fig. 69 (a) shows fraction of the number of nanoparticles (A_i) and Fig. 69 (b) presents mass fraction for each nanoparticle (B_i).

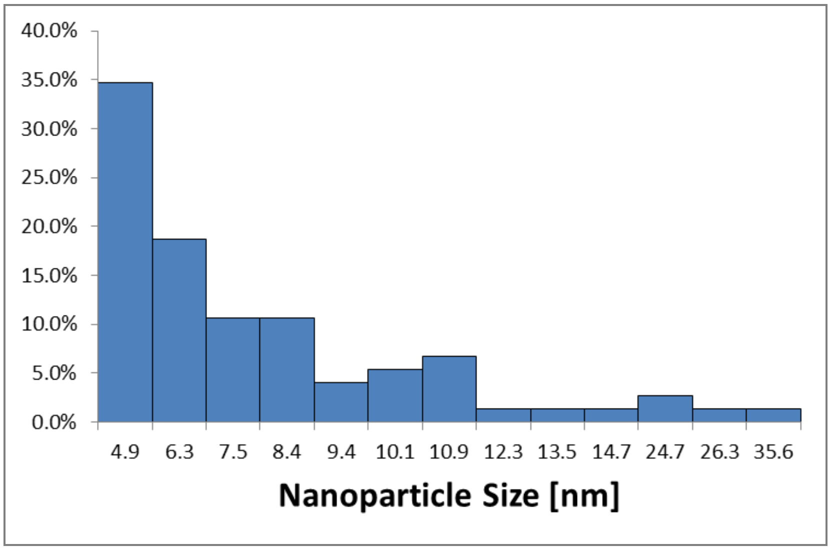

(a)

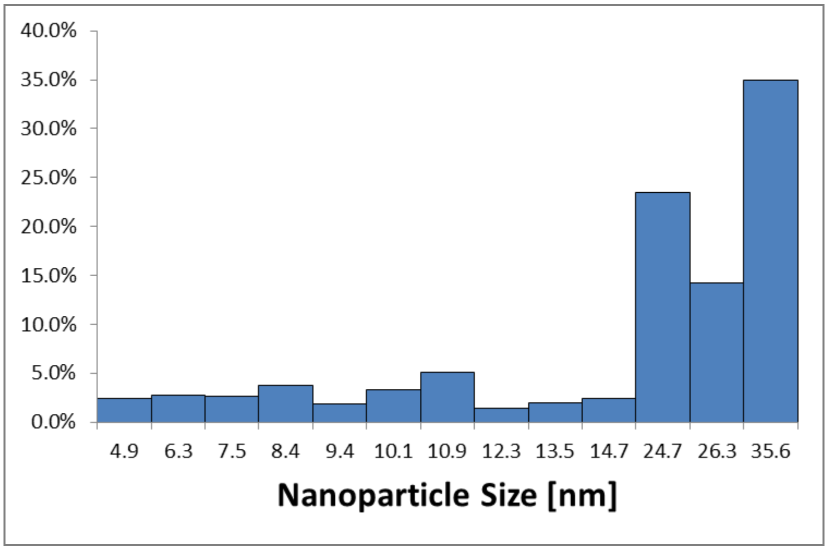

(b)

Fig. 69. (a) fraction of the number of nanoparticle A_i (b) mass fraction for each nanoparticle B_i.

In this study, the specific heat capacity values of alumina (Al_2O_3)/ carbonate salt eutectic nanofluids are calculated using the analytical model. The thermo-physical properties of the pure carbonate salt eutectic, the compressed phase, and alumina (Al_2O_3) nanoparticles are summarized in Table 34 to predict the specific heat capacity value of the nanofluids.

Table 34. The thermo-physical property values of the pure carbonate salt eutectic, the compressed phase, and the Al_2O_3 nanoparticles as well as the thickness of the compressed phase and the void layer.

Nanofluid	ρ_n (g/m^3)	ρ_s (g/m^3)	C_n (J/g-K)	C_s (J/g-K)	C_l (J/g-K)	d_{sl} (nm)	δ (nm)
Al_2O_3/ carbonate salt	4.0	2.57	2.2	250	2.5	0.3	1.2

D. Thermo-cycle data of all samples including pure nitrate salt

1. Pure Nitrate Salt (KNO_3:$NaNO_3$ = 60:40 in molar ratio)

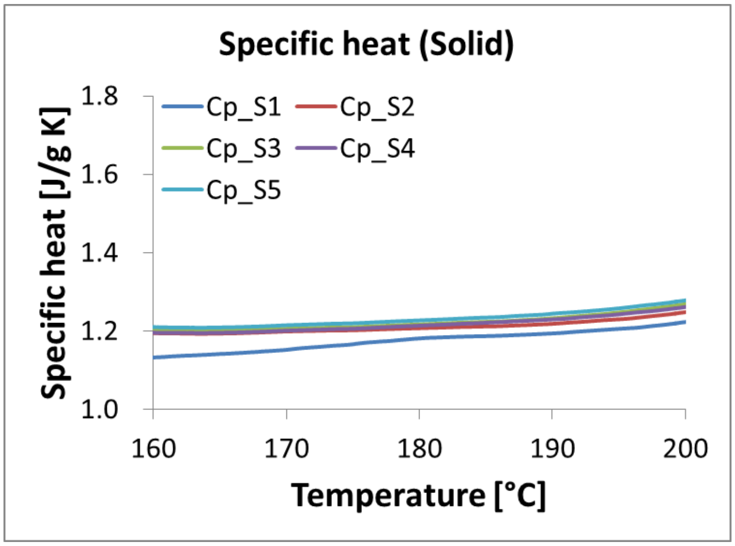

(a)

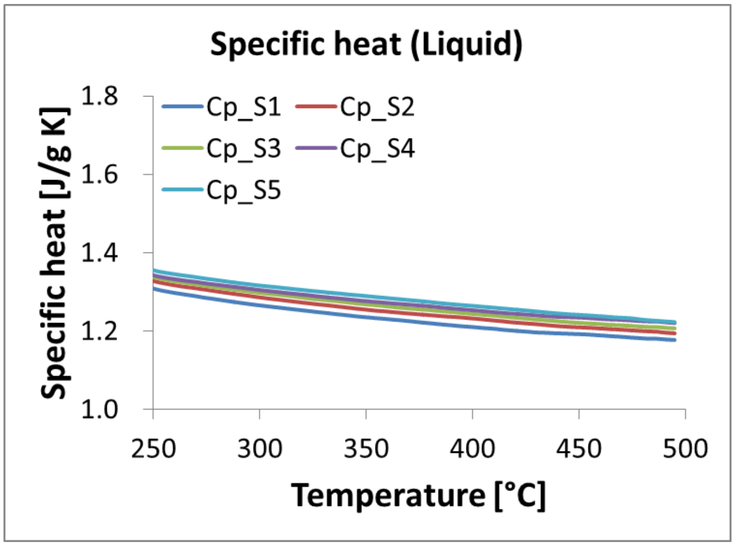

(b)

Fig. 70. Specific heat capacity values plotted as a function of temperature for each thermo-cycle. The samples alkali-nitrate salt mixture (KNO_3:$NaNO_3$ = 60:40 in molar ratio). The measured property data were categorized into (a) solid phase, and (b) liquid phase.

2. Alumina (Al_2O_3)/ Nitrate Salt (KNO_3:$NaNO_3$ = 60:40 in molar ratio)

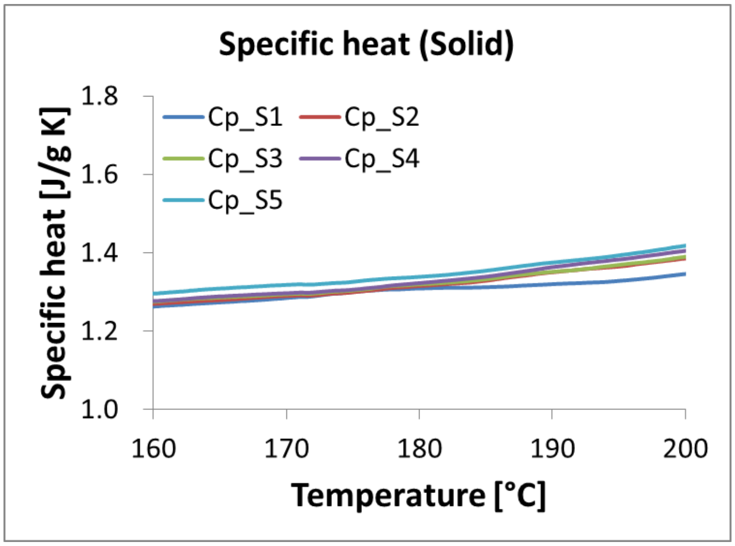

(a)

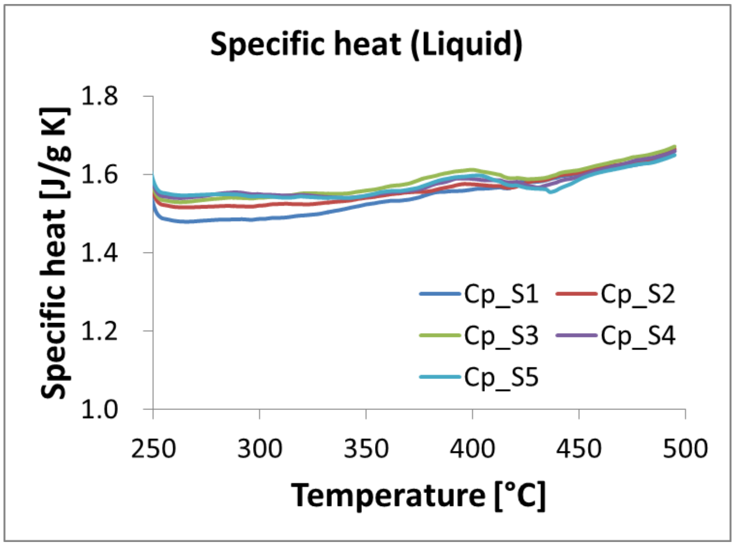

(b)

Fig. 71. Specific heat capacity values plotted as a function of temperature for each thermo-cycle. The samples alkali-nitrate salt (KNO_3:$NaNO_3$ = 60:40 in molar ratio)-based nanomaterials with 1% mass concentration of Alumina (Al_2O_3) nanoparticles for well dispersed nanomaterial. The measured property data were categorized into (a) solid phase, and (b) liquid phase.

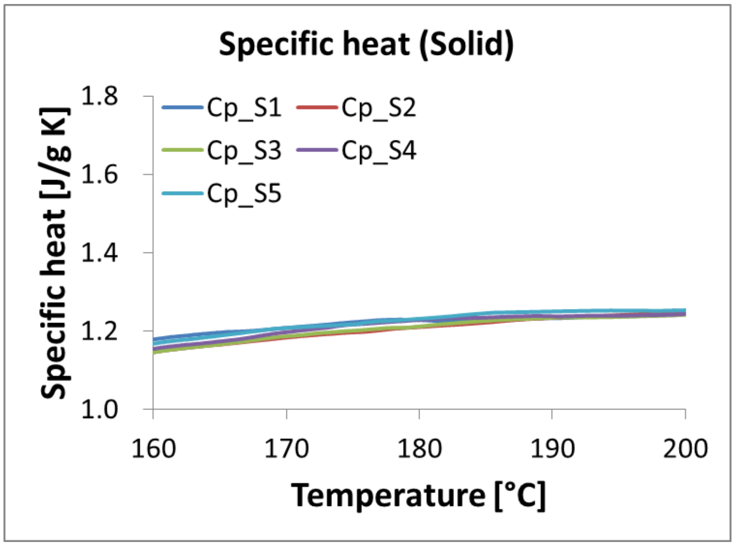

(a)

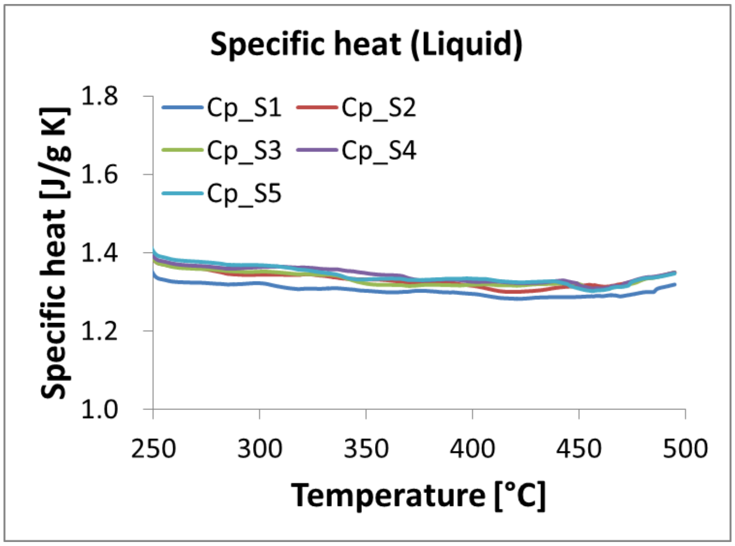

(b)

Fig. 72. Specific heat capacity values plotted as a function of temperature for each thermo-cycle. The samples alkali-nitrate salt (KNO_3:$NaNO_3$ = 60:40 in molar ratio)-based nanomaterials with 1% mass concentration of Alumina (Al_2O_3) nanoparticles for agglomerated nanomaterial. The measured property data were categorized into (a) solid phase, and (b) liquid phase.

3. Silica (SiO_2)/ Nitrate Salt (KNO_3:$NaNO_3$ = 60:40 in molar ratio)

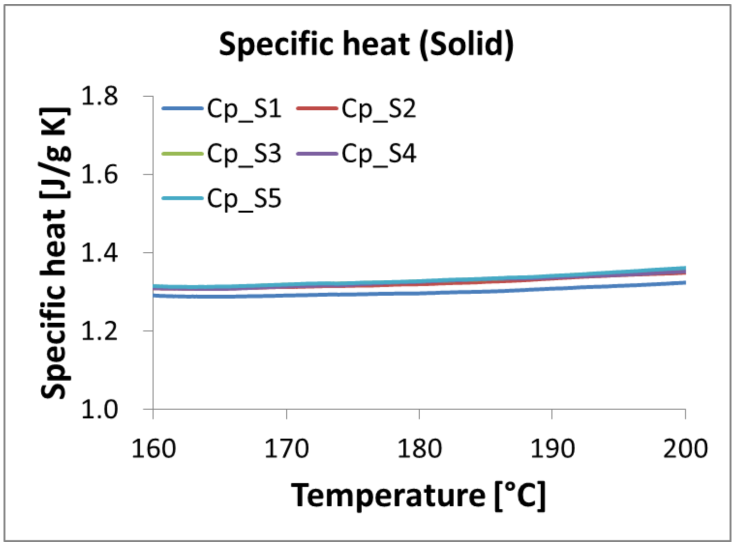

(a)

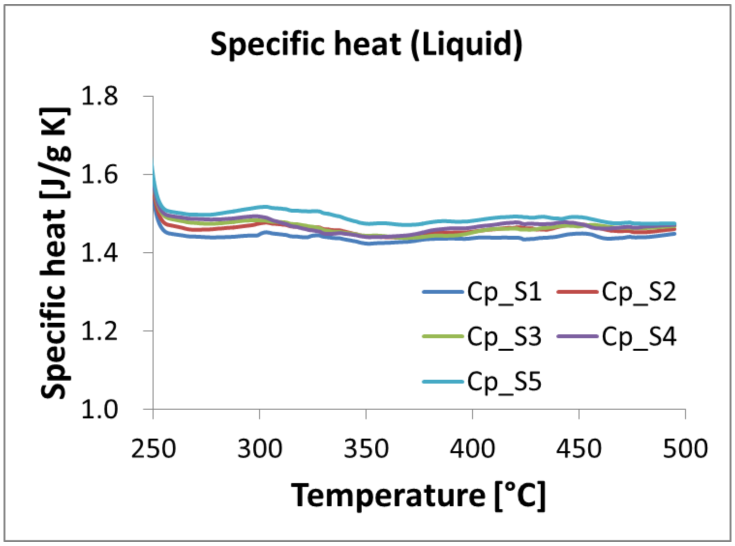

(b)

Fig. 73. Specific heat capacity values plotted as a function of temperature for each thermo-cycle. The samples alkali-nitrate salt (KNO_3:$NaNO_3$ = 60:40 in molar ratio)-based nanomaterials with 1% mass concentration of Silica (SiO_2) nanoparticles. The measured property data were categorized into (a) solid phase, and (b) liquid phase.

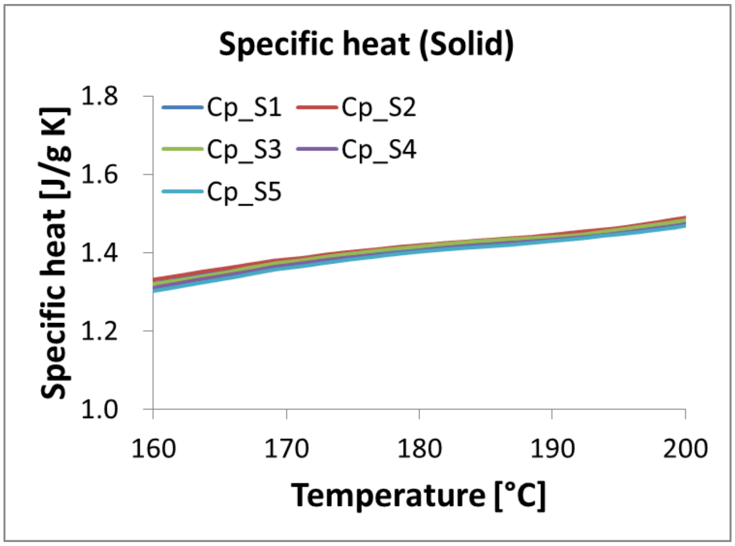

(a)

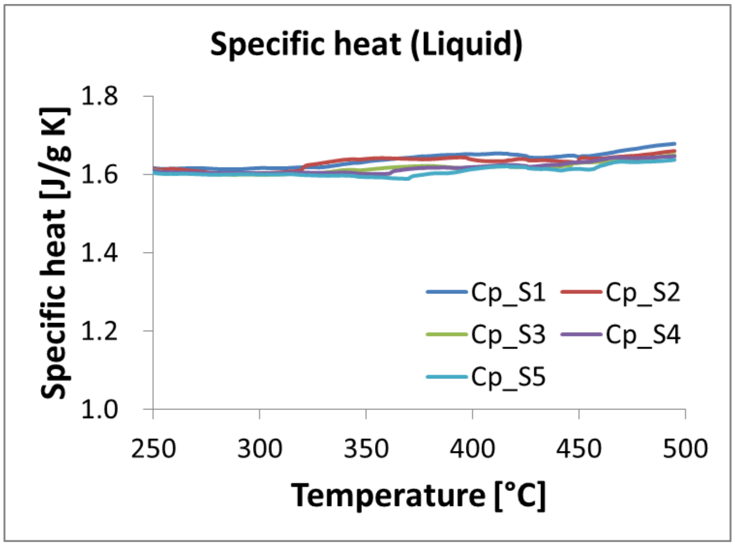

(b)

Fig. 74. Specific heat capacity values plotted as a function of temperature for each thermo-cycle. The samples alkali-nitrate salt (KNO_3:$NaNO_3$ = 60:40 in molar ratio)-based nanomaterials with 2% mass concentration of Silica (SiO_2) nanoparticles. The measured property data were categorized into (a) solid phase, and (b) liquid phase.

4. Titania (TiO_2)/ Nitrate Salt (KNO_3:$NaNO_3$ = 60:40 in molar ratio)

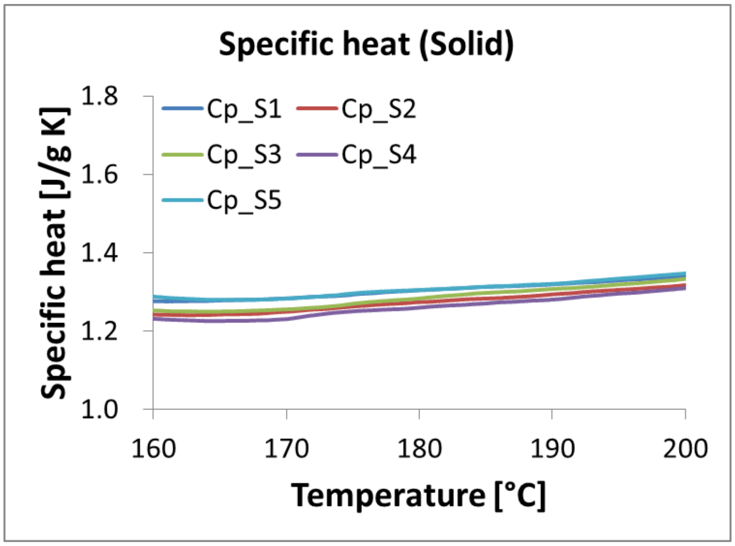

(a)

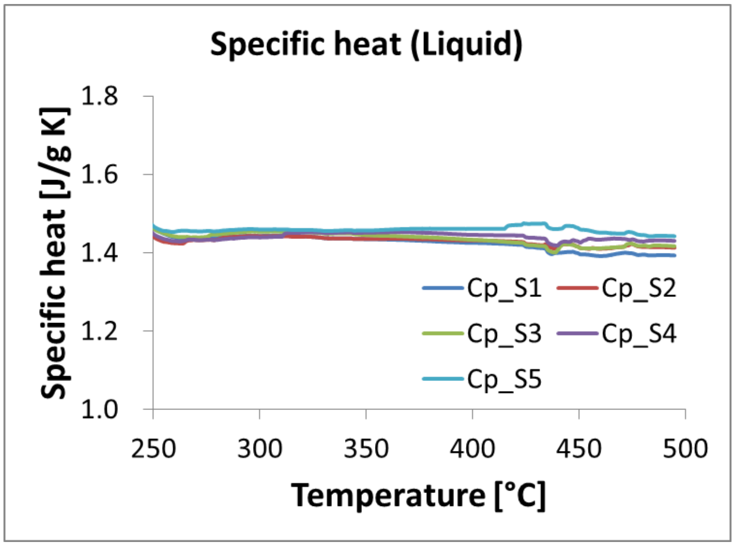

(b)

Fig. 75. Specific heat capacity values plotted as a function of temperature for each thermo-cycle. The samples alkali-nitrate salt (KNO_3:$NaNO_3$ = 60:40 in molar ratio)-based nanomaterials with 1% mass concentration of Titania (TiO_2) nanoparticles. The measured property data were categorized into (a) solid phase, and (b) liquid phase.

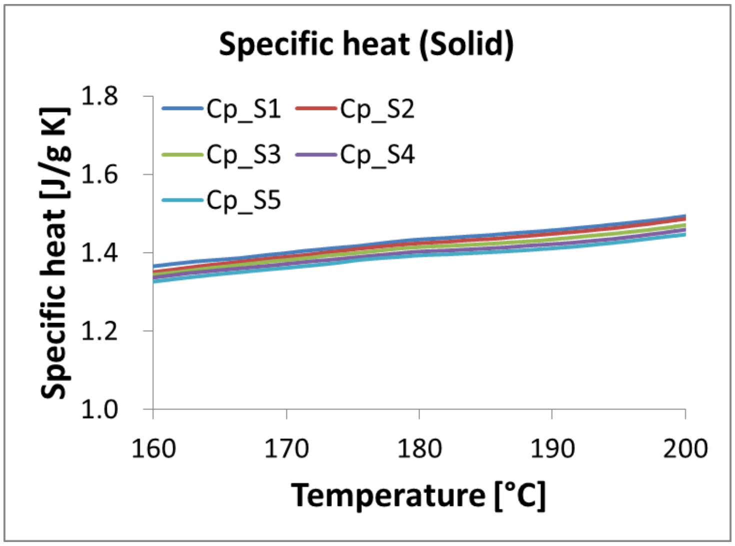

(a)

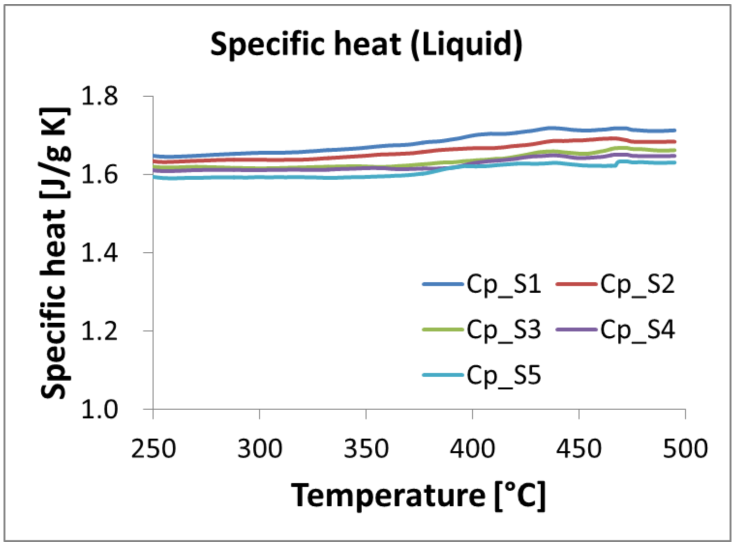

(b)

Fig. 76. Specific heat capacity values plotted as a function of temperature for each thermo-cycle. The samples alkali-nitrate salt (KNO_3:$NaNO_3$ = 60:40 in molar ratio)-based nanomaterials with 2% mass concentration of Titania (TiO_2) nanoparticles. The measured property data were categorized into (a) solid phase, and (b) liquid phase.

5. Silica (SiO_2)/ Nitrate Salt (KNO_3:$LiNO_3$ = 58.8:41.2 in molar ratio)

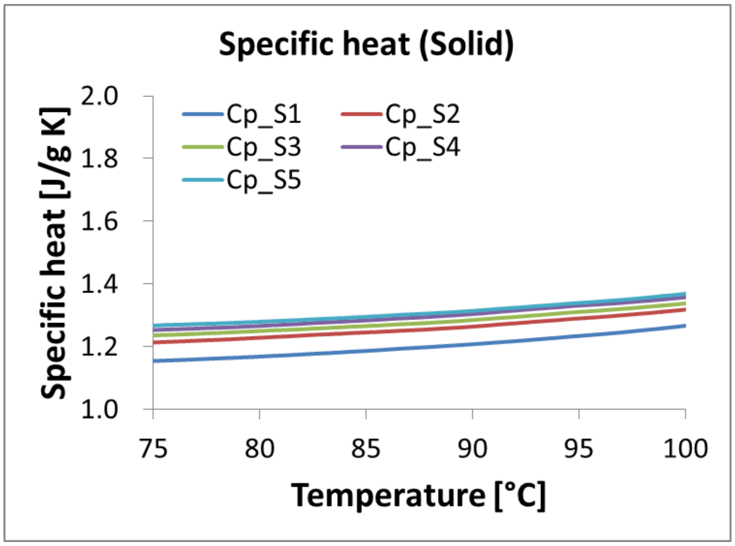

(a)

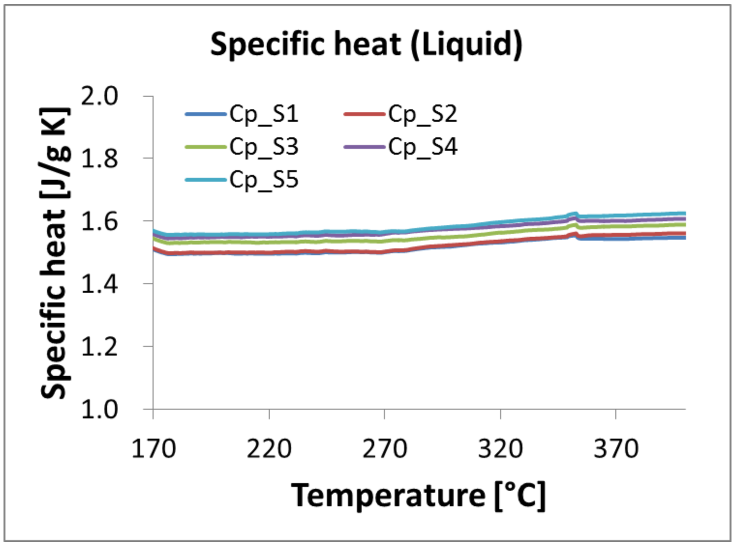

(b)

Fig. 77. Specific heat capacity values plotted as a function of temperature for each thermo-cycle. The samples alkali-nitrate salt mixture (KNO_3:$LiNO_3$ = 58.8:41.2 in molar ratio). The measured property data were categorized into (a) solid phase, and (b) liquid phase.

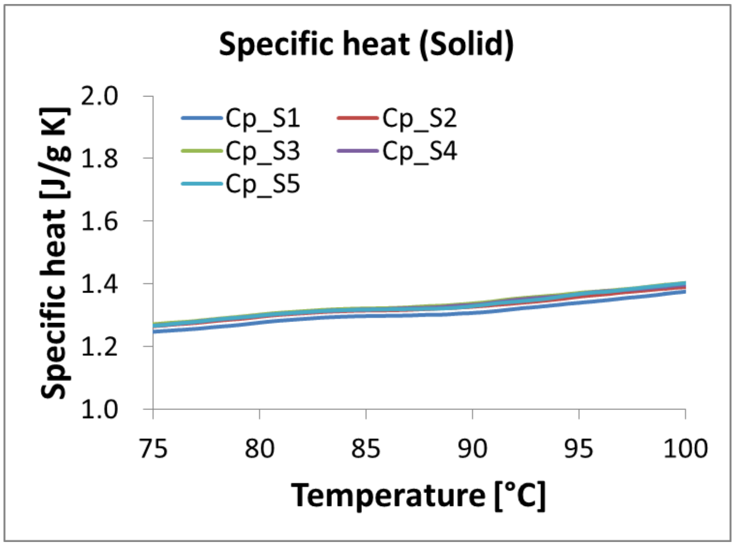

(a)

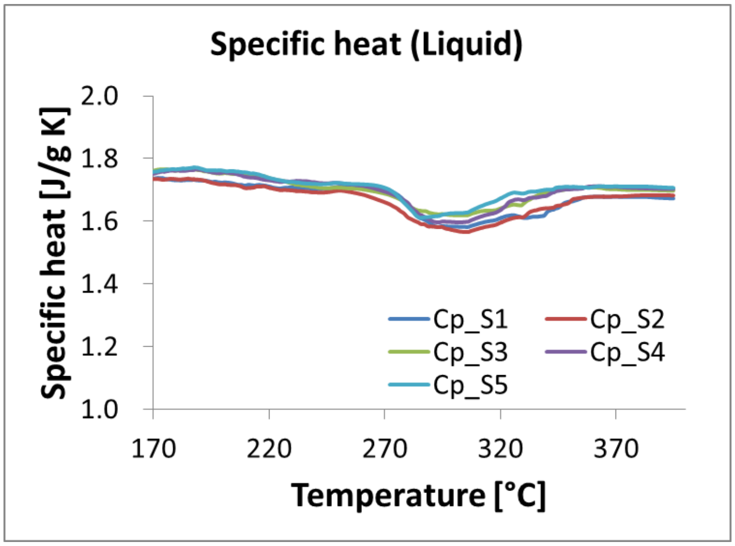

(b)

Fig. 78. Specific heat capacity values plotted as a function of temperature for each thermo-cycle. The samples alkali-nitrate salt (KNO_3:$LiNO_3$ = 58.8:41.2 in molar ratio)-based nanomaterials with 1% mass concentration of Silica (SiO_2) nanoparticles. The measured property data were categorized into (a) solid phase, and (b) liquid phase.

6. Silica (SiO_2)/ Nitrate Salt ($LiNO_3$:$NaNO_3$ = 45:55 in molar ratio)

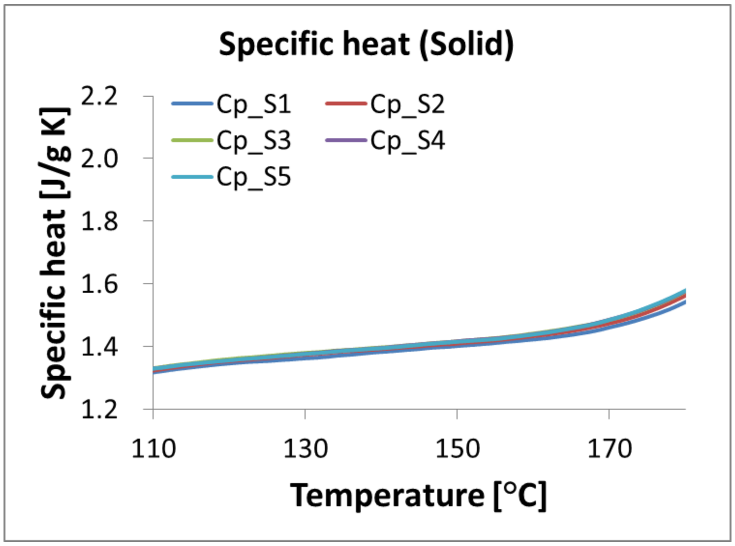

(a)

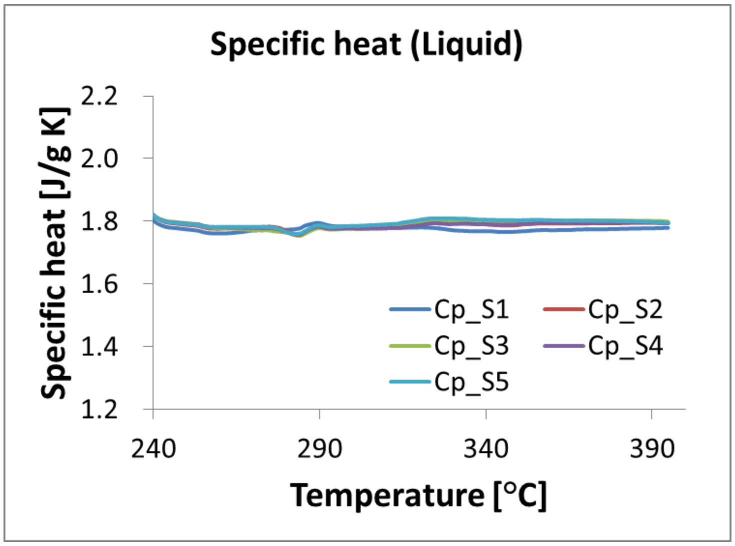

(b)

Fig. 79. Specific heat capacity values plotted as a function of temperature for each thermo-cycle. The samples alkali-nitrate salt mixture ($LiNO_3$:$NaNO_3$ = 45:55 in molar ratio). The measured property data were categorized into (a) solid phase, and (b) liquid phase.

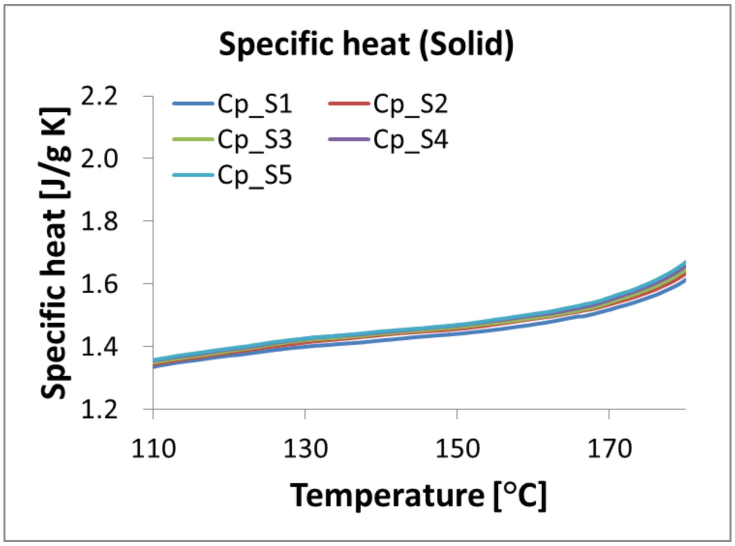

(a)

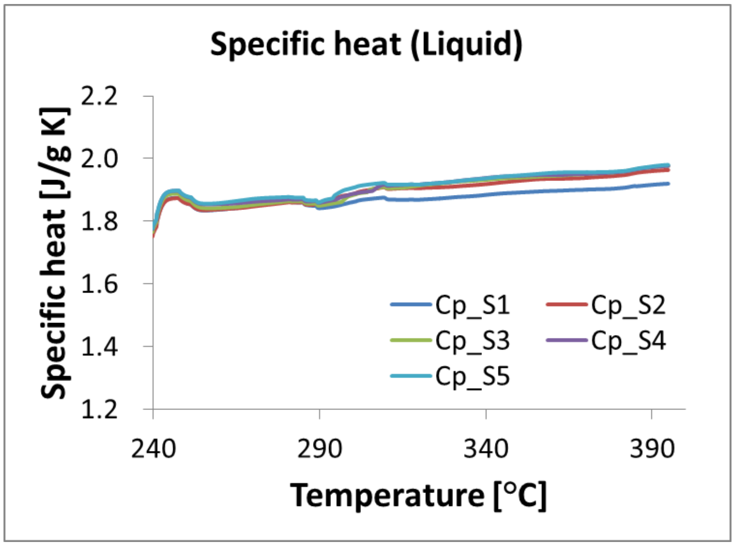

(b)

Fig. 80. Specific heat capacity values plotted as a function of temperature for each thermo-cycle. The samples alkali-nitrate salt ($LiNO_3$:$NaNO_3$ = 45:55 in molar ratio)-based nanomaterials with 1% mass concentration of Silica (SiO_2) nanoparticles. The measured property data were categorized into (a) solid phase, and (b) liquid phase.

7. Silica (SiO_2)/ Lithium-chloride Lithium-nitrate Salt ($LiCl:LiNO_3 = 12.5:87.5$ in molar ratio)

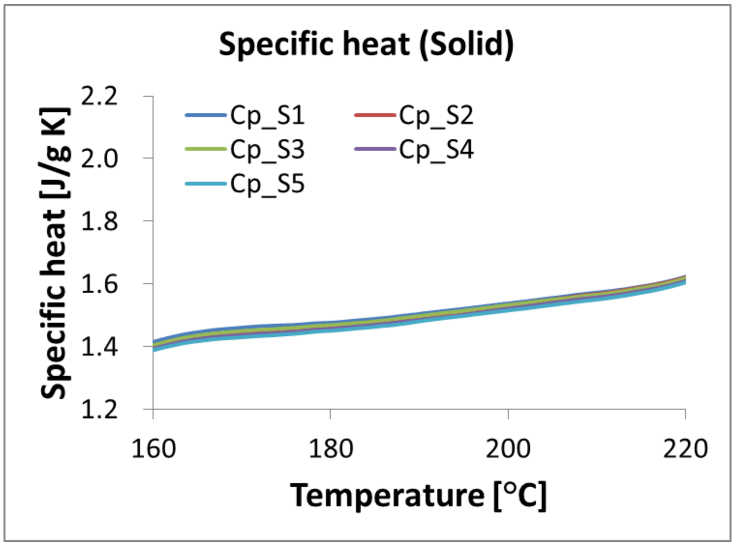

(a)

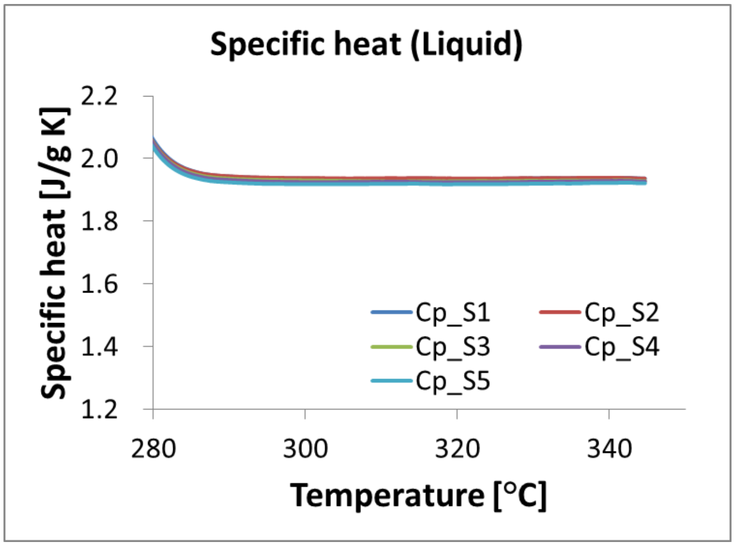

(b)

Fig. 81. Specific heat capacity values plotted as a function of temperature for each thermo-cycle. The samples lithium-chloride lithium-nitrate salt mixture ($LiCl:LiNO_3$ = 12.5:87.5 in molar ratio). The measured property data were categorized into (a) solid phase, and (b) liquid phase.

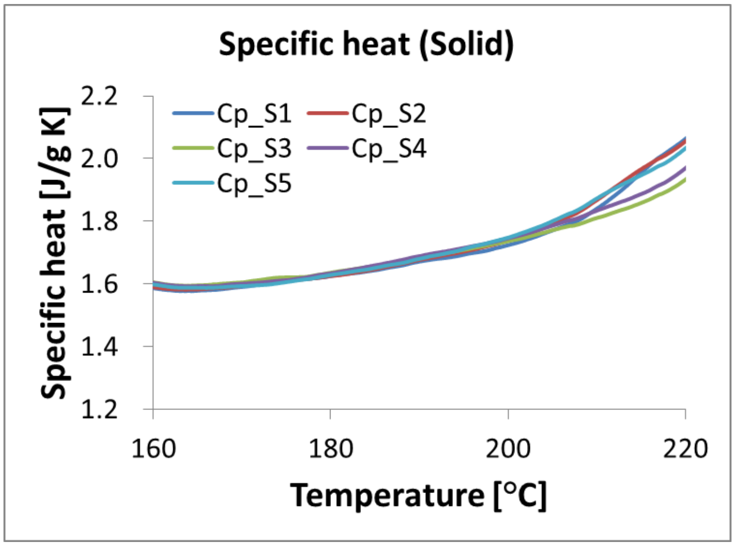

(a)

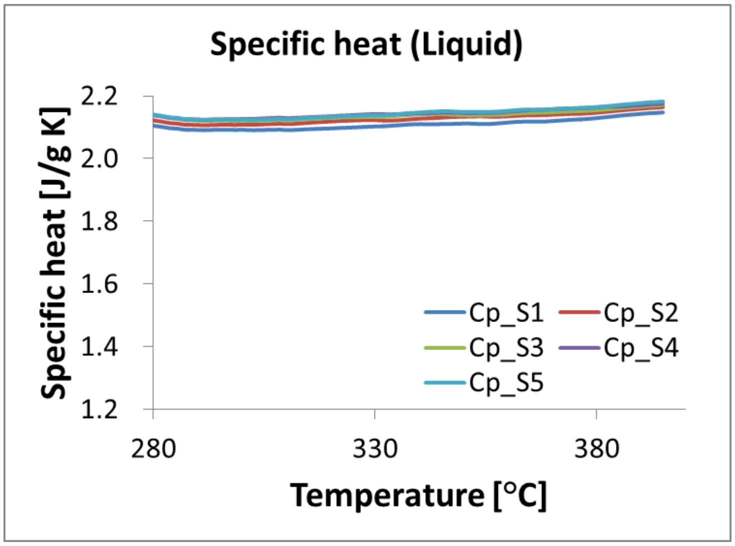

(b)

Fig. 82. Specific heat capacity values plotted as a function of temperature for each thermo-cycle. The samples lithium-chloride lithium-nitrate salt ($LiCl:LiNO_3$ = 12.5:87.5 in molar ratio)-based nanomaterials with 1% mass concentration of Silica (SiO_2) nanoparticles. The measured property data were categorized into (a) solid phase, and (b) liquid phase.

VITA

Name: Seunghwan Jung

Address: Department of Mechanical Engineering
c/o Dr. Debjyoti Banerjee
Texas A&M University
College Station, TX 77843-3123

Email Address: firstday1124@hotmail.com

Education: Ph.D., Mechanical Engineering,
Texas A&M University, College Station, May 2012

M.S., Mechanical Engineering,
University of Southern California, Los Angeles, Dec 2004

B.S., Mechanical Engineering,
Sungkyunkwan University, South Korea, Feb 2002

Publications:

- Byeongnam Jo, **Seunghwan Jung**, Donghyun Shin, and Debjyoti Banerjee, "Anomalous Rheological Behavior of Complex Fluids (Nanofluids)", *Proceedings of The ASME 2011 International Mechanical Engineering Congress & Exposition*, November 11-17, 2011, Denver, Colorado, USA.
- **Seunghwan Jung** and Debjyoti Banerjee, "A simple analytical model for specific heat of nanofluid with tube shaped and disc shaped nanoparticles", *Proceedings of The ASME/JSME 2011 8th Thermal Engineering Joint Conference*, March 13-17, 2011, Honolulu, Hawaii, USA.
- **Seunghwan Jung** and Debjyoti Banerjee, "Enhancement of heat capacity of nitrate salt using mica nanoparticles", *The ICACC'11 35th International Conference and Exposition on Advanced Ceramics and Composites*, January 23-48, 2011, Daytona, Florida, USA.
- **Seunghwan Jung**, Byeongnam Jo, Donghyun Shin, and Debjyoti Banerjee, "Experimental validation of a simple analytical model for specific heat capacity of aqueous nanofluids", *Proceedings of 2010 SAE Power Systems Conference*, November 2-4, 2010, Ft. Worth, TX, USA.